Properties of the Acoustic Vector Field in Underwater Waveguides

David R. Dall'Osto

A dissertation
submitted in partial fulfillment of the
requirements for the degree of

Doctor of Philosophy

University of Washington

2013

Reading Committee:

Peter H. Dahl, Chair

Brian L. Polagye

Robert C. Spindel

Program Authorized to Offer Degree:
Mechanical Engineering

University of Washington

Abstract

Properties of the Acoustic Vector Field in Underwater Waveguides

David R. Dall'Osto

Chair of the Supervisory Committee:
Professor Peter H. Dahl
Department of Mechanical Engineering

This thesis focuses on the description and measurement of the underwater acoustic field, based on vector properties of acoustic particle velocity. The specific goal is to interpret vector sensor measurements in underwater waveguides, in particular those measurements made in littoral (shallow) waters. To that end, theoretical models, which include the effects of reflections from the waveguide boundaries, are developed for the acoustic intensity, i.e. the product of acoustic pressure and acoustic particle velocity. Vector properties of acoustic intensity are shown to correspond to a non-dimensional vector property of acoustic particle velocity, its degree of circularity, which describes the trajectory of particle motion. Both experimental measurements and simulations of this non-dimensional vector property are used to analyze characteristics of sound propagation in underwater waveguides.

Two measurement techniques are utilized in the experiments described in this thesis. In the first, particle velocity is obtained indirectly by time integration of the measured pressure gradient between two closely spaced (with respect to an acoustic wavelength) conventional pressure sensitive hydrophones. This method was used in ocean experiments conducted with vertical line arrays of hydrophones. In the second technique, particle velocity is measured directly by time integration of the signal generated by an accelerometer. An additional pressure measurement from a co-located hydrophone forms what is known as a "combined sensor" in the Russian literature, which allows for estimation of the vector acoustic intensity. This method was utilized mainly in laboratory experiments.

TABLE OF CONTENTS

LIST OF FIGURES

ACKNOWLEDGMENTS

I would like to acknowledge and thank a number of people who have been supportive in my completion of my thesis and this degree. First, and most importantly, I thank my advisor, Peter Dahl, who brought me into the world of underwater acoustics. He has helped guide my research, encouraged me to focus on vector acoustics, and gave me the freedom to do independent research in this field. We have worked together for seven years now, culminating in a successful experimental deployment of our vector sensor in April 2013. I am not only grateful for the funding he has provided to support my Ph.D., but for his genuine interest in seeing me excel in this field.

I also would like to thank Bob Spindel, not only for his help in reading an early draft of this dissertation, but for his encouragement to follow the footsteps of Russian pioneers in vector acoustics. Bob has been kind enough to share his experiences in underwater acoustics, and I hope that one day, my career in underwater acoustics will reflect well on his. We build upon those who have come before us.

I would also like to thank my committee members in mechanical engineering, Brian Polagye and Per Reinhall, and John Horne for joining my committee. Additionally, I would like to thank my other colleagues at the APL, who have helped make this research a reality.

Finally, I would like to give thanks for the support my family and friends have given me over the years. Especially to my father, Raymond, for his continual help, and for inspiring within me an enduring love for science and progress.

Chapter 1

INTRODUCTION

A description of the acoustic field, developed by the late Richard Heyser, is used in this thesis for analysis of the acoustic vector field in the ocean. Heyser's notation efficiently describes vector properties of the acoustic field and is applied to field measurements. This research has direct application for seabed exploration and for determining the location of acoustic sources.

Heyser's notation can be applied to a conservation of energy description of the acoustic field, which includes a vector term called the instantaneous intensity, $\vec{S}$. This energy-flux vector was first described in 1873 by Nikolay Umov, in his paper "The Equation of Energy Motion in Bodies," and is commonly referred to in Russian texts as the Umov vector [1]. Electrical engineers may be more familiar with its appearance as the Poynting vector, which describes electromagnetic waves [2]. Shortly before his death in 1987, Heyser presented a complex representation of $\vec{S}$ based on the Hilbert transform [3]. Heyser's complex intensity was embraced by the acousticians Frank Fahy [4] and Finn Jacobsen [5], who have since further developed these concepts in the field of aeroacoustics. In this thesis, Heyser's notation is applied to the analysis of sound underwater.

Underwater sound propagation is affected by the sea surface and seabed, which trap and guide sound energy, creating an acoustic waveguide. The interaction between multiple reflections from the waveguide boundaries result in regions of constructive or destructive interference. The study of properties of the vector field relating to this interference is a significant part of the work making up this thesis. Field measurements of these properties are shown to relate to the source frequency, acquisition geometry and the environmental characteristics of the waveguide, e.g., the composition of the seabed.

As early as 1979, Heyser applied his theory to detect sediment layering in the ocean seabed [6]. A similar result is presented in this thesis using a non-dimensional parameter, the degree of circularity, $\vec{\Theta}$. This parameter describes the trajectory of fluid particle motion induced by an acoustic field, which can follow a straight line, an ellipse or a circle. The degree of circularity, $\vec{\Theta}$, can be directly measured by a three-dimensional particle motion sensor. An identical formulation of $\vec{\Theta}$, derived from the linear acoustic equations and which is based on complex intensity, allows for an approximate measure of $\vec{\Theta}$ from a single component of intensity. Controlled laboratory experiments are used to validate these formulations of $\vec{\Theta}$. The approximate measure of $\vec{\Theta}$ is then applied to experimental measurements in three littoral (shallow) seas to analyze sound propagation in ocean waveguides, in particular how $\vec{\Theta}$ is affected by sediment layering and source depth and frequency. To the best of my knowledge, this thesis presents the first application of Heyser's notation to examine properties of the acoustic vector field in underwater (ocean) waveguides.

The chapters of this thesis are organized as follows. The next four chapters present a tutorial of vector acoustics. Chapter 2 reviews the basic vector properties of the acoustic field, namely how the pressure, p, and particle velocity, $\vec{v}$, form the instantaneous intensity vector, $\vec{S}$, and its complex counterpart, $\vec{I_c}$. Chapter 3 presents formulations for vector properties of curl and divergence to complex acoustic intensity, $\vec{I_c}$. Chapter 4 relates the vector properties of $\vec{I_c}$ to a more subtle property of the vector field, the degree of circularity $\vec{\Theta}$, which describes the trajectory of particle motion. Chapter 5 describes the operating principles and construction of accelerometer-based vector sensors, and presents controlled laboratory measurements as an experimental validation of the formulations of $\vec{\Theta}$ discussed in Chapter 4; vector measurements from an ocean experiment (April 2013) are also discussed.

The next two chapters (6 and 7) present ocean measurements of vector properties and an interpretation using acoustic models. These results appear in two papers [7, 8] published in the Journal of the Acoustical Society of America. Chapter 6 presents an application of vector properties to determine the layering structure of the seabed from the vertical component of complex, measured by a vertical line array of hydrophones. Chapter 7 presents a similar application relating models of the vector properties of complex intensity to experimental measurements of the complex vertical intensity in an ocean waveguide.

Chapter 8 concludes this thesis, providing a brief summary of the results and the prospects for future research.

Chapter 2

FORMULATION OF THE ACOUSTIC INTENSITY VECTOR

2.1 Acoustic Pressure and Particle Velocity

The sound waves discussed here are compressional waves in a fluid. These compressional waves cause a momentary increase in pressure, and a pressure gradient that induces fluid motion, disturbing the fluid from its equilibrium state. To quote Fahy [4], "Once the disturbance [sound] has passed, everything is just as it was before - the fluid particles are once more at rest and do not continue to oscillate." The linear acoustic equations, which are derived from a linearization of Navier-Stokes equations, describe the relationship between the fluid particle motion (velocity) and the pressure fluctuations caused by an acoustic field.

A particle is defined herein as a small volume of fluid that contains a large collection of molecules. Although individual molecules are in constant motion (Brownian motion), in an average sense the fluid volume has uniform properties of density, pressure and velocity. To paraphrase David Blackstock [9], the smallest possible volume that defines a fluid particle is one that upon further reduction of its size, may no longer have the same density. The average movement of the particle in the absence of sound, in this linearized framework (or viewpoint), is zero.

When the fluid is subjected to a sound field, the particles exhibit a uniform motion, described by their acoustic particle velocity, $\vec{v}$. In this thesis, we directly measure $\vec{v}$ with a vector sensor, and to do so must also be concerned about the maximum size of a fluid volume that still behaves like a particle. A neutrally buoyant vector sensor operates on the principle that it moves like the fluid itself. This interpretation requires the physical size of the sensor to be much less than the characteristic length scales of the acoustic field [10]. Specifically, a characteristic scale of the field of frequency, f, is the acoustic wavelength, $\lambda = c/f$, where c is the speed of sound. We adapt the maximum to be $\lambda/4$, although note that further limitations of these sensors are discussed in Chapter 5.

We can describe the acoustic field by the particles' fluid properties of pressure, p, density, ρ, and particle velocity, $\vec{v}$. When subjected to an acoustic field, perturbations arise in the pressure, $p = p_0 + p_1$, and density, $\rho = \rho_0 + \rho_1$, where $\rho_1 \ll \rho_0$ and $p_1 \ll p_0$. Similarly, the acoustic field induces a momentary displacement, $\vec{\xi}$, of the fluid particles from their equilibrium position, which results in a non-zero particle velocity $\vec{v} = d\vec{\xi}/dt$. The linear acoustic equations, which describe the relationship between these fluid properties, assume that at equilibrium, i.e., no sound, the fluid has pressure $p = p_0$ and density $\rho = \rho_0$, and is also at rest, $\vec{v} = 0$. To simplify our notation, from now on the perturbations ρ_1 and p_1, i.e., the acoustic field variables, will be defined without their subscript, and the ambient fluid properties will be defined as p_0 and ρ_0.

2.1.1 Conservation of mass

The linearized conservation of mass is,

$$\nabla \cdot \vec{\xi}(t) + \frac{\rho(t)}{\rho_0} = 0, \tag{2.1}$$

which states that dilation of a particle's boundaries, $\nabla \cdot \vec{\xi}$, corresponds to the density of the particle. A particle contains a fixed number of molecules, thus a positive dilation (outward strain) of the particles' boundaries increases its volume, reducing its density. A negative dilation corresponds to a compression of the particle volume, and an increase in density. The pressure and density are related through the equation of state which, assuming no heat transfer between particles, is $\frac{dp}{d\rho}|_{\rho_0} = c^2$.

An alternate form of the conservation of mass, expressed in terms of p and $\vec{v}$, is formulated from the time derivative of Eq. 2.1, and is,

$$\nabla \cdot \vec{v}(t) = -\frac{1}{\rho_0 c^2}\frac{\partial p}{\partial t}. \tag{2.2}$$

This form will be useful in the derivation of the conservation of energy equation, presented in the next section.

2.1.2 Conservation of momentum

The linearized conservation of momentum, known as Euler's equation, is

$$\frac{\partial \vec{v}(t)}{\partial t} = -\frac{1}{\rho_0}\nabla p \tag{2.3}$$

which states that the change in momentum of a particle (given by the time derivative of $\rho_0\vec{v}$ times the volume of the particle) is the result of forces on the surface of the particle (the pressure gradient, ∇p). Note that the speed of a fluid particle is proportional to the perturbative pressure, and is much less than the speed of sound. It is the compressional wave, described by the pressure gradient in Euler's equation, that propagates energy through the fluid medium at the speed of sound.

2.2 Acoustic Energy Conservation

Acoustic energy propagation is described by the conservation of acoustic energy equation. Its derivation can start with either linearized conservation of mass or momentum, which is an important consideration if p and $\vec{v}$ have a complex representation (discussed in Chapter 3). For now, let us only consider real valued $p(t)$ and $\vec{v}(t)$. Following Allan Pierce [2], who starts with Euler's equation, the dot product of Eq. 2.3 with $\vec{v}(t)$ is taken,

$$\vec{v}(t) \cdot \frac{\partial}{\partial t}\rho_0\vec{v}(t) = -\vec{v}(t) \cdot \nabla p(t), \tag{2.4}$$

which upon re-arrangement is,

$$\frac{\partial}{\partial t}\frac{\rho_0|\vec{v}(t)|^2}{2} = -\vec{v}(t) \cdot \nabla p(t). \tag{2.5}$$

Note that the term on the left hand side corresponds to the kinetic energy density,

$$w_{kin}(t) = \frac{1}{2}\rho_0|\vec{v}(t)|^2. \tag{2.6}$$

which upon integration over some control volume yields the kinetic energy ($\frac{1}{2}m|\vec{v}|^2$) of that volume due to sound.

Continuing with the derivation, the right hand side of Eq. 2.4 can be expanded as,

$$-\vec{v}(t) \cdot \nabla p(t) = p(t)\nabla \cdot \vec{v}(t) - \nabla \cdot (p(t)\vec{v}(t)). \tag{2.7}$$

The first term, containing $\nabla \cdot \vec{v}$, can be written as a function of pressure through the conservation of mass (Eq. 2.2), and is,

$$p(t)\nabla \cdot \vec{v}(t) = -\frac{p(t)}{\rho_0 c^2}\frac{\partial p(t)}{\partial t}. \tag{2.8}$$

Note that the term on the right hand side corresponds to the potential energy density,

$$w_{pot}(t) = \frac{1}{2}\frac{p(t)^2}{\rho_0 c^2}. \tag{2.9}$$

which upon integration over some control volume yields the total potential energy of that volume due to sound. (The dimension of both potential and kinetic energy density are the same as pressure.)

The final term of Eq. 2.7, $\nabla \cdot \; (p(t)\vec{v}(t))$, is the divergence of the Umov vector, which we will call the instantaneous intensity, $\vec{S}(t)$. Rewriting Eq. 2.4 once again in terms of $\vec{S}(t)$ and the potential and kinetic energy densities, the conservation of energy equation is,

$$\frac{\partial}{\partial t}w_{kin}(t) + \frac{\partial}{\partial t}w_{pot}(t) + \nabla \cdot \; \vec{S}(t) = 0. \tag{2.10}$$

where, $\nabla \cdot \; \vec{S}(t)$, describes the energy flux into (or out of) a volume that balances the time-rate of change of total energy within the volume.

2.3 Instantaneous Intensity Vector

The instantaneous intensity, or Umov vector, is,

$$\vec{S}(t) = Re\{p(t)\}Re\{\vec{v}(t)\}. \tag{2.11}$$

Note that $\vec{S}(t)$ is identified explicitly by the real part of the pressure and particle velocity, which, in general, can have a complex representation. A complex representation of a real-valued measurement incorporates both its magnitude and phase. The formulation of complex representations of real-valued measurements are discussed in the next section.

The time-averaged behavior of $\vec{S}(t)$ undergoes an interesting transition with increasing range from an acoustic source. This behavior is readily demonstrated with a monopole point source, which we can model as a harmonically pulsing sphere with radius a. Assuming a homogeneous medium with no boundaries (free-space), the pressure field is,

$$p(r;t) = A\frac{e^{ikr-iwt}}{r} \tag{2.12}$$

where r is the range from the center of the sphere, $\omega = 2\pi f$ is the circular frequency, and $k = \omega/c$ is the wavenumber. A is the complex amplitude given by,

$$A = a\left(\frac{ka}{ka+i}\right)\rho_0 c u_0 e^{-ika} \tag{2.13}$$

where u_0 is the amplitude of the radial velocity of the surface of the pulsing sphere [11]. The complex amplitude of a monopole point source is that of a sphere with $ka \ll 1$, in which case A is equal to $i\rho_0\omega a^2 u_0$.

The acoustic field of the point source exhibits spherical symmetry, and derivatives of Eq. 2.12 with respect to the angular coordinates are zero. Following Euler's equation (Eq. 2.3), the velocity field is,

$$v_r(r;t) = \frac{p(r;t)}{\rho_0 c}(1 + \frac{i}{kr}). \tag{2.14}$$

which in this case is only in the radial direction. The constant in the denominator, $\rho_0 c$, is the characteristic impedance of the medium. The acoustic impedance is defined as the ratio of the complex amplitude of the pressure and particle velocity. In general, the acoustic impedance is not constant and exhibits spatial dependence. The acoustic impedance of the point source defined in Eq. 2.12 and 2.14 is $\rho_0 c(1 + \frac{i}{kr})$, which depends on both the source frequency and the distance from the source.

Writing p in Eq. 2.12 and v_r in Eq. 2.14 in terms of sines and cosines, and taking the real part of their product as prescribed by Eq. 2.11, the radial instantaneous intensity, $S_r(r;t)$, of a point source is,

$$S_r(r;t) = \frac{A^2}{\rho_0 c}\frac{\cos^2[kr - wt]}{r^2} - \frac{A^2}{\rho_0 c}\frac{\sin[2kr - 2wt]}{2kr^3}. \tag{2.15}$$

As we can see, $S_r(r;t)$ contains two terms that have significantly different time averaged behavior.

The first term, which essentially is the squared pressure field divided by the characteristic impedance ($\rho_0 c$), has a non-zero time average. This term describes the energy that radiates away from the source and is called the active intensity. The second term, which is called the reactive intensity, has a zero time average and does not contribute to the total radiated energy. The additional factor of kr in the denominator of this term, relative to the active intensity, causes the reactive intensity to be insignificant at ranges greater than a few wavelengths from a point source.

2.4 Complex Acoustic Intensity

In general, the partitioning of $\vec{S}$ into active and reactive intensity (as observed in Eq. 2.15) requires knowledge of the phase of p and $\vec{v}$. The phase (and amplitude) of p and $\vec{v}$ are embodied in their complex representation. The complex representation of p and $\vec{v}$ from real measurements, $p_M(t)$ and $\vec{v}_M(t)$, can be formed by the Hilbert transform pair [3],

$$p(t) = p_M(t) + i\tilde{p}_M(t), \tag{2.16}$$

$$\vec{v}(t) = \vec{v}_M(t) + i\tilde{\vec{v}}_M(t), \tag{2.17}$$

where the tilde indicates the Hilbert transform of the original signal, which is

$$\tilde{p}_M(\tau) = \frac{1}{\pi}\int_{-\infty}^{\infty} \frac{p_M(t)}{t-\tau} dt, \tag{2.18}$$

for the pressure, and

$$\tilde{\vec{v}}_M(\tau) = \frac{1}{\pi}\int_{-\infty}^{\infty} \frac{\vec{v}_M(t)}{t-\tau} dt, \tag{2.19}$$

for the particle velocity.

The Hilbert transform of a measurement shifts the phase of all the frequency components by $\pi/2$. This can be implemented by changing the sign of the negative components of the Fourier transformed measurement, multiplying this result by $-i$, and then computing the inverse Fourier transform. For example, the function $\cos(\omega_0 t)$ has the Fourier transform $[\delta(\omega-\omega_0)+\delta(\omega+\omega_0)]$, which becomes $i[\delta(\omega+\omega_0)-\delta(\omega-\omega_0)]$ with inverse Fourier transform equal to $\sin(\omega_0 t)$. The Hilbert transform of $\cos(\omega_0 t)$ is thus $\sin(\omega_0 t)$, and its Hilbert transform pair is $\cos(\omega_0 t) + i\sin(\omega_0 t)$. The real part of complex p and $\vec{v}$ satisfy the relationship for the formulation of $\vec{S}(t)$ in Eq. 2.11.

Now, considering complex p and $\vec{v}$, the complex intensity is defined as,

$$\vec{I}_c(t) = \frac{p(t)\vec{v}(t)^*}{2} = \vec{I}(t) + i\vec{Q}(t)\ , \tag{2.20}$$

where the asterisk (*) indicates complex conjugation. The choice of the conjugated term is arbitrary, and does not affect the formulation of the active intensity envelope, which is,

$$\vec{I}(t) = Re\left\{\vec{I_c}(t)\right\} \ . \tag{2.21}$$

The active intensity envelope is the magnitude of the active intensity, representing the propagating, or time-averaged portion of $\vec{S}$. The factor 1/2 in Eq. 2.20 is required to equate the time average of $\vec{I}(t)$ to the time average of $\vec{S}(t)$. For example, consider a steady-state completely active intensity field defined by $p_M = \cos(\omega_0 t)$ and $\vec{v}_M = \cos(\omega_0 t)/\rho_0 c$. The product of their complex quantities, $p\vec{v}^*$, has no time dependence and is equal to $1/\rho_0 c$, a result double that of the time average of $\vec{S}(t) = \cos^2(\omega_0 t)/\rho_0 c$ over a period, $T = 2\pi/\omega_0$, where $\langle \vec{S}(t) \rangle_T$ is equal to $1/2\rho_0 c$.

The imaginary part of $\vec{I_c}(t)$ is the reactive intensity envelope,

$$\vec{Q}(t) = Im\left\{\vec{I_c}(t)\right\} \ , \tag{2.22}$$

The reactive intensity envelope represents the magnitude of the portion of $\vec{S}(t)$ that time-averages to zero. Although the time-average of reactive intensity is zero, the time average of $\vec{Q}(t)$ is not necessarily zero. This subtle distinction allows for analysis of reactive intensity in a time-average sense, and is an important feature of the complex intensity representation. The sign of $\vec{Q}(t)$ is arbitrary, as it represents the portion of $\vec{S}(t)$ that is both equally positive and negative. The sign is determined by the choice of which term, p or $\vec{v}$, is conjugated in the formulation of complex intensity. The choice to conjugate $\vec{v}$ in Eq. 2.20 establishes the convention that $\vec{Q}(t)$ points away from a point-source with time-dependence $e^{i\omega t}$; to maintain this convention for source with $e^{-i\omega t}$ time-dependence, a conjugation of Eq. 2.20 is required.

Since $\vec{I}(t)$ and $\vec{Q}(t)$ are derived from $\vec{S}(t)$, the time-dependence of the active and reactive intensity can be re-introduced to their respective envelopes to reconstruct the original $\vec{S}(t)$. For example, considering a narrow-band signal at center frequency f (bandwidth $B \ll f$), the two envelopes combine to form $\vec{S}(t)$ as,

$$\vec{S}(t) = \vec{I}(t)\cos^2(2\pi f t) + \frac{1}{2}\vec{Q}(t)\sin(4\pi f t). \tag{2.23}$$

The envelopes $\vec{I}(t)$ and $\vec{Q}(t)$ are time dependent quantities, and in a static environment are subject to fluctuations in source amplitude.

Briefly, to summarize the notation:

- $\vec{S}(t) = Re[p(t)]Re[\vec{v}(t)]$
- $\vec{I_c}(t) = \frac{1}{2}p(t)\vec{v}(t)^*$
- $\vec{I}(t) = Re[I_c(t)]$ such that $\langle \vec{I}\, \rangle_T = \langle \vec{S}\, \rangle_T$
- $\vec{Q}(t) = Im[I_c(t)]$

Let us proceed next with a demonstration of the time dependent behavior of $\vec{S}(t)$, $\vec{I}(t)$ and $\vec{Q}(t)$ in two characteristic regions of a source, the acoustic near-field and far-field. The data, shown in Figs. 2.1 and 2.2, are reproduced from experimental measurements made by Jacobsen [5] of the pressure, $p(t)$, and radial particle velocity, $v_r(t)$, caused by an acoustic source (loud-speaker) placed in a large, strongly damped room, which approximately represents a compact source (ka≪1) in free-field conditions.

The first set of measurements were taken directly in front of the loud speaker producing 250 Hz noise. Figure 2.1a shows how $p(t)$ and $v_r(t)$ (scaled by $\rho_0 c$) are 90° degrees out of phase. This phasing, and the relative amplitude of velocity exceeding $\rho_0 c$, is due to a significant imaginary component of the acoustic impedance because kr is not $\ll 1$.

Figure 2.1b shows the corresponding radial instantaneous intensity, $S_r(t)$ (solid line), calculated from the product of the $p(t)$ and $\vec{v}_r(t)$ measurements. The oscillatory behavior of $S_r(t)$ at this position looks like a sine wave at twice the frequency of the source, which is characteristic of near-field measurements, where the field is predominately reactive. The time-dependent amplitude of the oscillatory part of $S_r(t)$ is given by its reactive intensity envelope, $Q_r(t)$ (dashed line). As the reactive component of intensity oscillates both in the positive and negative direction, the sign of $\vec{Q}(t)$ does not signify a direction of energy propagation. Rather, the sign of $\vec{Q}$ points away from the source in the near-field following our convention established in the formulation of the complex intensity (Eq. 2.20). In more

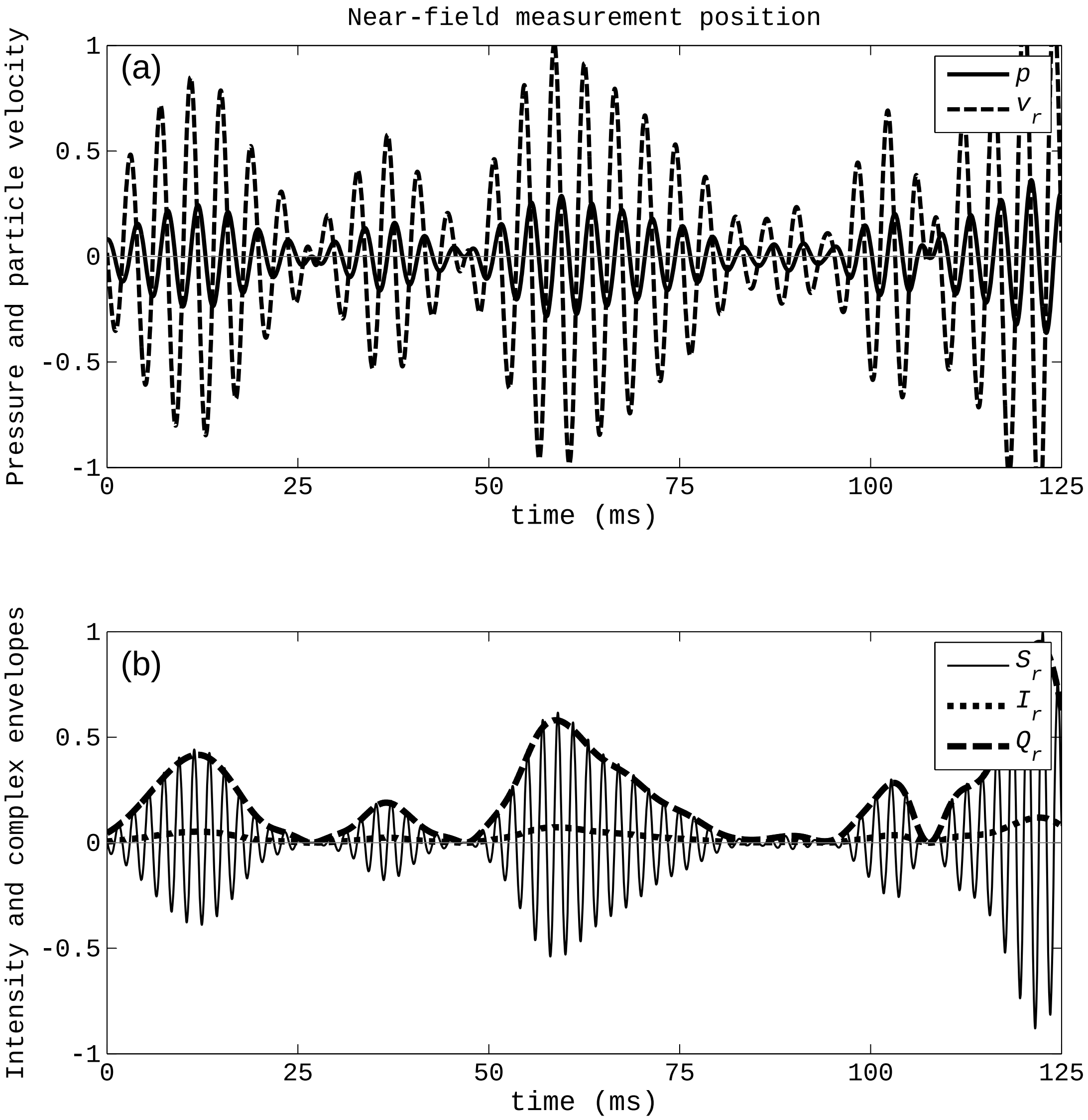

Figure 2.1: (a) Measurements of pressure (solid) and radial particle velocity (dashed), scaled by $\rho_0 c$, directly in-front of a speaker producing 250 Hz noise. (b) The radial component of the instantaneous intensity (solid), and the corresponding active (dashed) and reactive (dotted) intensity envelope. Figure reproduced from data collected by Jacobsen [5]

.

complicated sound-fields, an additional component of reactive intensity (perpendicular to the boundaries) will arise in regions of destructive interference, even when $kr \gg 1$.

Although the majority of the energy flux in the near-field time-averages to zero, a small portion of intensity (the active part) survives the time-average process and radiates to the far-field. Its time-dependent amplitude is given by the active intensity envelope, $I_r(t)$ (dotted line). The positive $I_r(t)$ indicates energy propagating away from the source. Note that where the apparent source amplitude has increased, so has the value of $\vec{I_r}$.

The second set of measurements were taken 30 cm in-front of the loud speaker, now producing 1000 Hz noise. Figure 2.2a now shows that $p(t)$ and $v_r(t)$ (scaled by $\rho_0 c$) are completely in-phase. Note that here the ratio of pressure and particle velocity is nearly equal to $\rho_0 c$.

Figure 2.2b shows the corresponding $S_r(t)$ (solid line), which at this position looks like a squared cosine wave at the source frequency. This is characteristic of the far-field instantaneous intensity in the free-field, where the amplitude of $S_r(t)$ is completely described by $I_r(t)$ (dotted line), and $Q_r(t) \approx 0$. It is clear that the time averages of the $S_r(t)$ and $I_r(t)$ are positive, indicating energy flux away from the source. The intensity can also be written in terms of its Cartesian vector components, where the sign of each component indicates energy flux in the positive or negative direction along each axis. The simple free-field analysis presented here suggests that when $kr \gg 1$, $\vec{I}(t)$ points away from the source and $p/|\vec{v}| = \rho_0 c$; these assumptions are no longer valid when boundaries (which cause reflections) are considered.

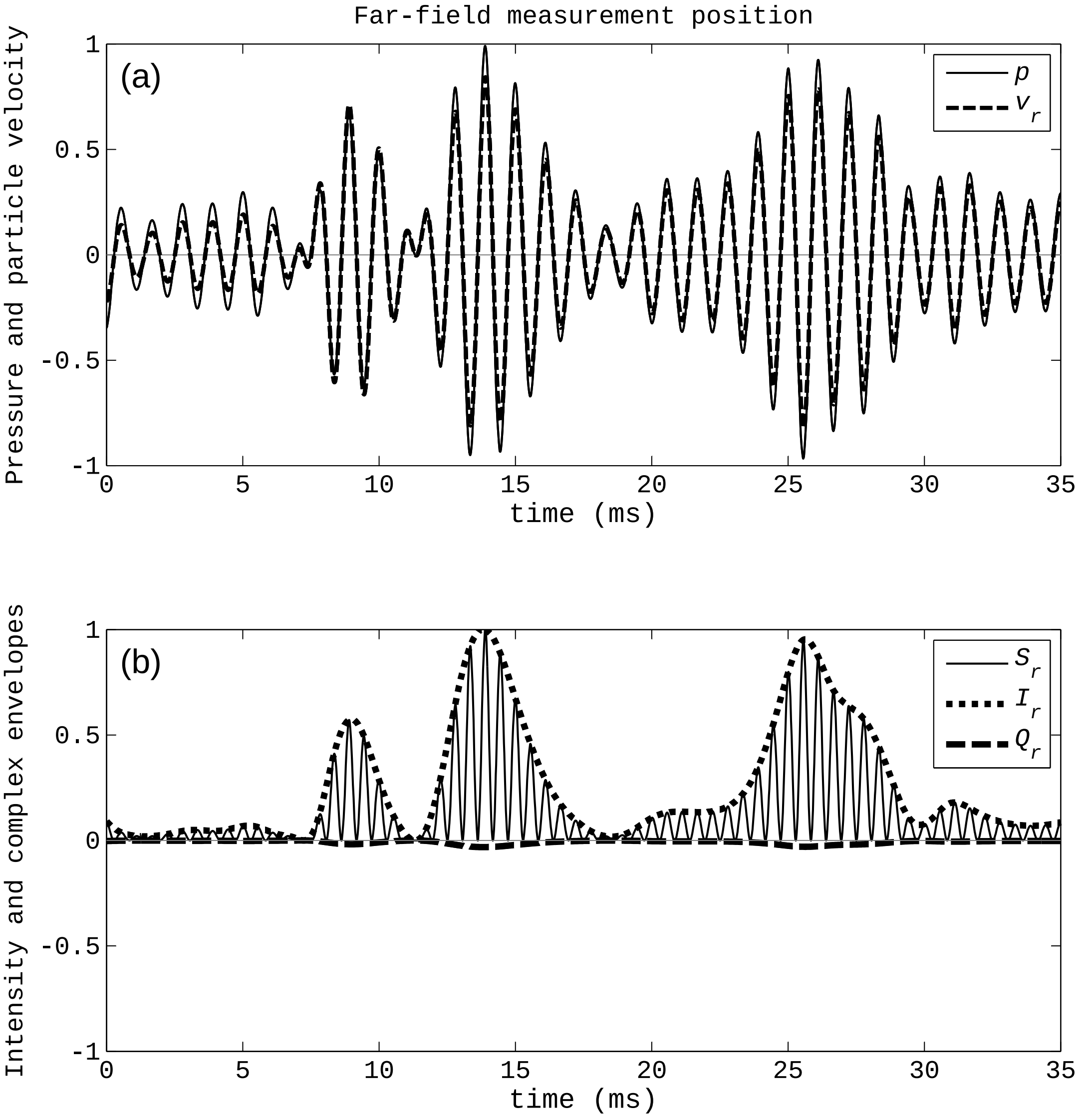

Figure 2.2: (a) Measurements of pressure (solid) and radial particle velocity (dashed), scaled by $\rho_0 c$, 30 cm in-front of a speaker producing 1000 Hz noise. (b) The radial component of the instantaneous intensity (solid), and the corresponding active (dotted) and reactive (dashed) intensity envelopes. Figure reproduced from data collected by Jacobsen [5]

.

Chapter 3

VECTOR PROPERTIES OF COMPLEX ACOUSTIC INTENSITY

3.1 Divergence of Active Intensity, $\nabla \cdot \vec{I}$

The time derivative of the total energy density ($w_{kin}+w_{pot}$) in a control volume describes the acoustic power, and power flow (i.e. intensity), within that volume. The conservation of energy equation, Eq. 2.10, equates divergence of instantaneous intensity, $\nabla \cdot \vec{S}$, associated with a control volume to acoustic power flow in or out of that volume. Positive $\nabla{\cdot}\vec{S}$ indicates acoustic power flow out of the control volume, and negative $\nabla \cdot \vec{S}$ indicates power flow into a control volume. A positive time-average of acoustic power flow, or time averaged $\nabla \cdot \vec{S}$, indicates acoustic power radiated out of a control volume by sources within the volume. If the control volume does not contain a source, the time averaged acoustic power flow into the volume is equal to the averaged power flow out of the volume (assuming no sound absorption occurs (as heat) within that volume), and $\nabla \cdot \vec{S} = 0$. As time averaged $\vec{S}$ is equal to time averaged $\vec{I}$, we can thus equate $\nabla \cdot \vec{I}$ to the total radiated power, W, of a volume as,

$$\int_V (\nabla \cdot \vec{I}) dV = W \tag{3.1}$$

Again, if the control volume does not contain a sound source, then both $\nabla \cdot \vec{I}$ and W are equal to 0. This condition holds for any size control volume that does not include a source, including a small control volume surrounding a single fluid particle.

One practical use of complex intensity measurements is to determine radiated acoustic power from a sound source. The acoustic power of a source is determined by measuring $\vec{I}$ on the surface of a control volume that surrounds (and includes) the source. Applying the divergence theorem to $\nabla \cdot \vec{I}$,

$$\int_V (\nabla \cdot \vec{I}) dV = \int_S (\vec{I} \cdot \vec{n}) dS, \tag{3.2}$$

the volume integral of $\nabla \cdot \vec{I}$ (i.e. the total power radiated out of the control volume) can

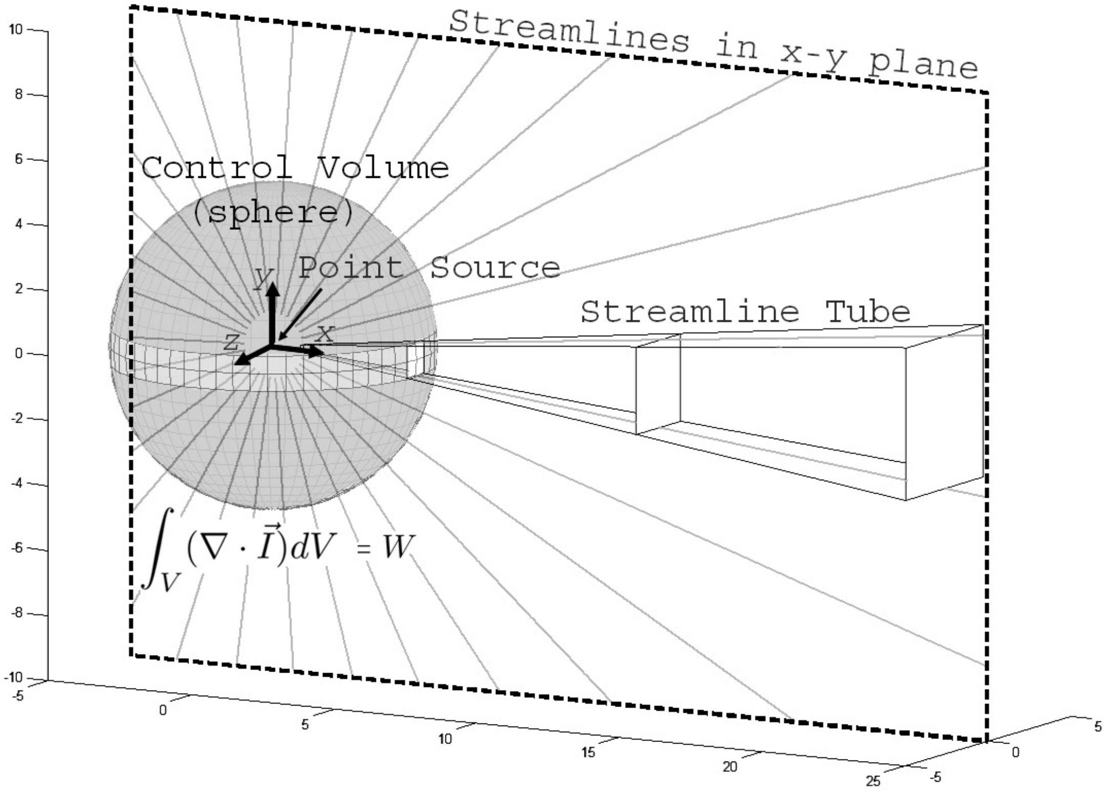

Figure 3.1: Intensity streamlines in the x-y plane, launched from an equal spacing from a point source in free-space. A streamline tube in three dimensions intersects the x-y plane as shown. The integral of $\nabla \cdot \vec{I}$ within a control volume surrounding the source (the sphere) is equal to the source power, W.

be determined by the surface integral of the $\vec{I}$ component normal to surface. The normal component of the $\vec{I}$ measurements are integrated over the surface of the control volume to yield the acoustic power, W.

3.1.1 Intensity Streamlines

The property that $\nabla \cdot \vec{I} = 0$ is analogous to an incompressibility approximation in fluid dynamics. This property allows for a representation of $\vec{I}$ by a stream-function, which can be used to construct streamlines to visualize energy flow. The intensity stream-function, Ψ, is defined as,

$$I_x = \frac{d\Psi}{dy}, I_y = \frac{d\Psi}{dx}, \tag{3.3}$$

where the direction of $\vec{I}$ is tangent to the streamline. Intensity streamlines can formed by two methods, either by plotting equal contours of Ψ, or by constructing streamlines directly from the intensity field.

The first method, plotting equal contours of Ψ, results in equally spaced streamlines. Equally spaced streamlines can be used to determine the energy flux through a control surface, simply by counting the number of streamlines passing through the area [12]. However, the explicit representation of Ψ can be difficult to compute and requires integration the intensity function, either numerically or analytically.

The second method, which results in unequally spaced streamlines, describes the energy propagation path (a streamline) initiated from some launch point. To construct the streamline, the direction of the intensity vector at the launch point is computed, and then the streamline is propagated a short distance in that direction. The direction is recalculated from the intensity field at the new position, and the process is repeated to form the streamline. These streamlines can be launched from any point and are quite useful in visualizing energy flow around complicated intensity features. Furthermore, the launch position of the streamlines can also be chosen such that the physical interpretation of equally spaced streamlines, discussed above, can be applied to unequally spaced streamlines.

To construct these approximately equal streamlines, the origin of the streamlines must have the same intensity magnitude. As discussed by Chapman in [13], this can be accomplished by choosing launch points close enough to the source, such that the field is not affected by interference due to reflections or other sources. This method is used to construct the streamlines depicted in this thesis, and allows for the construction of three-dimensional (3-D) streamlines which form the boundaries of a streamline tube. These streamline tubes represent the propagation path of a fixed amount of energy, and are discussed next.

3.1.2 Intensity streamline tubes

As an example, let us construct the intensity streamlines for the point source model described by Eq. 2.12 and 2.14. Writing the acoustic field in Cartesian coordinates with an origin at the center of the point source, the pressure is,

$$p(x, y, z) = \frac{e^{ik\sqrt{x^2+y^2+z^2}}}{\sqrt{x^2+y^2+z^2}} A e^{-i\omega t}, \tag{3.4}$$

and the particle velocity components are,

$$v_x(x, y, z) = \frac{p(x, y, z)}{\rho_0 c} \left(1 + i \frac{1}{k\sqrt{x^2+y^2+z^2}}\right) \frac{x}{\sqrt{x^2+y^2+z^2}}, \tag{3.5}$$

$$v_y(x, y, z) = \frac{p(x, y, z)}{\rho_0 c} \left(1 + i \frac{1}{k\sqrt{x^2+y^2+z^2}}\right) \frac{y}{\sqrt{x^2+y^2+z^2}}, \tag{3.6}$$

$$v_z(x, y, z) = \frac{p(x, y, z)}{\rho_0 c} \left(1 + i \frac{1}{k\sqrt{x^2+y^2+z^2}}\right) \frac{z}{\sqrt{x^2+y^2+z^2}}, \tag{3.7}$$

$$\tag{3.8}$$

Following Eq. 2.20, the active intensity components are,

$$I_x(x, y, z) = \frac{A}{\rho_0 c} \frac{x}{(x^2+y^2+z^2)^{\frac{3}{2}}}, \tag{3.9}$$

$$I_y(x, y, z) = \frac{A}{\rho_0 c} \frac{y}{(x^2+y^2+z^2)^{\frac{3}{2}}}, \tag{3.10}$$

$$I_z(x, y, z) = \frac{A}{\rho_0 c} \frac{z}{(x^2+y^2+z^2)^{\frac{3}{2}}}. \tag{3.11}$$

Figure 3.1 shows intensity streamlines for a point source in free space. The gray streamlines are launched from equally spaced increments on a circle in the x-y plane, with $z = 0$. This circle is centered on the point source and represents a contour of equal intensity magnitude, making these streamlines equivalent to equally spaced streamlines. In addition to these streamlines in the x-y plane, a three-dimensional streamline tube is shown. The boundaries of this streamline tube are established by the four black 3-D streamlines. There is no energy flow perpendicular to the boundary of the streamlie tube, and the energy flux through cross sectional areas of a streamline tube is constant.

The azimuthal symmetry of the point source model allows for a visualization of this streamline tube from the two-dimensional (2-D) streamlines shown in the x-y plane. The spreading of the tube in the azimuthal direction (out of plane, or z-direction in Fig. 3.1) depends only on the range from the source, and not the shape of the x-y streamlines. This feature will facilitate a 2-D representation streamline tubes in more complicated fields that exhibit azimuthal symmetry. The streamline tube is very similar to the concept of a ray tube description of intensity [14], where the cross-sectional area between to neighboring rays is proportional to the intensity. In this simple acoustic field, a point-source in the free-field, the rays and streamlines are identical.

While rays and streamlines are very similar, there are a few key differences. Rays are lines drawn perpendicular to the phase fronts of a wavefront, while streamlines are drawn parallel to the intensity vector. When there is only one wavefront passing though each field point, as is the case of the point source in the free-field (Fig. 3.1), the rays and streamlines are identical. When there are multiple wavefronts (or wavefront curvature due to refraction), more than one ray can pass through the same field point. On the other hand, intensity streamlines by definition will never overlap. This characteristic of streamlines is useful in identifying regions of destructive interference as streamlines appear to avoid these regions [15].

3.2 Divergence of Reactive Intensity, $\nabla \cdot \vec{Q}$

A complex representation of the conservation of energy can be formulated to represent its time-averaged behavior, although this representation must be consistent with that derived in Eq. 2.10 for real valued p and $\vec{v}$. Starting with Euler's equation as in Section 2.2, but now allowing for complex p and v, we have,

$$\frac{1}{2}\left[\rho_0 \frac{\partial \vec{v}}{\partial t} + \nabla p\right] \cdot \vec{v}^{\,*} = \frac{1}{2}\left[\rho_0 \frac{\partial \vec{v}}{\partial t} \cdot \vec{v}^{\,*} + \frac{1}{\rho_0 c^2}\frac{\partial p^*}{\partial t} p + \nabla \cdot p\vec{v}^{\,*}\right] = 0, \qquad (3.12)$$

And with the conservation of mass, we have,

$$\frac{1}{2}\left[\frac{\partial}{\partial t}\frac{p}{\rho_0 c^2} + \nabla \cdot \vec{v}\right] \cdot p^* = \frac{1}{2}\left[\rho_0 \frac{\partial \vec{v}^{\,*}}{\partial t} \cdot \vec{v} + \frac{1}{\rho_0 c^2}\frac{\partial p}{\partial t} p^* + \nabla \cdot p^* \vec{v}\right] = 0. \qquad (3.13)$$

Following Pascal [16], setting Eq. 3.12 equal Eq. 3.13 and assuming $e^{i\omega t}$ time dependence, we have,

$$i\frac{\rho_0 \omega (\vec{v} \cdot \vec{v}^*)}{2} - i\frac{\omega (pp^*)}{2\rho_0 c^2} + \nabla \cdot \vec{I_c} = -i\frac{\rho_0 \omega (\vec{v} \cdot \vec{v}^*)}{2} + i\frac{\omega (pp^*)}{2\rho_0 c^2} + \nabla \cdot \vec{I_c}^{\,*} \qquad (3.14)$$

The conjugation of the complex intensity changes only the sign of $\vec{Q}$. Rearranging the intensity terms to one side, and noting that $\nabla \cdot \vec{I_c} - \nabla \cdot \vec{I_c}^* = 2i\ \nabla \cdot \vec{Q}$, Eq. 3.14 simplifies to,

$$\nabla \cdot \vec{Q} = \frac{\rho_0 \omega (\vec{v} \cdot \vec{v}^*)}{2} - \frac{\omega (p p^*)}{2 \rho_0 c^2} \tag{3.15}$$

The terms on the right hand side are energy density quantities expressed with complex p and $\vec{v}$, representing their time-averaged behavior. To equate these complex representations to time-averages of w_{kin} and w_{pot} in Eq. 2.6 and 2.9, an additional factor of 1/2 is required, such that the kinetic energy density is,

$$\langle w_{kin} \rangle = \rho_0 \frac{\vec{v} \cdot \vec{v}^*}{4}, \tag{3.16}$$

and the potential energy density is,

$$\langle w_{pot} \rangle = \frac{1}{\rho_0 c^2} \frac{p p^*}{4}, \tag{3.17}$$

Writing 3.15 in terms of time-average energy quantities, we have

$$\nabla \cdot \vec{Q} = 2\omega [\langle w_{kin} \rangle - \langle w_{pot} \rangle], \tag{3.18}$$

From this derivation, it is apparent that the sign of $\vec{Q}$ corresponds to the relative magnitude of the kinetic and potential energy densities. Following our convention that $\vec{Q}$ points outward from a source, then a control volume surrounding a source with positive $\nabla \cdot \vec{Q}$ will have more kinetic energy than potential energy. As an example, consider the experimental measurements of a reactive field shown in Fig. 2.1, which shows that the kinetic energy exceeds the potential energy in the near field.

This sign convention of $\vec{Q}$ pointing outward from a source also establishes properties of interference fields, where regions of constructive interference have $\nabla \cdot \vec{Q} > 0$, and regions of destructive interference have $\nabla \cdot \vec{Q} < 0$. The acoustic field for a control volume that surrounds a destructive interference region is predominately the result of kinetic energy, i.e., $\langle w_{kin} \rangle$ exceeds $\langle w_{pot} \rangle$ as they both approach a minimum. In such destructive regions, a vector sensor which measures the particle velocity (and thus kinetic energy) may be best equipped to measure the acoustic field.

3.3 Curl of the Complex Intensity $\nabla \times \vec{I_c}$

The curl of complex intensity, $\nabla \times \vec{I_c}$, describes rotation of the intensity vector field, which can be non-zero in sound fields exhibiting constructive and destructive interference. Expanding $\nabla \times \vec{I_c}$ in terms of the pressure and particle velocity,

$$\nabla \times \vec{I_c} = \frac{1}{2}\left(p\nabla \times \vec{v}^{\,*} + \nabla p \times \vec{v}^{\,*}\right). \tag{3.19}$$

where the first term is zero as the particle velocity is defined as irrotational ($\nabla \times \vec{v} = 0$), the curl of complex intensity curl simplifies to,

$$\nabla \times \vec{I_c} = \frac{1}{2}\nabla p \times \vec{v}^{\,*}. \tag{3.20}$$

Expressing the pressure gradient in terms of the particle velocity via Euler's equation (Eq. 2.3), and assuming an $e^{i\omega t}$ time dependence, the curl of complex intensity can be written as,

$$\nabla \times \vec{I_c} = -\frac{i\omega\rho_0}{2}\,\vec{v} \times \vec{v}^{\,*}. \tag{3.21}$$

The curl of complex intensity is the result of phase differences between the individual velocity components, which can be shown by expressing the cross-product $\vec{v} \times \vec{v}^{\,*}$ in terms of its vector components, as

$$\vec{v} \times \vec{v}^{\,*} = \begin{vmatrix} \mathbf{i} & \mathbf{j} & \mathbf{k} \\ v_x & v_y & v_z \\ v_x^* & v_y^* & v_z^* \end{vmatrix} = \begin{bmatrix} (v_y v_z^* - v_z v_y^*)\mathbf{i} \\ (v_z v_x^* - v_x v_z^*)\mathbf{j} \\ (v_x v_y^* - v_y v_x^*)\mathbf{k} \end{bmatrix}. \tag{3.22}$$

When two components of $\vec{v}$ have the same phase, the sum of their conjugated pairs (e.g. $v_y v_z^* - v_z v_y^*$) will be zero. If two components differ by a constant phase $e^{i\phi}$, the sum of their conjugated pairs is the product of their magnitude times $2i \sin\phi$, which is equivalent to the corresponding component of $Im\left\{\vec{v} \times \vec{v}^{\,*}\right\}$ times $2i$.

Thus Eq. 3.21 simplifies to,

$$\nabla \times \vec{I_c} = \omega\rho_0 Im\left\{\vec{v} \times \vec{v}^{\,*}\right\}, \tag{3.23}$$

which is consistent with the derivation in Ref. [17]. The imaginary part of the cross-product, $Im\left\{\vec{v} \times \vec{v}^{\,*}\right\}$, can also be written as the cross-product $Re\left\{\vec{v}\right\} \times Im\left\{\vec{v}\right\}$ times 2, such that $\nabla \times \vec{I_c} = 2\omega\rho_0 Re\left\{\vec{v}\right\} \times Im\left\{\vec{v}\right\}$, which is consistent with the derivation in Ref. [18].

The curl of complex intensity can also be written in terms of the cross-product $I_c \times I_c$ by manipulation of the right side of Eq. 3.21 (multiplying it by pp^*/pp^*) giving,

$$\nabla \times \vec{I}_c = \frac{-i\omega\rho_0}{2}\frac{p\vec{v}^* \times p^*\vec{v}}{pp^*} = -2i\omega\rho_0\frac{\vec{I}_c \times \vec{I}_c^*}{pp^*}. \tag{3.24}$$

Expanding the cross product $I_c \times I_c$ as,

$$\vec{I}_c \times \vec{I}_c^* = \begin{vmatrix} \mathbf{i} & \mathbf{j} & \mathbf{k} \\ I_x + iQ_x & I_y + iQ_y & I_z + iQ_z \\ I_x - iQ_x & I_y - iQ_y & I_z - iQ_z \end{vmatrix} = 2i\,\vec{I} \times \vec{Q}, \tag{3.25}$$

the curl of the complex intensity in Eq. 3.24 simplifies to,

$$\nabla \times \vec{I}_c = 4\omega\rho_0\frac{\vec{I} \times \vec{Q}}{pp^*}, \tag{3.26}$$

which is consistent with the derivation in Ref. [19].

From Eq. 3.26, we can see that non-zero $\nabla \times \vec{I}_c$ requires the active and reactive intensity to be oriented in different directions. In the acoustic field of a point source in free-space, the active and reactive components are oriented in the same radial direction and $\nabla \times \vec{I} = 0$. This zero curl is visualized by the straight streamlines in Fig. 3.1. Similarly, the components of the particle velocity vector all have the same complex phase dependence and $\vec{v} \times \vec{v}^* = 0$.

Both the particle velocity formulation in Eq. 3.23, and intensity formulation in Eq. 3.26, result in a completely real quantity, and thus,

$$\nabla \times \vec{Q} = 0. \tag{3.27}$$

This zero curl property of $\vec{Q}$ is a feature of all vector fields that can be derived from a potential field, such as with sound where $p = i\omega\rho_0\phi$ and ϕ is the velocity potential [20]. The reactive intensity is proportional to $|p|^2$, and gradients in $|p|^2$ are the result of constructive and destructive interference due to multiple wavefronts. This is a very interesting property and is the subject to further study in Chap. 7.

At this point, we have now derived the basic vector properties of the complex intensity. Before moving onto an example, let us summarize. In a control volume that contains no sources and has constant ρ_0:

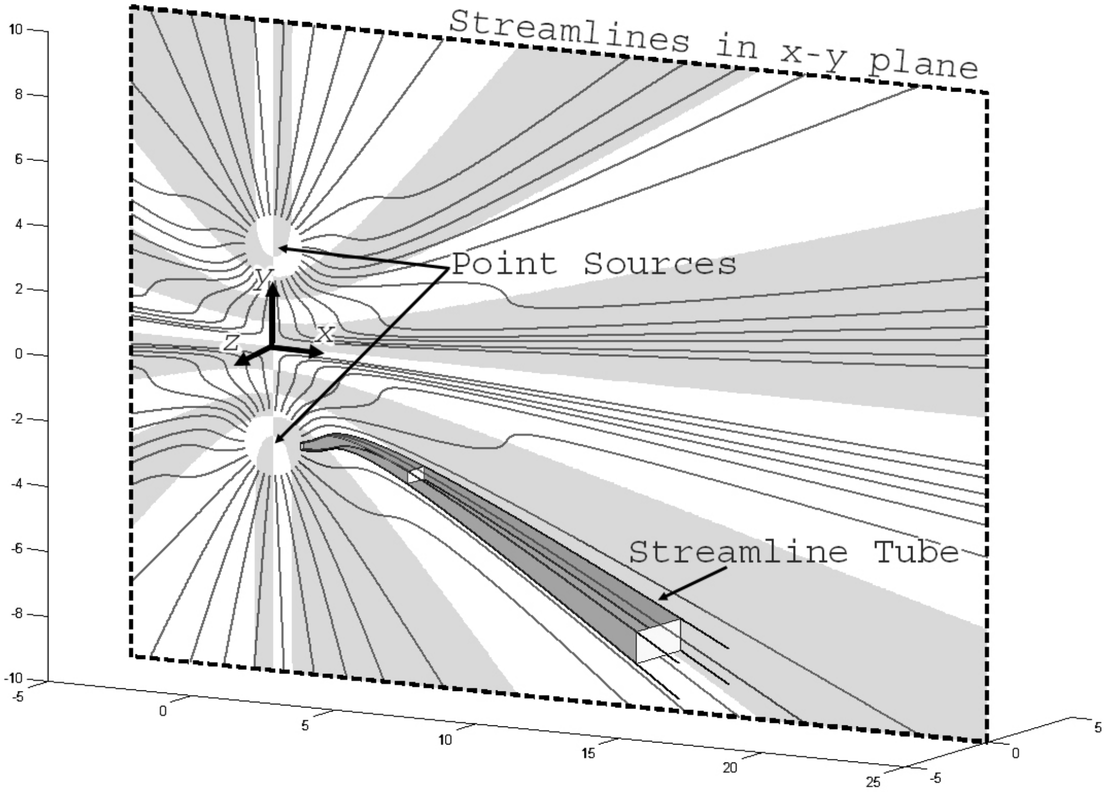

Figure 3.2: Equally spaced intensity streamlines plotted in the x-y plane of a field consisting of two 500 Hz coherent point sources in water. The sign of the z-component of $\nabla \times \vec{I}$ in the x-y plane is indicated by the white (positive) and gray (negative) regions. A streamline tube in three dimensions intersects the x-y plane as shown.

- $\nabla \cdot \vec{I} = 0$
- $\nabla \cdot \vec{Q} = 2\omega[\langle w_{kin} \rangle - \langle w_{pot} \rangle]$
- $\nabla \times \vec{I} = 4\omega\rho_0 \frac{\vec{I}\times\vec{Q}}{pp^*} = -\omega\rho_0 Im\left\{\vec{v} \times \vec{v}^*\right\}$
- $\nabla \times \vec{Q} = 0$

As a demonstration of non-zero $\nabla\times\vec{I}$, now consider the sound field consisting of two point sources of equal magnitude in a homogeneous medium, where the sources have the same amplitude, phase and time dependence. We can combine the individual representations of the two point sources, as defined in Eq. 3.4, into one equation. The pressure field is,

$$p(x,y,z;t) = \left[\frac{e^{-ikr_1}}{r_1} + \frac{e^{-ikr_2}}{r_2} \right] Ae^{i\omega t}, \tag{3.28}$$

$$\text{where} \quad r_1 = \sqrt{(x-x_1)^2 + (y-y_1)^2 + (z-z_1)^2},$$

$$\text{and} \quad r_2 = \sqrt{(x-x_2)^2 + (y-y_2)^2 + (z-z_2)^2},$$

where $[x_1, y_1, z_1]$ and $[x_2, y_2, z_2]$ are the position vectors of the two point sources, and A is a complex amplitude defined in Eq. 2.13. The components of particle velocity are computed from Eq. 3.2 with Euler's equation (Eq. 2.3), and are,

$$v_x(x,y,z;t) = \frac{A}{\omega\rho_0} \left[\frac{e^{-ikr_1}e^{i\omega t}}{r_1} \left(k + i\frac{1}{r_1} \right) \frac{\partial r_1}{\partial x} + \frac{e^{-ikr_2}e^{i\omega t}}{r_2} \left(k + i\frac{1}{r_2} \right) \frac{\partial r_2}{\partial x} \right] \tag{3.29}$$

$$v_y(x,y,z;t) = \frac{A}{\omega\rho_0} \left[\frac{e^{-ikr_1}e^{i\omega t}}{r_1} \left(k + i\frac{1}{r_1} \right) \frac{\partial r_1}{\partial y} + \frac{e^{-ikr_2}e^{i\omega t}}{r_2} \left(k + i\frac{1}{r_2} \right) \frac{\partial r_2}{\partial y} \right] \tag{3.30}$$

$$v_z(x,y,z;t) = \frac{A}{\omega\rho_0} \left[\frac{e^{-ikr_1}e^{i\omega t}}{r_1} \left(k + i\frac{1}{r_1} \right) \frac{\partial r_1}{\partial z} + \frac{e^{-ikr_2}e^{i\omega t}}{r_2} \left(k + i\frac{1}{r_2} \right) \frac{\partial r_2}{\partial z} \right], \tag{3.31}$$

where the derivatives,

$$\frac{\partial r_1}{\partial x} = \frac{x - x_1}{\sqrt{(x-x_1)^2 + (y-y_1)^2 + (z-z_1)^2}} \tag{3.32}$$

$$\frac{\partial r_1}{\partial y} = \frac{y - y_1}{\sqrt{(x-x_1)^2 + (y-y_1)^2 + (z-z_1)^2}} \tag{3.33}$$

$$\frac{\partial r_1}{\partial z} = \frac{z - z_1}{\sqrt{(x-x_1)^2 + (y-y_1)^2 + (z-z_1)^2}} \tag{3.34}$$

$$\frac{\partial r_2}{\partial x} = \frac{x - x_2}{\sqrt{(x-x_2)^2 + (y-y_2)^2 + (z-z_2)^2}} \tag{3.35}$$

$$\frac{\partial r_2}{\partial y} = \frac{y - y_2}{\sqrt{(x-x_2)^2 + (y-y_2)^2 + (z-z_2)^2}} \tag{3.36}$$

$$\frac{\partial r_2}{\partial z} = \frac{z - z_2}{\sqrt{(x-x_2)^2 + (y-y_2)^2 + (z-z_2)^2}}. \tag{3.37}$$

Let us examine the field of two 500 Hz sources located two wavelengths apart. We can take advantage of the azimuthal symmetry of this field by choosing the origin of our Cartesian coordinate system to be at the midpoint between the two sources. Setting the origin to have the y-direction pointing toward one source, we have $[x_1, y_1, z_1]$=$[0, \lambda, 0]$ and $[x_2, y_2, z_2] = [0, -\lambda, 0]$. This field is azimuthally symmetric and looks identical in either the

x-y and y-z planes. The active intensity streamlines (black lines) were launched from a circumference surrounding each of the sources, allowing for their interpretation as equally spaced streamlines.

The interference between the two sources causes positive or negative $\nabla \times \vec{I}$, and transitions from positive to negative correspond to a change in the curvature of the streamlines. To simplify the visualization of curl, Fig. 3.2 only shows positive (white) and negative (gray) regions of the z-component of $\nabla \times \vec{I}$ in the x-y plane ($z = 0$). These regions, and the curvature of the intensity streamlines, depend on the frequency of the source. For example, if the frequency were increased to 1000 Hz (and the source positions unchanged), $\nabla \times \vec{I}$ would have twice the number of positive/negative transitions over which the streamlines would curve back and forth.

Figure 3.3 shows an enlargement of the x-y plane in Fig. 3.2, to demonstrate how the sign of $\nabla \times \vec{I}$ corresponds to the geometry of a streamlines. The curl of the active intensity in a section between two neighboring streamlines can be determined by their geometry by application of Stokes' theorem,

$$\int_A (\nabla \times \vec{I}) \cdot \vec{n} \ dA = \oint_C \vec{I} \cdot d\vec{r}, \tag{3.38}$$

which states that average $\nabla \times \vec{I}$ normal to an area is equal to the circulation of active intensity around its circumference.

Figure 3.3 shows the path of the line integral for two sections; the direction of the line integral is shown by the arrowheads. The line integral of each section can be broken into four segments. The two segments that connect the two neighboring streamlines are perpendicular to the direction of $\vec{I}$, and therefore do not contribute to the integral. The two streamlines do contribute to the integral, and their length is proportional to their integrated intensity. In the region labeled positive curl, the longer length segment corresponds to the intensity in the direction of integral. In the region labeled negative curl, the longer length opposes the integration path. We will continue with this two point source example in the next chapter in a discussion on acoustic particle motion, where a property of particle velocity will be shown to relate directly to $\nabla \times \vec{I}$.

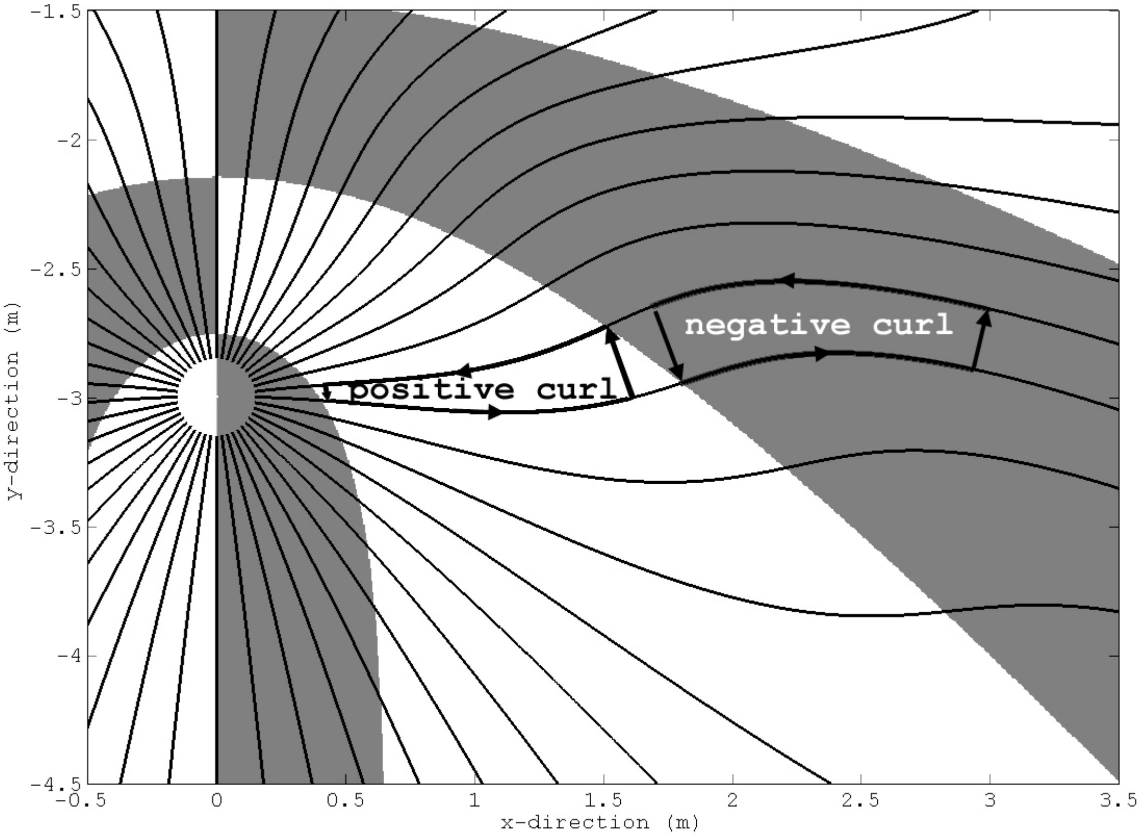

Figure 3.3: Streamlines corresponding to Fig. 3.2, and the integration path for two regions of a streamline tube. The length of the streamline between the two cross-sectional segments is proportional to the integrated intensity, longer lengths having a larger contribution to the integral.

Chapter 4

VECTOR PROPERTIES OF ACOUSTIC PARTICLE VELOCITY

This chapter presents a formulation for the degree of circularity, a non-dimensional vector property, which originates from "Elliptical Particle Motion in Underwater Waveguides," accepted by the Journal of the Acoustical Society of America for publication in July, 2013. The degree of circularity describes a characteristic of particle motion in an acoustic field. For a single frequency steady-state acoustic field, the path a particle follows has one of three canonical shapes: a line, a circle, or an ellipse. The particle will repeatedly pass through the same position on this path once each period.

By tracking the motion of fluid particles with a neutrally buoyant sensor, the shape of the particle motion path, and the direction the particle travels along its path, i.e., its polarization, can be directly measured. Measurements of the particle velocity, $\vec{v}$, or the complex intensity, $\vec{I_c}$, can be used to formulate a non-dimensional parameter describing the shape, called the degree of circularity, $\vec{\Theta}$. Controlled laboratory measurements of $\vec{\Theta}$ are presented in Chapter 5, and are compared to an approximate formulation, $\tilde{\Theta}$, derived in this chapter. This approximate formulation is applied in Chapter 6 to vertical intensity measurements in the ocean to determine properties of layered seabed.

4.1 Elliptical Particle Motion

As a demonstration of elliptical particle motion, let us again consider the acoustic field discussed in Fig. 3.2 consisting of two 500 Hz point sources. To take advantage of the azimuthal symmetry, the coordinate system is chosen to be the same as in Fig. 3.2. Figure 4.1 shows contours of equal velocity magnitude in the x-y plane (given in Eq. 3.29, 3.30 and 3.31). In the x-y plane, the velocity component $v_z(x, y, 0; t) = 0$. The circles on the thick contour line in Fig. 4.1 indicate two regions where the particles have identical velocity magnitude, but follow a different shaped path, a line and an ellipse.

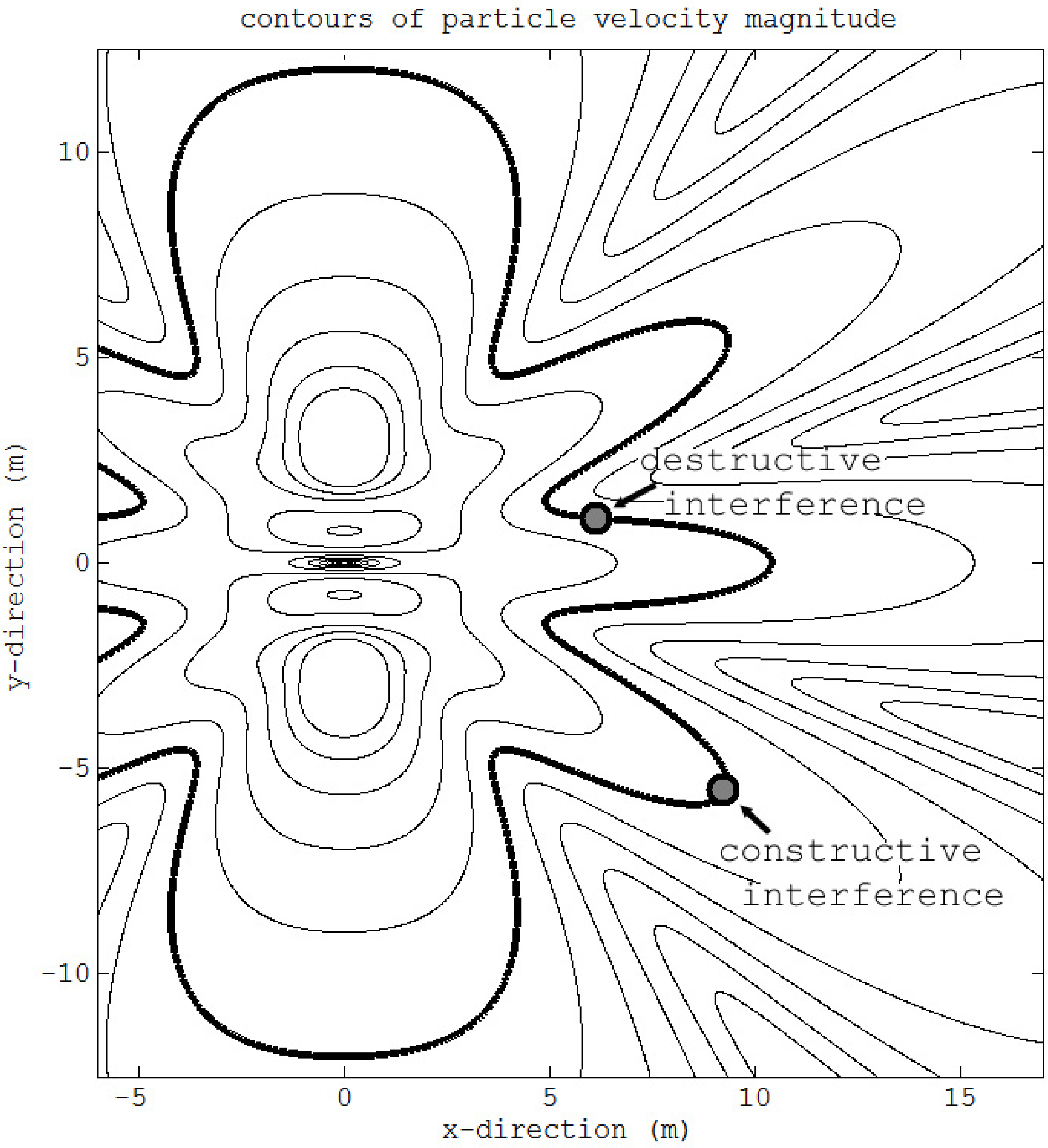

Figure 4.1: Contours of equal particle velocity magnitude for two 500 Hz point sources in water separated by 2 wavelengths (6 m). Two regions which have the same velocity magnitude, indicated by the circles on the bold contour, correspond to the region of constructive interference, discussed in Fig. 4.2, and a region of destructive interference, discussed in Fig. 4.3.

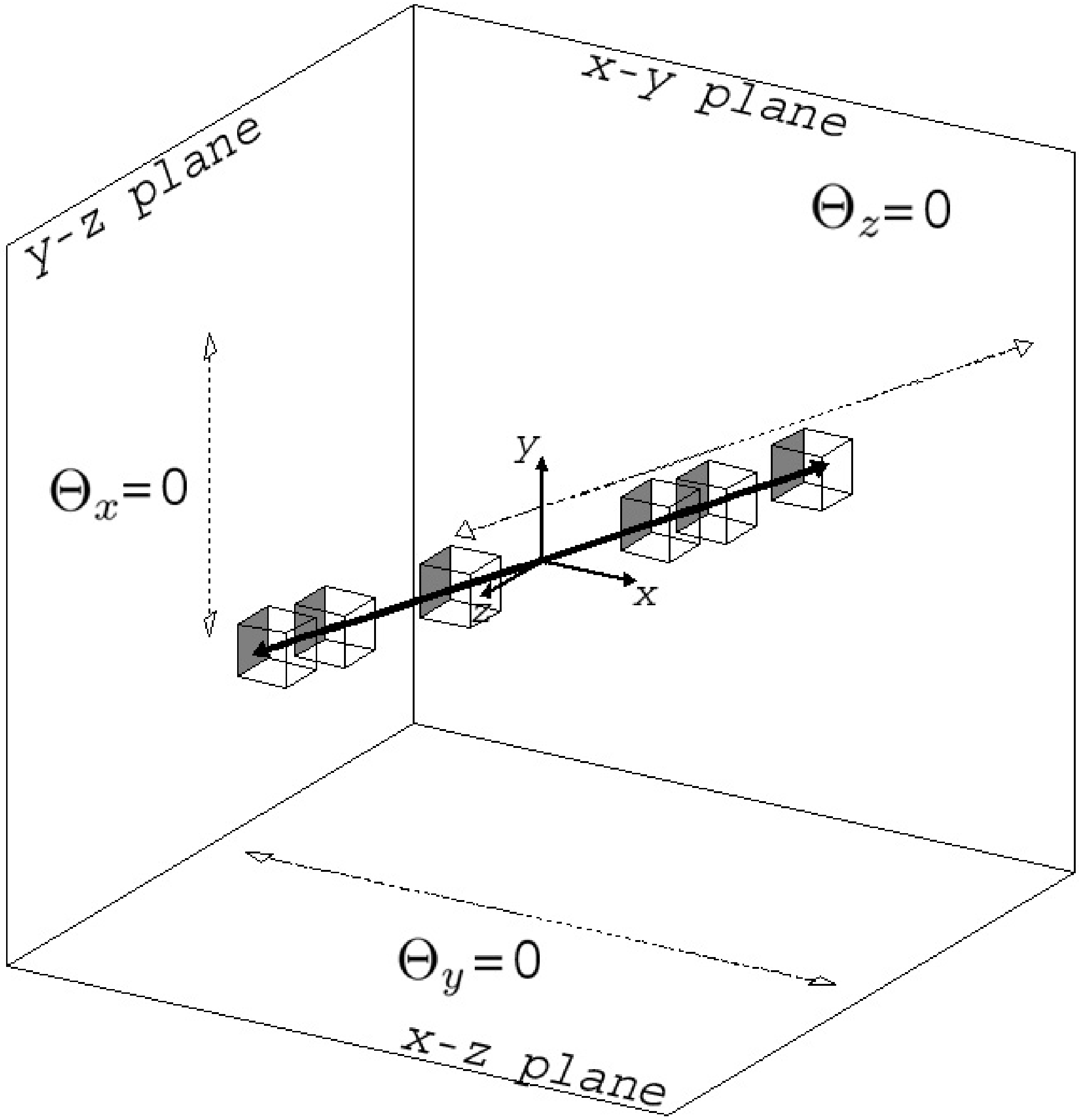

Figure 4.2: Particle motion of the constructive region indicated in Fig. 4.1 projected onto three orthogonal planes. The cubes correspond to the fluid motion of a small volume at sequential times spanning one period. One face of the cube is darkened to mark its orientation.

Figure 4.2 shows the acoustic motion associated with a small volume of fluid (a cube) located in the constructive region identified in Fig. 4.1. In this plot, the origin of the Cartesian coordinate system is centered at the equilibrium position of the cube. If there were no sound, the cube would be centered and remain at the origin. The x-y axes of Fig. 4.2 are oriented in the same direction as in the original x-y coordinates defined in Fig. 4.1.

The sound from the 500 Hz sources causes the cube to move along a path. Each cube in Fig. 4.2 represents the same volume at sequential times over one period. The vertices of each cube are computed explicitly by their acoustic displacement, determined by time integration of the velocity components given in Eq. 3.29, 3.29 and 3.31. The center of the cube traces out a path in three dimensions, which is shown by the bold line in Fig. 4.2. This 3-D path is projected onto three orthogonal planes in Fig. 4.2 (dotted lines). In this region of constructive interference, the particles (or cube) follow a back and forth oscillation along the line which lies in the x-y plane. The motion caused by constructive interference is similar to what we would expect from a single point source.

Figure 4.3 shows the motion associated with particles located in the destructive region identified in Fig. 4.1. Here, the fluid particles exhibit uniform motion around an elliptical path. The path traced out by the center of the cube is an ellipse shown by the bold line, which is projected on the three orthogonal planes (dotted lines). As the z-component of velocity is zero due to the azimuthal symmetry, the motion projected on the x-z plane is a line in the x direction, and similarly in the y direction for the y-z plane. The elliptical path is completely described by the projection on the x-y plane, and the direction of travel around the ellipse (its polarization) is indicated by the arrowhead. The basic geometry of the ellipse defines the degree to which the ellipse resembles a circle, or its circularity. Its circularity is twice the product of the major and minor axes of the ellipse, divided by their squared sum; hence circularity is a non-dimensional measure. When the particle motion falls on a straight line, there is no minor axis and the circularity is zero. Formulations of the degree of circularity, $\vec{\Theta}$, which describes circularity and its polarization, are presented in the next section.

It may be useful to clarify the angular momentum associated with this elliptical acoustic motion. As mentioned earlier, the linear acoustic field is irrotational, i.e., $\nabla \times \vec{v} = 0$, which

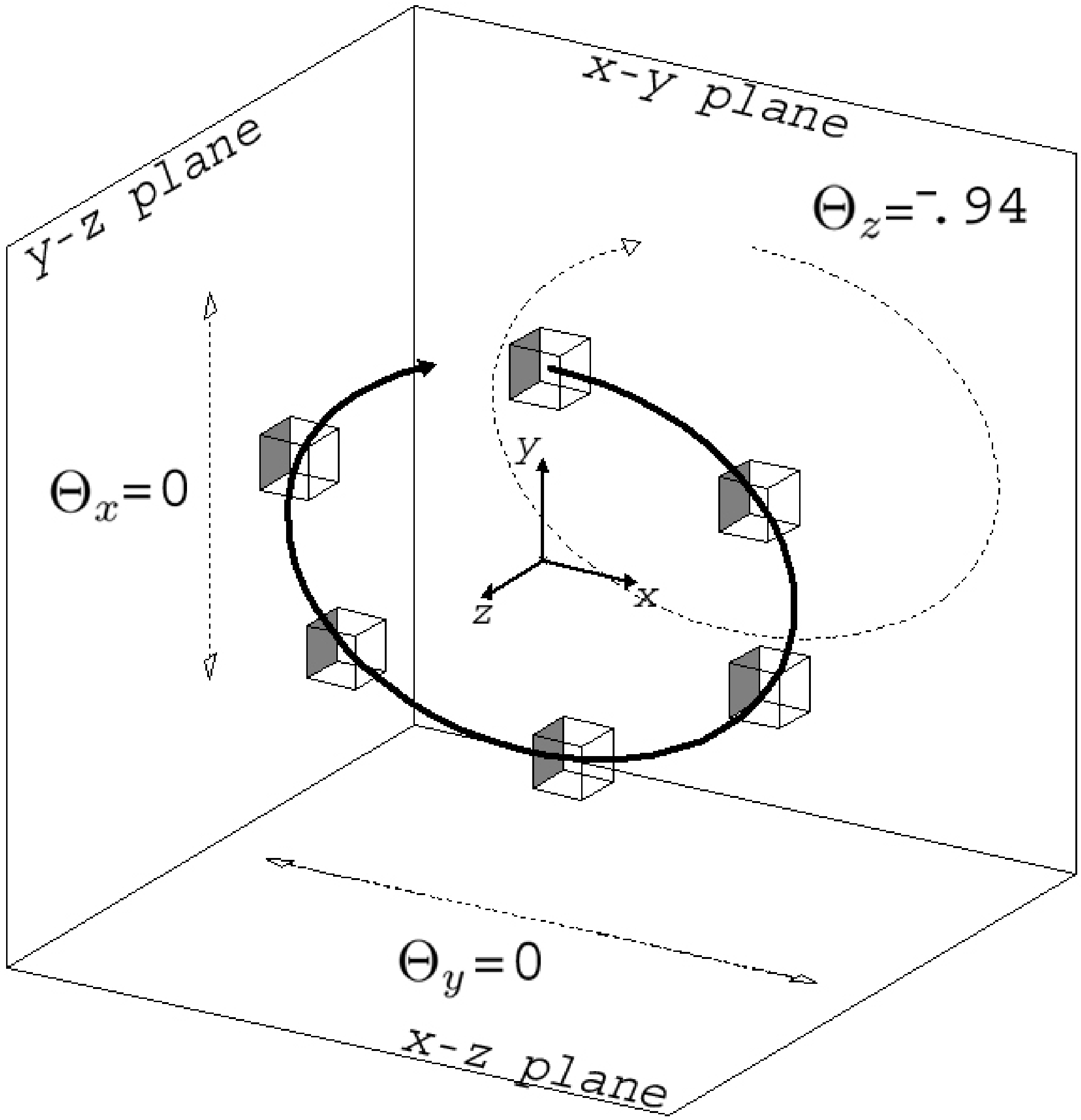

Figure 4.3: Particle motion of the destructive region indicated in Fig. 4.1 projected onto three orthogonal planes. The cubes correspond to the elliptical fluid motion of a small volume at sequential times spanning one period. One face of the cube is darkened to mark its orientation.

implies that there is no angular momentum. As shown in Fig. 4.2 and 4.3, the darkened face of the cube always points to the left, and thus the particle has zero net angular velocity and no angular momentum. As stated by Chun Lee et al. [21], "the circular motion is irrotational, such that, when an infinitesimal lump of the medium moves in a closed little loop, it must also spin in the opposite direction to keep the net angular momentum zero." In other words, since the orientation of the darkened face does not change, but the direction of travel does change, there is in effect a spin.

A neutrally buoyant sensor will also exhibit elliptical motion when placed in a destructive interference region. Although the displacements are seemingly imperceptible (on the order of 10^{-10} m for an rms pressure of 1 Pa at 1000 Hz), the accelerations associated with this motion (on the order of 10^{-3} m/s^2) can still be measured with a triaxial accelerometer, as is demonstrated in Chapter 5. These measurements of particle motion can be used to formulate the degree of circularity, $\vec{\Theta}$, to characterize the shape and polarization of particle motion.

4.2 The degree of circularity, $\vec{\Theta}$

4.2.1 $\vec{\Theta}$ computed via particle velocity, $\vec{v}$

The magnitude and phase relationship among the individual components of the complex particle velocity, v_i, can be used to construct a vector quantity, the degree of circularity [17],

$$\vec{\Theta} = 2\,\frac{Im(\vec{v} \times \vec{v}^*)}{|\vec{v}|^2}, \tag{4.1}$$

where the factor of 2 sets the bounds of any component of $\vec{\Theta}$ between ± 1. The phase relationship between the velocity components is given by the imaginary component of the cross product, $\vec{v} \times \vec{v}^*$, which is completely real when the velocity components are in phase (as demonstrated in Eq. 3.22). Each vector component of $\vec{\Theta}$ quantifies the degree to which the particle motion, projected on three orthogonal planes, resembles a circle.

When any two components of the particle velocity have the same phase, the particle motion in the plane of the two corresponding axes falls on a straight line. When the motion in a plane falls along a straight line, the corresponding value of $\vec{\Theta}$ is equal to zero. This is exemplified in the region of constructive interference in Fig. 4.2, where the x and y components of particle velocity are in phase. Here, the component of $\vec{\Theta} = [\Theta_x, \Theta_y, \Theta_z]$ corresponding to particle motion in the x-y plane, Θ_z, is equal to zero.

If two components of particle velocity are offset by a constant phase, the particle motion does not fall on a straight line. When the particle motion in a plane falls along a circle, the corresponding value of $\vec{\Theta}$ is equal to ± 1. When $0 < \vec{\Theta} < 1$ or $-1 < \vec{\Theta} < 0$, the motion will fall along an ellipse. This elliptical motion is exemplified in the region of destructive interference in Fig. 4.3, where Θ_z is equal to -0.94. The sign of $\vec{\Theta}$ corresponds to the direction, or polarization, a particle moves about its path with respect to a central point. Positive valued $\vec{\Theta}$ represents counterclockwise motion and negative valued $\vec{\Theta}$ represents clockwise motion. This distinction is further clarified in the context of Chapter 5 using both an analytic model and experimental data from a laboratory experiment.

4.2.2 $\vec{\Theta}$ computed from complex intensity, $\vec{I_c}$

The vector $\vec{\Theta}$, can also be derived from the complex intensity vector, $\vec{I_c}$. This allows for an approximation based on measurements of only one component of particle velocity, which is explained subsequently. The formulation of $\vec{\Theta}$ (equivalent to Eq. 4.1) based on the complex intensity is,

$$\vec{\Theta} = 2\,\frac{\vec{I} \times \vec{Q}}{|\vec{I}|^2 + |\vec{Q}|^2}, \tag{4.2}$$

Note that reactive intensity is very closely linked to elliptical particle motion: when $|\vec{Q}| = 0$, the degree of circularity is zero; when $|\vec{Q}| > 0$, the sign of the reactive intensity relates directly to the particle motion polarization. Furthermore, note how Eq. 4.2 compares to the complex intensity formulation of $\nabla \times \vec{I}$ in Eq. 3.26.

4.2.3 Approximation of $\vec{\Theta}$ component in the vertical plane

The sound fields discussed in this thesis are assumed to exhibit azimuthal symmetry, i.e., particle motion lies only in the r-z plane. Only one component of the vector $\vec{\Theta} = [\Theta_r, \Theta_z, \Theta_\Theta]$ in cylindrical coordinates is non-zero, (Θ_Θ). Therefore, for azimuthally symmetric fields, the vector notation will be dropped and the degree of circularity will be denoted as Θ.

An approximation to Θ can be derived from two vertically separated pressure measurements. This approximation relies on an accurate estimate of the complex horizontal intensity. The horizontal active intensity can be estimated by vector subtraction of the vertical component of active intensity from the total active intensity, where the total active intensity is approximated here by the pressure magnitude squared, divided by the characteristic impedance, $\rho_0 c$. The resulting approximate horizontal active intensity is,

$$\tilde{I_r} = \sqrt{\left(\frac{|p|^2}{\rho_0 c}\right)^2 - {I_z}^2}, \tag{4.3}$$

where I_z is the vertical intensity, and the tilde ($\sim$) indicates an approximate value of the horizontal intensity, I_r.

In regions of strong destructive interference, the magnitude of the total active intensity may be underestimated when $|p|/|\vec{v}|$ does not equate to $\rho_0 c$. The approximation of total intensity used in Eq. 4.3 is appropriate, as long as the interfering waves do not cause complete destructive interference. Complete destructive interference occurs when the active intensity of the interfering waves have a vector component of opposite sign, causing a complete cancellation of the acoustic field. This is often encountered in shallow water at long ranges, where the multiple upward and downward propagating waves set up standing waves in the vertical direction, creating a null or dislocation. Dislocations in ocean waveguides are discussed further in Chapter 7.

The horizontal component of reactive intensity, Q_r, is virtually zero a few wavelengths from the source, i.e., when $kr >> 1$. Substituting $\tilde{I_r}$ from Eq. 4.3 and $\tilde{Q_r} = 0$ for the appropriate quantities in Eq. 4.2, the approximate degree of circularity is,

$$\tilde{\Theta} = 2\frac{Q_z \tilde{I_r}}{{I_z}^2 + \tilde{I_r}^2 + {Q_z}^2}, \tag{4.4}$$

The approximate degree of circularity, $\tilde{\Theta}$, captures the dominant features of the exact Θ, given that the reflections are from horizontal boundaries such that reactive intensity is predominately in the vertical direction, i.e., along the z-axis.

Most importantly, $\tilde{\Theta}$ can be formed from two closely spaced hydrophones, extending this analysis of particle motion to observations made by a vertical line array of hydrophones. The hydrophone spacing must be less than $\lambda/4$ for an accurate estimation of particle velocity by the the finite difference approximation. The accuracy of the approximate $\tilde{\Theta}$, as computed by two hydrophones, is dependent not only on the accuracy of the finite-difference estimate of particle velocity, but also on the accuracy of the assumption that $|p|/|\vec{v}|$ equals $\rho_0 c$. To reiterate, the approximation in Eq. 4.4 will have the same sign (positive or negative) as the exact value of Θ, as long as the magnitude of the vector component of complex intensity does not exceed $|p|^2/\rho_0 c$.

Chapter 5

VECTOR SENSOR MEASUREMENT SYSTEMS

Vector sensors are acoustic sensors that can measure the particle motion feature of sound. Such particle motion sensors can be paired with a hydrophone, forming a combined sensor capable of measuring the acoustic intensity vector. There are a number of techniques which can be used to measure the particle motion in acoustic fields. For example, acoustic particle velocity can be detected using measurements of Doppler shifted laser light scattered from the medium, caused by the fluid motion, [22]. Particle velocity can also be detected by monitoring the change in resistance of a pair of heated wires, caused by the transfer of heat from one wire to the other by the fluid motion induced by the acoustic field, as used in the MEMs (Microelectromechanical) device described in [23]. Particle acceleration can be detected by measuring the acceleration of the rigid sensor, caused by the pressure gradients in the acoustic field. In this chapter, the design, construction and operating principles of accelerometer-based vector sensors are discussed.

Spatially separated hydrophone measurements can also be used to measure particle motion by an approximation to the pressure gradient in Euler's equation (Eq. 2.3). The core measurement and analysis effort in this thesis, presented in Chapters 6 and 7, utilizes this technique to compute the complex intensity from a vertical line array of hydrophones. The pressure gradient is approximated by the difference of the two hydrophone signals, divided by their separation. This pressure gradient is scaled by $1/\rho_0$ and time integrated to yield the component of particle velocity along the axis separating the two sensors, centered at the midpoint. The pressure field at the midpoint is calculated by the average of the two pressure signals. The validity of the approximation (discussed in Chapter 7) depends on the frequency, and the spatial separation between the hydrophones must be less than $\lambda/4$.

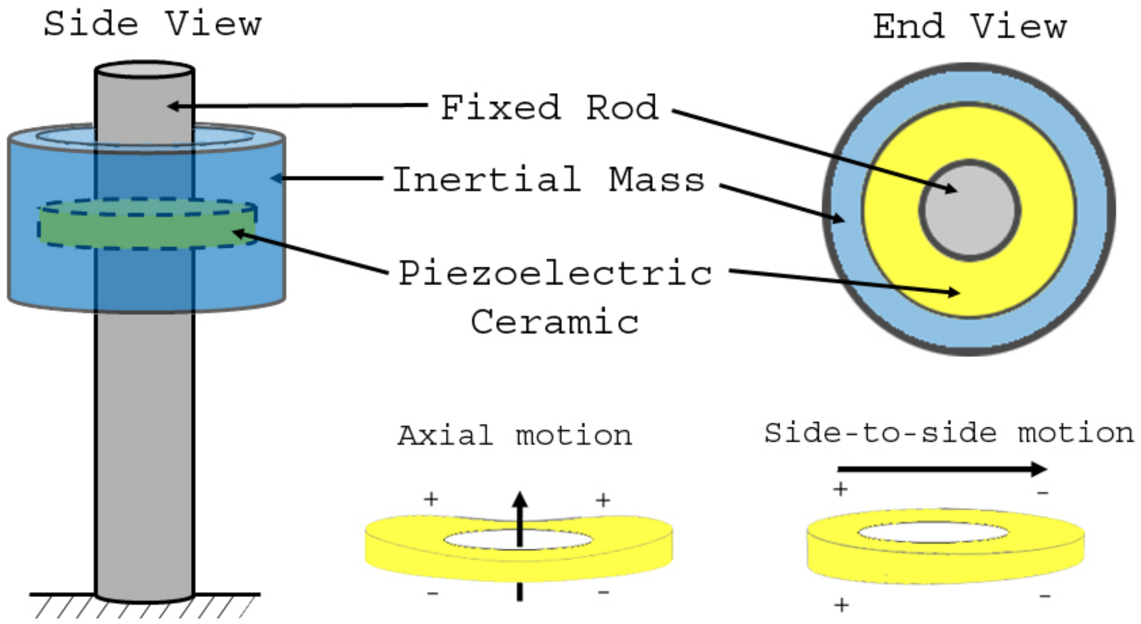

Figure 5.1: Diagram of a uni-directional accelerometer. The + and - relate to the charge developed on faces of piezoelectric wafer due to flexing, caused by relative motion of the inertial mass (shown by the arrows).

5.1 Accelerometer-based Vector Sensors

Accelerometer-based vector sensors operate on the premise of measuring the acceleration of the physical sensor housing, caused by the acoustic motion of the surrounding fluid. An accelerometer measures a signal proportional to the inertial force exerted by a mass within the sensor housing. Triaxial accelerometers consist of three unidirectional accelerometers, mounted to the accelerometer housing along the three Cartesian axes. Figure 5.1 shows a diagram of one unidirectional accelerometer, which consists of a small (inertial) mass, a piezoelectric ceramic wafer and a fixed rod (attached to the sensor housing). The ceramic wafer is pressed between the inertial mass and fixed rod, suspending the inertial mass relative to the fixed rod (the mass and rod do not touch). The ceramic acts like a stiff spring, creating a mass-spring system which typically has a natural frequency greater than 10 kHz.

The movement of the inertial mass, relative to the sensor housing, exerts a force on the piezoelectric ceramic, causing it to deflect. Due to the piezoelectric effect, the deflection causes an equal and opposite charge to develop on the compressed and stretched face of the ceramic. The unidirectional accelerometer shown in Fig. 5.1 is designed such that sensor responds only to acceleration in the axial direction. Axial motion produces flexing of the ceramic in one direction, and thus a positive and negative charge develops on opposite faces of the ceramic. When side-to-side motion occurs (perpendicular to the measurement axis), the mass simultaneously compresses and stretches both faces of the ceramic, resulting in zero net charge on each face.

The electrical impedance of the wafer is high, and to sense the signal, a charge amplifier with a high input impedance is typically included within the sensor housing, acting as a buffer amplifier. The charge amplifier is electrically connected to one face of the piezoelectric ceramic, and is grounded to the sensor housing. The amplifier lowers the output impedance of the sensor (and amplifies it) to drive the signal wire, which can be recorded by a data acquisition system. The voltage from the charge amplifier is proportional to the force exerted by the mass within the linear operating range of the accelerometer, through $F = ma$.

As part of this graduate research, a portable vector acoustic measurement system was constructed based around a triaxial accelerometer. The single rational for this effort was to better understand the operation of accelerometer-based vector sensor devices, and its construction is described in the following section. This device will be referred to in this thesis as the *MOD-1* system, to distinguish it another system used in this thesis (described in the subsequent section) with model designation *VHS-100*, manufactured by Ocean Applied Acoustic-Tech, Hangzhou Applied Acoustic Research Institute (HAARI), China.

5.1.1 MOD-1 *(accelerometer based vector sensor)*

The *MOD-1* system is based around the triaxial accelerometer, model number 356A16, manufactured by PCB Piezotronics, Inc. Figure 5.2 shows a cut-away of the triaxial accelerometer, which is a machined aluminum cube with sides roughly 14 mm long. Three unidirectional accelerometers, such as that depicted in Fig. 5.1, are screwed into three

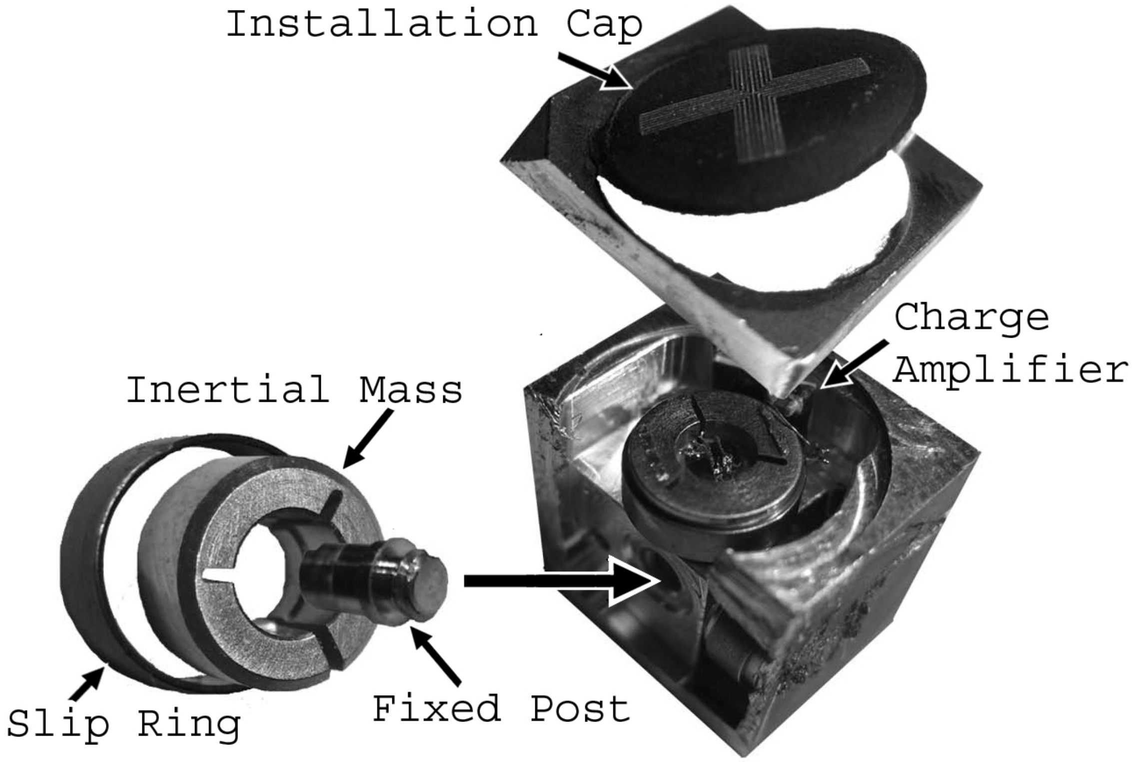

Figure 5.2: Exploded view of the PCB Piezotronics, Inc. 356A16 accelerometer.

Figure 5.3: Neutrally Buoyant Housing of *MOD-1*.

tapped (threaded) holes, orienting the axis of each unidirectional accelerometer along a Cartesian coordinate. In Fig. 5.2, one of the unidirectional accelerometers is shown in the exploded view (the piezoelectric ceramic wafer is not pictured), and another is shown installed in position with its charge amplifier in place. The accelerometer is assembled by pressing the slip-ring over the inertial mass, which compresses the circular mass around the piezoelectric ceramic and fixed rod. The slip-ring "preloads" (compresses) the ceramic wafer which acts a stiff spring in slight compression, connecting the fixed rod to the inertial mass as a mass-spring system with a resonance of $\sim$ 35 kHz. The threaded end of the fixed post, which passes through the center of the ceramic wafer, is screwed into one of the tapped holes. The accelerometers are covered by an aluminum installation cap, and the housing is sealed by metal-film and epoxy.

For operation as an underwater vector sensor, it is essential that the sensor be made neutrally buoyant. The 356A16 accelerometer weighs 7.5 grams and displaces 2.7 grams of water, and to make the accelerometer neutrally buoyant, it can surrounded by a volume of syntactic foam, a closed cell foam that does not compress under high pressures. Zeddies, et al., used this method in their construction of a vector sensor (based on the same accelerometer model) for studies on particle motion sensitivity in fish [24]. Figure 5.3 shows the neutrally buoyant *MOD-1* sensor, which consists of the 356A16 accelerometer embedded in a machined cylindrical block of syntactic foam. The foam is surrounded by a plastic sphere (for durability), and is sealed with a watertight coating.

The block diagram of the *MOD-1* system, shown in Fig. 5.4, includes a signal conditioner, which is required to power the accelerometer charge amplifiers. The accelerometer is connected to a signal conditioner by a 4-conductor cable; three of the conductors carry a constant 2.2 mA current to each of the three charge amplifiers in the sensor, and the fourth conductor attaches to the sensor housing. The output of the circuit carries a balanced signal to the portable recording system, a Roland Edirol R-44.

A balanced signal is used in a noise-cancellation scheme, known as common-mode rejection, which can cancel noise common to both inputs. For example, to cancel radio-interference noise that develops on the sensor cabling, two signals are sent along a set of parallel wires, where one wire carries the original signal and the another wire carries an

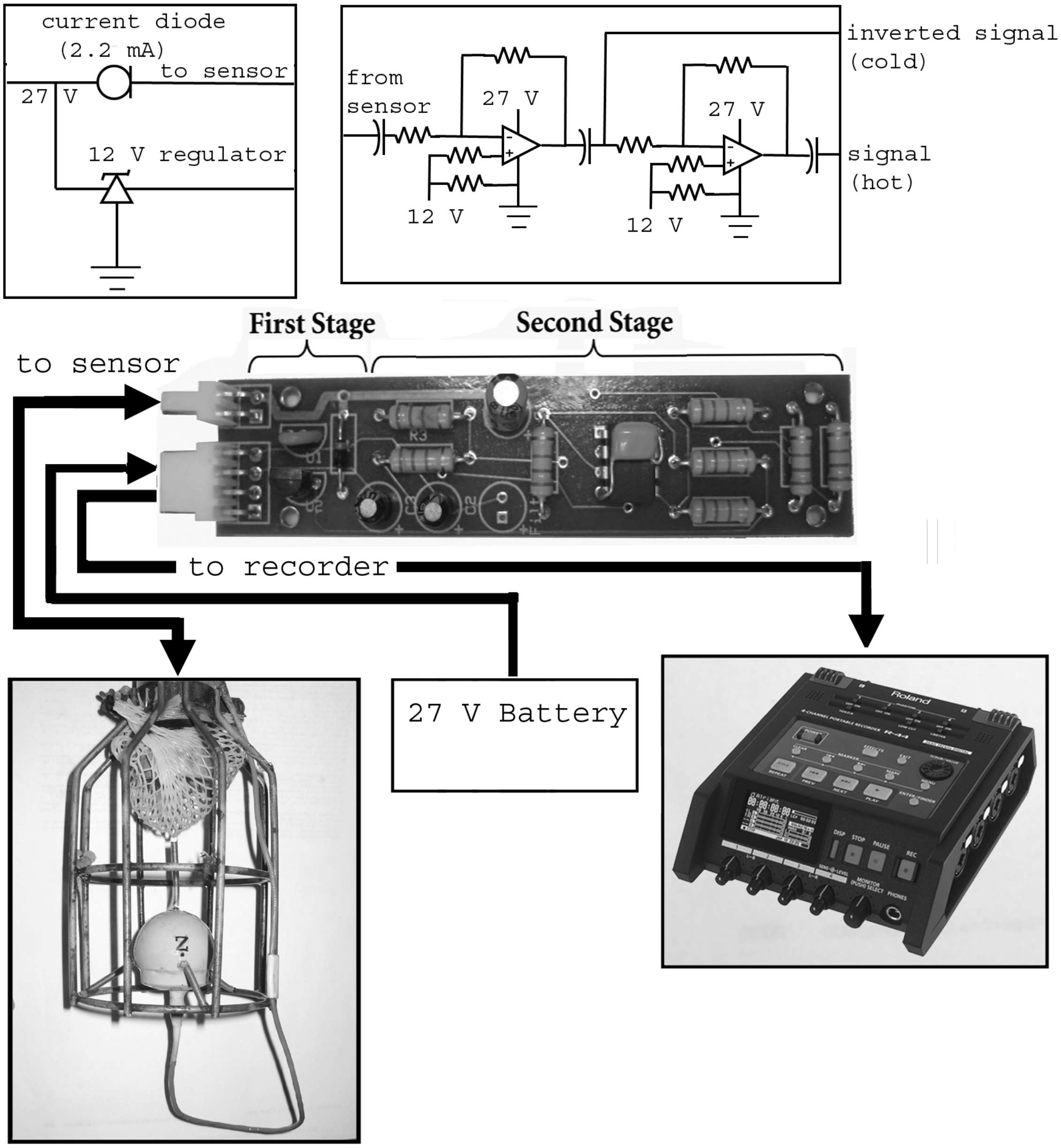

Figure 5.4: Block Diagram of the *MOD-1* vector sensor system

inverted copy. Both the inverted and original signals are thus contaminated by the same interference on the wire, i.e., the common-mode. At the recorder, the internal circuitry subtracts the inverted signal from the original, effectively adding the two original signals together and canceling the common-mode noise. The balanced output typically has three leads, referred to in the audio-industry as hot (original), cold (inverted) and ground, corresponding to the Tip (hot) -Ring (cold) -Sleeve (ground) of a balanced 1/4" TRS audio jack.

When an unbalanced signal from the accelerometer (such as that provided by the output of the PCB Piezotronics, Inc. signal conditioner model 480C02) is fed into the Edirol R-44 recorder, the signal becomes contaminated by internal clock-noise. I subsequently discovered this to be a problem with all unbalanced inputs into the Edirol R-44. The reason the Edirol R-44 recorder introduces clock-noise on the unbalanced input, I believe, is due to the internal balancing circuitry of the recording system. It does not present a problem to balanced signals, as the internal clock-noise, which contaminates both inputs, is removed by the common-mode rejection circuitry. An unbalanced signal does not have a cold signal, and the clock-noise contaminating the original signal is not removed.

With the help of undergraduate research assistant Robbie Burns, I designed and constructed the custom signal conditioner that solved this problem. The circuit, shown in the block diagram in 5.4, provides the necessary current (2.2 mA) to the accelerometer, analog filtering and amplification capabilities, and provides the necessary balanced output signal for the R-44 recorder. The *MOD-1* sensor is also shown in Fig. 5.4 in a wire-cage, suspended by springs to maintain its orientation. Design considerations of vector sensor suspension systems, relating to that built for the *VHS-100*, are discussed next.

5.1.2 VHS-100 *(and suspension frame)*

It is very likely that the commercial (off-the-shelf) vector sensor, the *VHS-100*, contains a triaxial accelerometer similar to the one used in the *MOD-1* system. Regardless of its internal construction, an accelerometer-based vector sensor requires a suspension system to fix the sensor in a known orientation. The *VHS-100* has 6 eyelets, intended to be used in

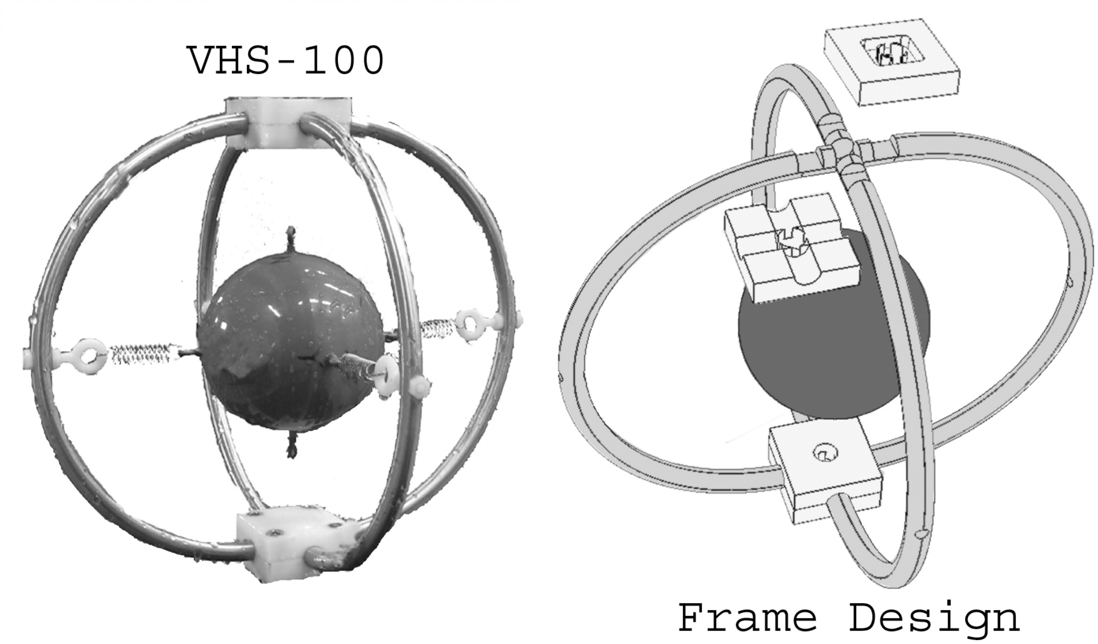

Figure 5.5: *VHS-100* in suspension frame

suspending the sensor in a rigid frame by springs (or rubber bands). The springs act to decouple the sensor from its rigid suspension frame, however the springs introduce a resonant frequency in the system that depends on the spring constant, the number of springs, and the mass of the sensor.

Figure 5.5 shows an image of the *VHS-100* suspended by stainless steel springs in its modular frame, which I designed and machined from Delrin plastic and 1/2 inch stainless steel u-bolts. Springs with a low stiffness establish a resonant frequency around 4 Hz, well below the 20 Hz to 4 kHz frequency response cited in the *VHS-100* specification sheet. No vertical springs are used in the system, as the horizontal springs appeared sufficient to maintain the orientation of the sensor. Laboratory testing confirmed that this suspension method (as well as that including vertical springs) does not affect the response of the *VHS-100* above 1 kHz.

Following $\lambda = 4/D$ as a guideline for the maximum frequency, with D equal to 10 cm, the *VHS-100* has a maximum frequency around 4 kHz. At frequencies greater than 4 kHz, the short wavelengths can excite internal resonances within the sensor housing. These resonances can be linked to the natural frequency of the actual mass spring system of the internal accelerometers, or to resonances within neutrally buoyant housing (epoxy) of the sensor. At frequencies near the natural resonances of the sensor, the system may appear to have an increased sensitivity; however, at these frequencies the relationship between the accelerometer signal and the acoustic particle acceleration is no longer linear.

The *VHS-100* and its suspension system have been integrated into Peter Dahl's Moored Receiving Array (MORAY) system, and were used in the recent Targets and Reverberation Experiment (TREX) held off the coastline of Panama City, FL. Some "quick look" results from TREX are presented at the end of this chapter. However, it is emphasized that the TREX endeavor is not an integral part of this dissertation research. Rather, it represents an experimental data set that will be studied by me in post-doctoral context, together with Peter Dahl and our colleagues.

5.2 Vector sensor laboratory measurements

To test the ability of a vector sensor to detect particle acceleration, it was desirable to create a simple measurement experiment, which could be compared to a theoretical model. The field of a point source close to the air-water interface exhibits a characteristic interference pattern, often referred to as Lloyd's Mirror. It is named after the famous light experiment conducted by Bartholomew Lloyd in 1834, in which observations of the interference patterns of candle light with its reflection from a darkened mirror were used to demonstrate the wave-nature of light [25].

5.2.1 Analytic Model of Laboratory Experiment: Lloyd's Mirror

Treating the surface as a pressure release boundary, a model of the acoustic field can be constructed from a two point source model, similar to that presented in Chapters 3 and 4. A point source located at the source depth represents the direct field. The reflection from the surface is given by a virtual source equidistant from the pressure release surface, but located above the surface. The pressure field in the water is given by,

$$p(x,y,z;t) = \left[\frac{e^{-ikr_1}}{r_1} - \frac{e^{-ikr_2}}{r_2} \right] Ae^{i\omega t}, \tag{5.1}$$

$$\text{where} \quad r_1 = \sqrt{(x-x_0)^2 + (y-y_0)^2 + (z-z_0)^2},$$

$$\text{and} \quad r_2 = \sqrt{(x-x_0)^2 + (y+y_0)^2 + (z+z_0)^2},$$

and where [x,y,z] is the location of a field point in Cartesian coordinates, with the origin at the sea-surface. To take advantage of the azimuthal symmetry, the source position $[x_0, y_0, z_0]$ is set to [0,1,0], signifying a source depth of 1 m. Inclusion of the factor -1 modifying the virtual source term satisfies the pressure release boundary condition of the surface, such that $p(x,0,z) = 0$. The pressure release model of the sea surface is a reasonable approximation at the frequencies (>1000 Hz) and source depth (1 m) used in this experiment. However, this model may be inappropriate when the source depth, z_0, is such that $kz_0 \ll 1$. When $kz_0 \ll 1$, the source can radiate a significant portion of energy across the air-water interface into the air, a phenomenon referred to as transparency [26]. The values of kz_0 considered here are all much greater than 1. The particle velocity can be computed from Euler's equation and Eq. 5.1, and is nearly identical to the velocity vector given in Eqs. 3.29, 3.30 and 3.31.

Lloyd's mirror pattern is reflected clearly in the degree of circularity for a 2000 Hz tone source at a depth of 1 m. Figure 5.6a shows 3 dB contours of the pressure magnitude field (relative to the maximum), upon which the pattern of Θ is shown. Note how the circularity changes sign near destructive interference (lowest pressure magnitude) and constructive interference (highest pressure magnitude). The arrows in Fig. 5.6a show the path (highly exaggerated) that a fluid particle follows over 3/4 of a cycle at 10 representative depths, and at range 3.17 m. These paths are exaggerated by the same factor to preserve their relative magnitudes.

Figure 5.6b shows the depth dependence of both the exact Θ (depicted by o's) from Eq. 4.2 and the approximate $\tilde{\Theta}$ (depicted by x's) from Eq. 4.4. At the receiver depths of 0.6 m and 2.2 m, particle motion (and thus particle velocity) falls on a line oriented with the ridge of pressure magnitude contours indicating constructive interference. A similar straight line path occurs at destructive interference, indicated by the valley of the pressure magnitude

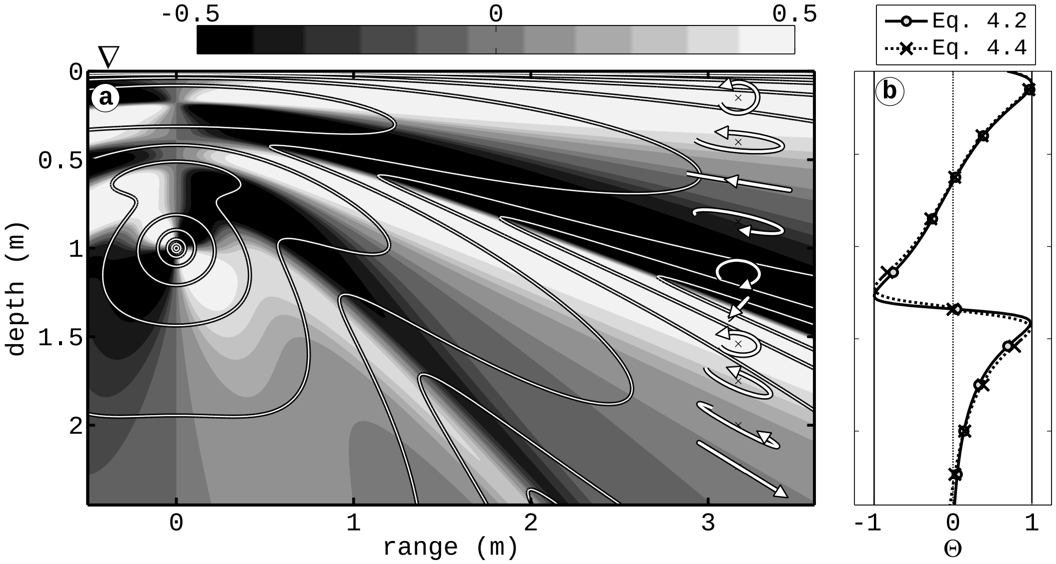

Figure 5.6: (a) Image of the degree of circularity measured in the vertical plane, Θ, due to a 2000-Hz point source 1 m below the air-water interface. The overlaying contours represent equal levels of the pressure magnitude, graded in 3 dB increments. Exaggerated particle paths at a range of 3.2 m and 10 depths are shown, for which Θ ranges from linear ($\Theta = 0$) to circular ($\Theta = \pm 1$). (b) Θ as a function of depth at the range, 3.2 m. The dots correspond to the discrete particle depths depicted in (a).

contours, at 1.3 m. Here the line is oriented in a direction perpendicular to the valley of destructive interference. Particle motion that does not fall on a straight-line is observed on either side of the destructive minimum, e.g., at the receiver depths of 1.4 m and 1.2 m. The motion here is best described as elliptical.

As a reminder, the acoustic particle motion falls between two extremes as parameterized by Θ, being purely circular when $\Theta = \pm 1$ and falling along a straight line when $\Theta = 0$; the sign of Θ signifies the polarization (direction of travel) of the particle motion. Note that above or below a position with zero circularity, the polarization abruptly changes from clockwise to counterclockwise. For example, at depth 1.1 m Θ is negative (clockwise) and at 1.5 m it is positive (counterclockwise).

The polarization of the particle motion can also be described as either prograde or retrograde motion. The direction that particles travel directly above and below the maximum of constructive interference (such as that observed by the contours in Fig 5.6a at depth 0.6

m), when they approach the maximum, is in the same direction as the energy propagation. This type of polarization can be defined as prograde motion. Conversely, the direction that particles travel directly above and below a minimum due to destructive interference (for example at depth 1.3 m), when they approach the minimum, is in the opposite direction as the energy propagation. This type of polarization is retrograde motion. The divergence of the reactive intensity can be used to distinguish prograde (divergent $\nabla \bullet \vec{Q} > 0$) or retrograde (convergent $\nabla \bullet \vec{Q} < 0$) motion. Examples of divergent and convergent reactive intensity in ocean waveguides, and how they relate to dislocations in the field, are discussed in Chapter 7.

The abrupt changes in the sign of Θ predicted by the analytical solution are readily observable in experimental measurements at depths that correspond to destructive interference. The depth spacing and frequency dependence of these abrupt transitions can be used to identify the spatial structure of the interference pattern, which can be used in source-localization algorithms such as that described in [27].

5.2.2 The Lloyd's Mirror Model and Comparison with Experimental Data

The same particle motion features predicted by the analytic solution (Fig. 5.6) have been observed experimentally in measurements I conducted at the University of Washington Applied Physics Laboratory's acoustic test facility (ATF). An approximation to Lloyd's Mirror was generated by an acoustic projector (USRD standard type F37 transducer) positioned at a depth of 1 m, and separated from the receiver by 3.17 m when both were at the same depth. The receiver consists of the *VHS-100* vector sensor and two International Transducer Corp., ITC-1042 hydrophones, attached to the frame directly above and below the *VHS-100* sensor, spaced 15 cm apart. The pressure at the center of the accelerometer is approximated by the average of the two hydrophone signals, and thus the receiver forms a combined sensor.

To recreate Lloyd's Mirror, a 4 ms duration pulse was recorded by the receiver, and the recorded signal was time-gated to include only the first 1 ms of interference, the interference between the direct and surface arrival. After 1 ms, unavoidable reflections from features of the ATF (e.g., pontoons, lake bottom) complicate the interference pattern. Three pulses at center frequencies 2, 3, and 4 kHz, were recorded during this experiment. The frame was attached to a vertical profiler that moved the sensor in 10 cm depth increments. At each depth increment, Θ is calculated by Eq. 4.2, and $\tilde{\Theta}$ by Eq. 4.4.

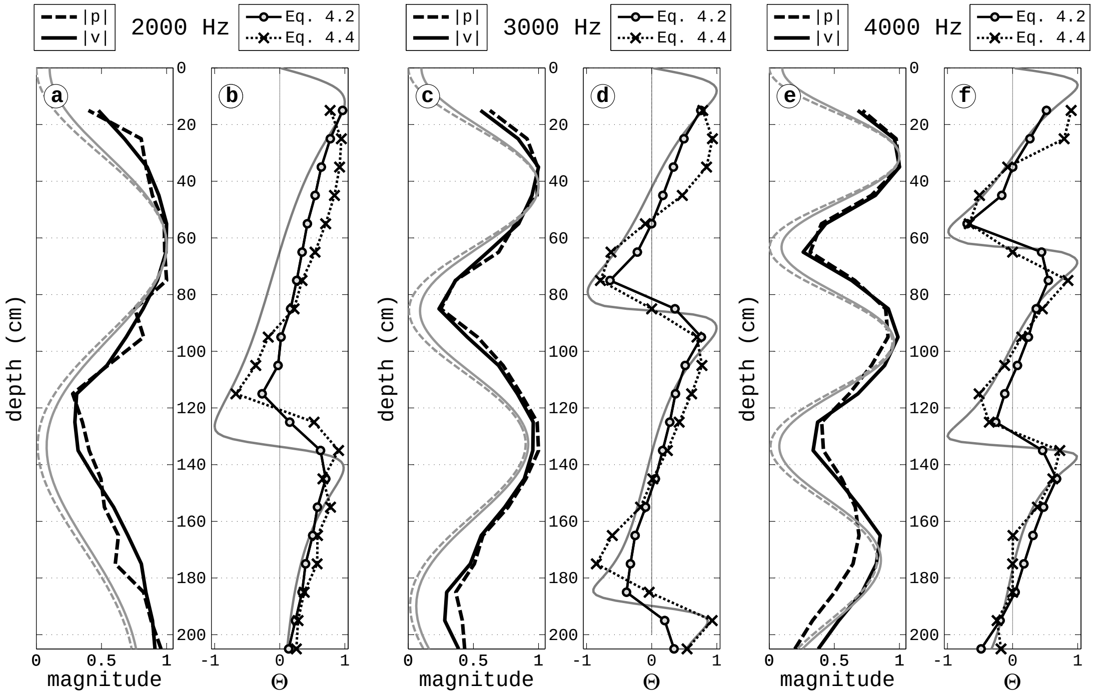

Figure 5.7: (a) Experimental measurements of pressure magnitude $|p|$ (solid black) and particle velocity magnitude $|v|$ (dashed black) versus depth at 2000 Hz are along with the analytic solution of $|p|$ (solid gray) and particle velocity magnitude $|v|$ (dashed gray). Each profile is normalized by its maximum value. (b) Experimental measurements of the exact Θ (circle's) and the approximate $\tilde{\Theta}$ (x's) computed from the vertical component of intensity are plotted over the analytic model of Θ (gray). Results are repeated in (c) and (d) at 3000 Hz, and in (e) and (f) at 4000 Hz.

Figures 5.7a, 5.7c and 5.7e show the experimentally measured magnitude of the pressure (solid black) and particle velocity (dashed black) plotted relative to their maximum recorded level at 2, 3, and 4 kHz, respectively. This data exhibits a very similar depth dependence to the analytic solution for the pressure (solid gray) and particle velocity (dashed gray). Note that the experimental data is constrained by the noise floor and does not have the dynamic range of the analytic solution. Nevertheless, the depths at which maxima or minima of the field occur coincide with the analytic solution.

Figures 5.7b, 5.7d and 5.7f show the measured exact Θ (o's) and approximate $\tilde{\Theta}$ (x's) for 2, 3, and 4 kHz, respectively. These measurements agree reasonably well with the analytic model of Θ (gray), exhibiting either a slowly changing circularity though maxima in the field, or, an abrupt change in sign at the destructive nodes. The depths of these features depend on the frequency of the signal, as well as the depth and range of the source. The zero-crossings of the data and analytical solution do not align precisely, a feature most likely due to the finite dimensions of the sensor ($\sim$10 cm). Aside from this limitation, the character of the zero-crossings at a particular depth (gradual or sharp) is in agreement with the model. Similarly, the number of zero-crossings measured at a particular frequency is accurately predicted by the analytical model. As a point to emphasize, even though estimates of Θ based on its exact and approximate formulation show different magnitudes at each depth, the sign of the two quantities are identical.

The distinct advantage of the Θ description over the pressure or particle velocity magnitude, is the ability to distinguish spatial properties of pressure maxima or minima using one measurement point. For example, on either side of a maximum or minimum, the pressure field will have the same magnitude while the value of Θ will change sign. Additionally, since Θ is non-dimensional, an analysis based on Θ is not sensitive to source level fluctuations. This applies equally to Θ derived completely from the particle velocity (Eq. 4.1) or intensity measurements (Eq. 4.2).

5.2.3 Vector Sensor Comparison: VHS-100 *vs.* MOD-1

Another Lloyd's Mirror experiment was performed at the ATF to compare the two vector sensors, the *VHS-100* and the *MOD-1.* This experiment used an ITC-1007 sound source at a depth of 1 m, separated from receiver by 1.57 m when both were at the same depth. Note that this geometry differs from the experiment in Fig. 5.7. The experiment was repeated at 6 frequencies, ranging from 1 to 6 kHz in 1 kHz steps.

Figure 5.8 compares measurements made by the *VHS-100* (x's) and the *MOD-1* (o's)

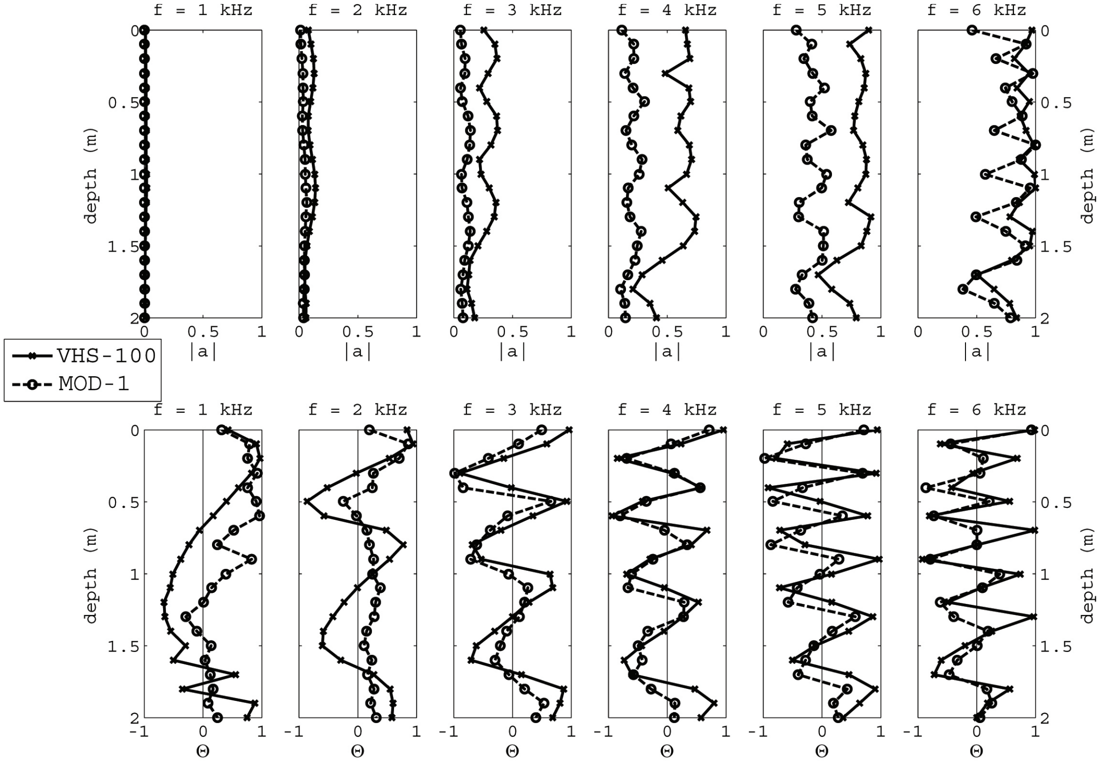

Figure 5.8: Experimental measurements at the ATF of particle velocity magnitude $|v|$ by the *VHS-100* (solid) and the *MOD-1* (dashed) vector sensor for a source located 1.57 m from the sensors, depth 1 m below the surface. (top) Magnitude of particle acceleration normalized by the maximum value over all the frequencies. (bottom) Corresponding value of Θ.

vector sensors. The upper plots show the magnitude of particle acceleration at the six frequencies, the magnitude of each sensor was normalized by its maximum recorded value at 6 kHz. Although the source level at each frequency is not necessarily the same, the plots do show the relative sensitivity of two sensors at each frequency. It appears that the *MOD-1*, when compared to the *VHS-100*, is more sensitive at higher frequencies than lower frequencies. Likewise, the *VHS-100* has a relatively flat response between 4-6 kHz, when compared to the *MOD-1*. Noting the physical differences in the two sensors, the diameter, D, of the *VHS-100* is four times that of the *MOD-1*. Following $D = \lambda/4$, the physical size of the *VHS-100* (D=10 cm) sets the upper frequency limit to $\sim$4 kHz. A calibration experiment, which used a direct signal with a known-pressure level (and thus known velocity), confirmed that the voltage response increases by a factor of ω (as expected from the time-derivative of velocity) up until 4 kHz. At higher frequencies, the linear relationship between voltage and acceleration starts to break down.

The lower plots of Fig. 5.8 compare the measured Θ as a function of depth. No pressure hydrophones were used in this experiment, and the acceleration channels of the sensors were time-integrated to compute the particle velocity and $\vec{\Theta}$ from Eq. 4.1. The value of Θ was computed at the time of the surface arrival following the same procedure used to create Fig. 5.7. The two sensors capture the same zero-crossings of Θ at nearly all of the frequencies. At the lowest frequency, the ITC-1007 source was unable to produce the desired signal level, however the *VHS-100* did manage to capture some of these features. In general, the more massive *VHS-100* appears more sensitive to the extreme Θ values, although note that its suspension frame was of higher quality construction and the natural frequency induced by the springs was lower than that of the *MOD-1*.

5.3 Vector sensor field measurements

Finally, let us take a brief look at the *VHS-100* sensor as it operates in sea water field conditions. As mentioned earlier, the *VHS-100* and frame were integrated into the Moored Receiving Array (MORAY) system, a project undertaken by Peter Dahl and the Applied Physics Laboratorys Ocean Engineering Department, under an ONR DURIP grant. The MORAY was recently reconfigured as a experimental benthic tower, and was used in the ONR funded experiment known as TREX (Targets and Reverberation EXperiment), which was held off the coastline of Panama City, Florida in April and May of 2013.

The MORAY tower, which was deployed on the sea-floor as shown in Fig. 5.9, consists of twelve ITC-1042 hydrophones and the *VHS-100* vector sensor. One hydrophone was placed within its suspension frame of the *VHS-100* vector sensor, forming a combined sensor, and the others were arranged in a 7-element vertical line array (VLA), and a 4-element horizontal line array (HLA). In this section we will only examine a few measurements from the combined sensor, for which this was the first real at-sea test. Note that the extensive dataset collected during TREX will be the subject of vigorous data analysis in future studies, as discussed in Chapter 8. The measurements presented here, in Figs. 5.11 and 5.12, give

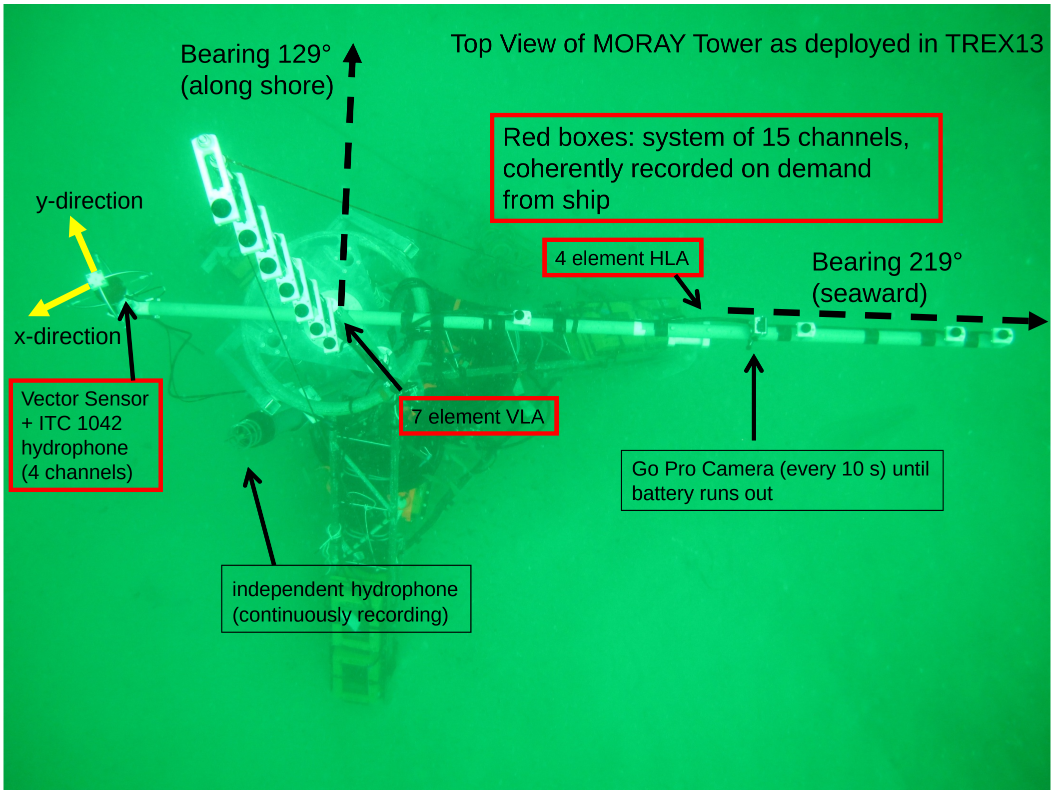

Figure 5.9: Dive photograph of MORAY tower with its key elements identified. The neutrally buoyant *VHS-100* is shown on the left, suspended within its rigid frame.

a sense of the quality of this kind of vector data in shallow water (depth 18 m). In doing so, let us exploit an “accident” that occurred during the diver-assisted deployment of the tower.

The HLA was aligned pointing seaward, along the bearing 219°. It was planned that one axis of the *VHS-100* (y-axis) was to be precisely aligned with the HLA. However, towards the end of deployment procedure (lasting about an hour) a diver’s knee inadvertently came into contact with the *VHS-100* frame causing it rotate an estimated $\sim 35°$. This unplanned rotation was apparent upon inspection of the deployment photos made by the divers (who were at the time unaware of the extended frame contact), such as the one shown in Fig.

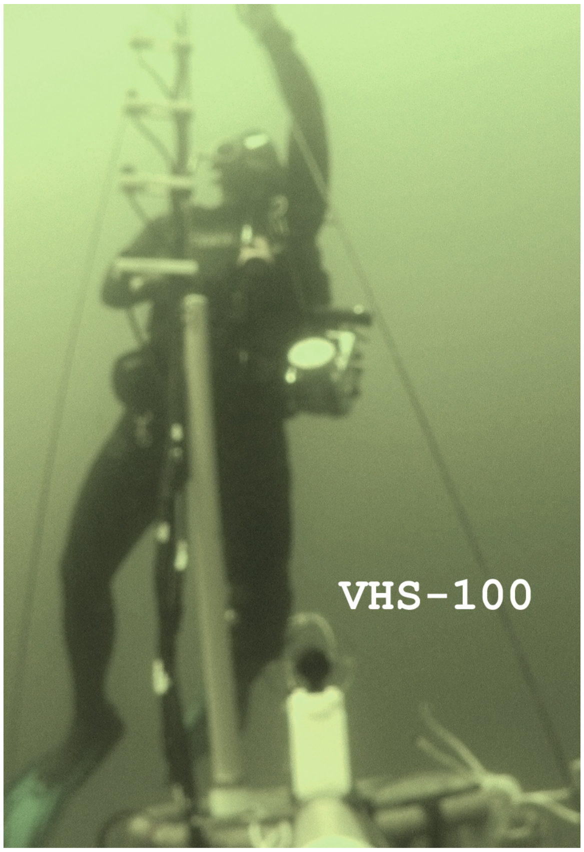

Figure 5.10: Image of the deployment of the *VHS-100* and orientation change due to diver operations captured by a 10 second time-lapse GoPro camera.

5.9. A GoPro camera mounted on the tower, retrieved when the tower was recovered some days later, also documented the contact event and is shown in Fig. 5.10. Furthermore, this camera documented that no additional rotation of the vector sensor occurred over the duration of its deployment.

The rotation of the vector sensor was confirmed acoustically, using data that was sent back to the research vessel via telemetry. As part of the experiment, an ITC 2010X sound source was lowered to a depth of 12 m from the stern of the R/V *Smith*, and transmitted several pulse types, some being a 2 kHz continous wave (CW) tone of duration 100 ms. The *VHS-100* acceleration measurements at range 200 m at bearing 129°, and the measurements at the same range but at bearing 219°, were used to compute the particle velocity, and

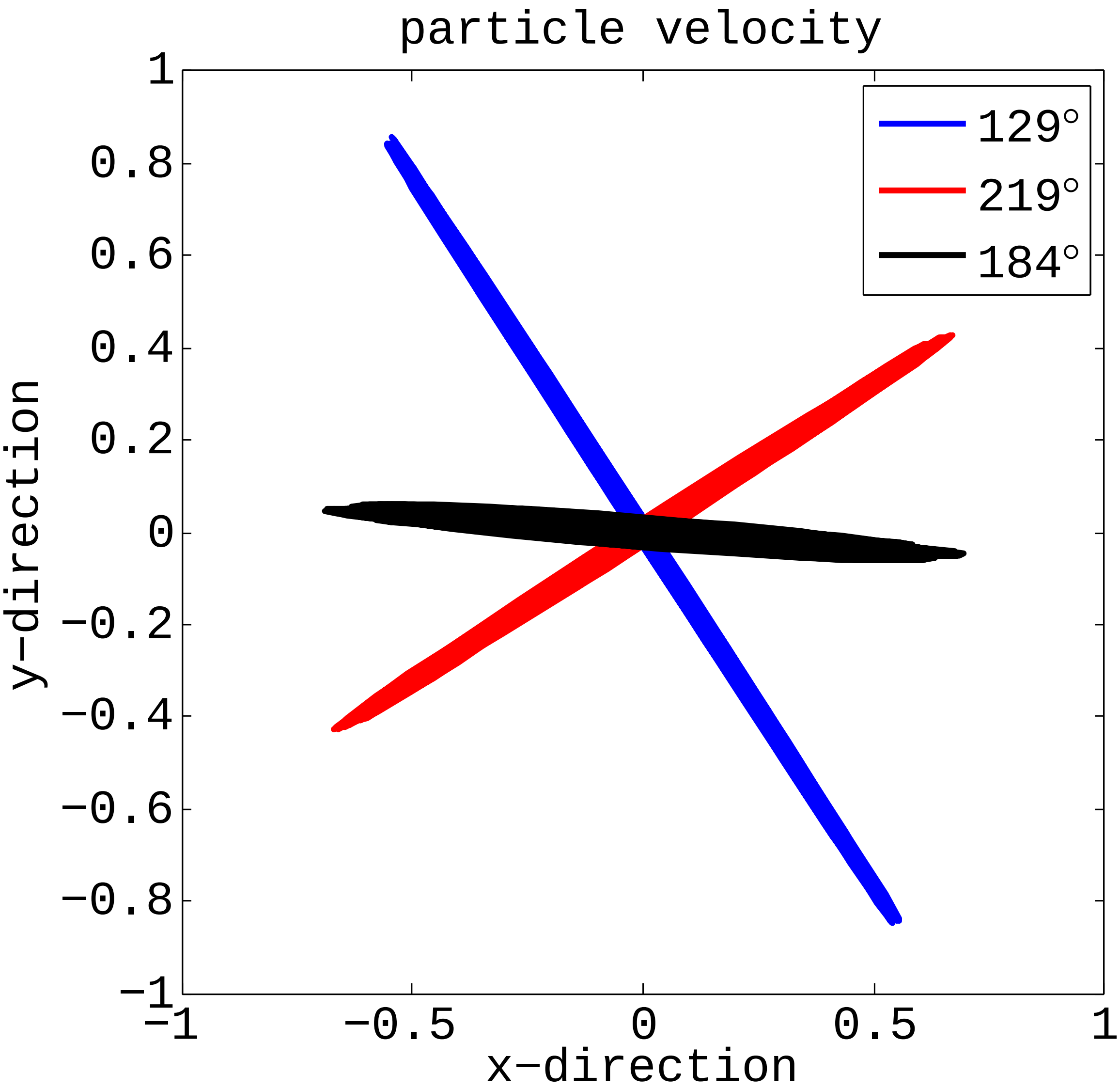

Figure 5.11: Measurements of the acoustic particle motion by the *VHS-100* in the horizontal (x-y) plane, of a 2 kHz tone measured at three source-receiver bearings. The particle motion (and velocity) oscillates between positive and negative. Notice that the y-component of the measurement at the source bearing 184° is nearly zero.

particle displacement. Figure 5.11 shows the measured particle motion (displacement), computed for the 129° measurements (blue) and 219° measurements (red). The particle motion follows a nearly straight-line path over the first 40 ms of the arrival, and the signals from the two bearings are nicely perpendicular (all paths are scaled by the same constant). From these measurements, an estimate of the rotation was further refined to be 35° from its intended orientation. This was subsequently confirmed by repositioning the R/V *Smith* at range 200 m and bearing 184°, which produced the black line in Fig. 5.11. In this case, the y-component of horizontal particle velocity is nearly zero, confirming the estimated rotation.

The velocity data has an ambiguity in the source direction, given that it travels back and forth along the line shown in Fig. 5.11. This ambiguity can be resolved by measurement of the active intensity vector, which is made possible by the pressure measurement from the hydrophone placed within the frame of the *VHS-100*. Figure 5.12 shows the horizontal components of active intensity, the measurements at each bearing are scaled by the same constant. The active intensity points unambiguously away from the source, and thus demonstrates that a combined sensor can resolve uncertainty in source bearing. Additionally, the combined sensor can obtain an vertical arrival angle, allowing for an estimate of the three-dimensional source bearing. Note that in shallow water, as will be shown in the following two chapters, the vertical bearing angle often corresponds to properties of the waveguide, and not the vertical elevation angle of the source.

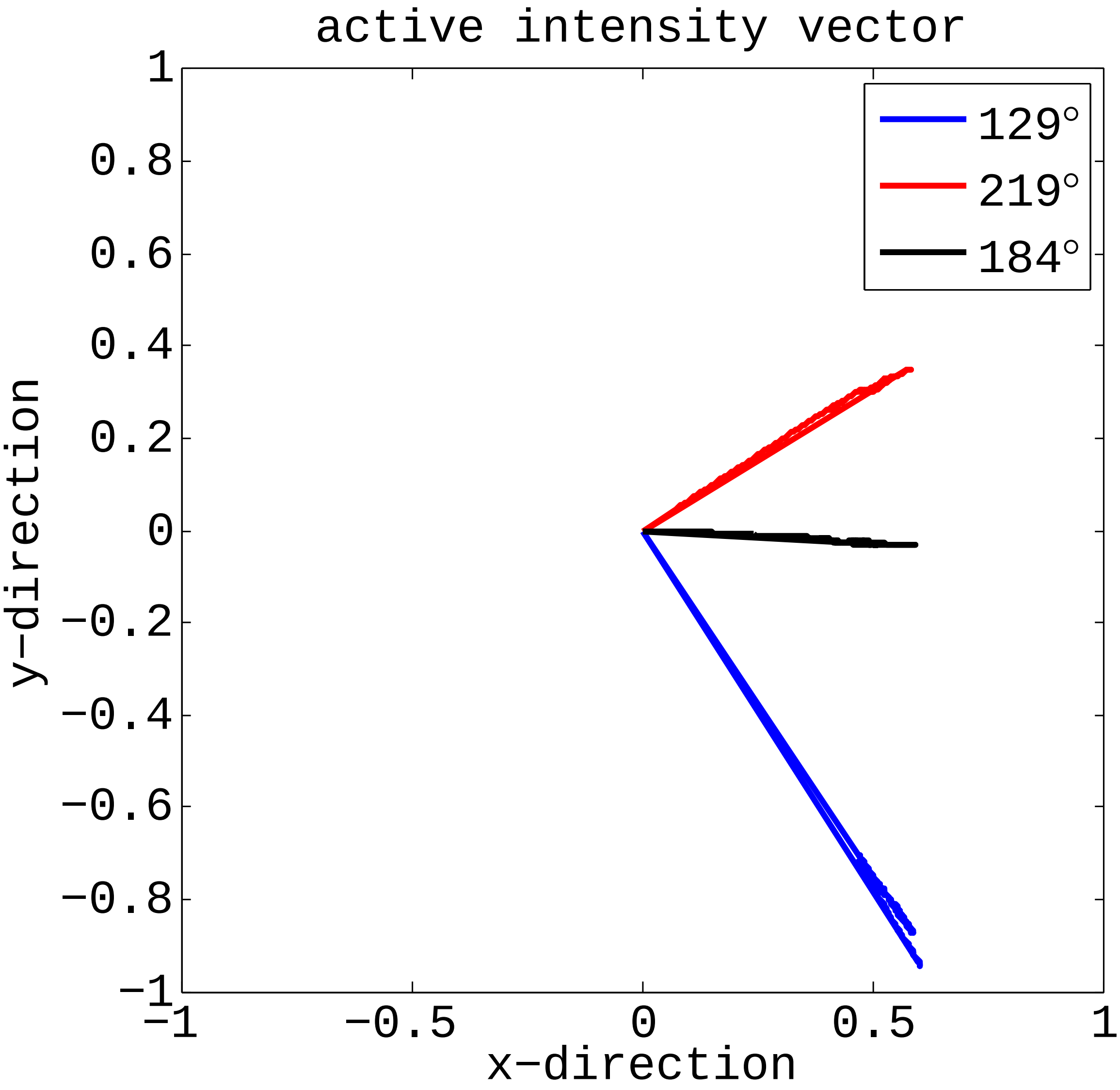

Figure 5.12: The active intensity envelope in the horizontal plane corresponding to the particle velocity estimates shown in Fig. 5.11. The sign corresponds to the direction of propagating intensity, away from the source bearing.

Chapter 6

EFFECT OF LAYERED SEDIMENTS ON VECTOR PROPERTIES

This chapter consists of results from an ocean experiment, which are presented in a paper accepted by the Journal of the Acoustical Society of America for publication in July, 2013 [8]. Experimental measurements of the vertical intensity in the ocean are interpreted in terms of the vector properties described in the previous chapters. Observations of the spatial dependence of these vector properties led to the development of the approximate degree of circularity in Eq. 4.4, which was subsequently used to determine the properties of the sea bed.

These measurements were made by my advisor, Peter Dahl, in 2006, in an experiment conducted off of the New Jersey Coast in waters 80 m deep, using a different configuration of the MORAY system that predates the integration of the vector sensor, described in the last chapter. The pressure measurements collected on the vertical line array of the MORAY were used to compute the vertical intensity by finite-difference methods.

6.1 Experimental description

The data used in this discussion was recorded on the moored vertical line array (MORAY), centered at 39.0245° N, 73.0377° W. An ITC-2010X source, positioned within 5 m of the bottom, was towed from the stern of the R/V *Knorr*. The ship traveled at a speed of 0.1 m/s, starting at range 50 m from the MORAY and proceeding to range 300 m, along four different source-receiver bearings, while the source transmitted a sequence of three pulses every 12 s; a 2-16kHz FM sweep, a 2 ms continuous wave (CW), followed by a 3 ms CW, each CW with center frequency 1 kHz.

The complex vertical intensity is approximated by the hydrophone pair (separation 20 cm) centered at the depth of 49 m. The vertical intensity is used to compute the approximate degree of circularity ($\tilde{\Theta}$) for the two, 1 kHz CW pulses (use of both CW pulses provides

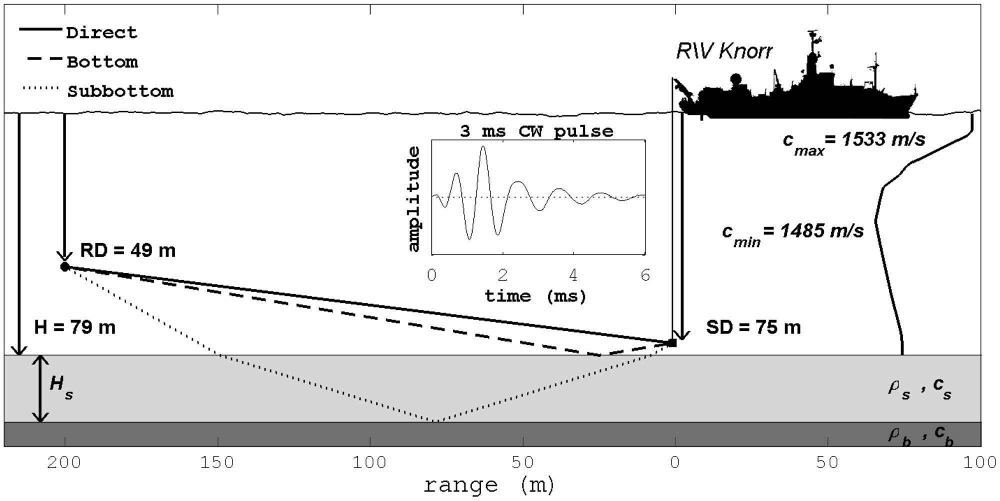

Figure 6.1: The experimental geometry and the first three arrivals. The direct (solid), bottom (dashed), and sub-bottom (dotted) path from the towed source (depth 75 m) to receiving array (depth 49 m) are shown for a source range of 200 m. The sound speed profile in the water column varies from a maximum of 1533 m/s at the surface to a minimum 1485 m/s at the thermocline at 20 m depth, the sound speed at the water-sediment interface is 1499 m/s.

more range sampling). The range dependence is given explicitly by GPS coordinates of the source and receiver, which recorded for each transmission.

Figure 6.1 shows the geometry of the experiment, including the sound speed profile depicted on the right side. The inset figure is a rendition of the actual 3-ms pulse transmitted, derived from calibration measurements made shortly before these measurements but at range 50 m, with the source at mid-depth to allow for a clean, direct arrival. The ray-paths of the first three arrivals are shown for a source-receiver range of 200 m. Although the amplitude of the sub-bottom reflection (dotted line) is substantially weaker than the direct (solid line) and bottom (dashed line) arrivals, the interference caused by this arrival can be observed in the experimental data. The arrival times of these first three paths, extracted from the matched-filtered arrivals of the FM-sweep pulse, show that the direct, bottom and sub-bottom path arrive simultaneously at a range of 200 m. (This range estimate is later used in Section 6.4 for geo-acoustic inversion.) In addition to the matched-filtered data, the measured Θ exhibits a range-dependence that corresponds to the arrival angle of the sub-bottom path.

6.2 Experimental measurements of $\tilde{\Theta}$ at the experimental site

Figure 6.2 shows the experimental data collected along one of the range tracks, with data time-aligned to the direct arrival. The experimental data is plotted next to simulated data to help identify features due to the interference in the noisy experimental data. The interference features are hard to distinguish in the pressure data $|p|^2$ (plotted in a relative dB scale to the maximal value), although in the simulated data, the destructive interference can be seen by the dark dots indicating destructive interference within the arrival. The experimental measurements of the vertical active intensity, which is predominately negative, indicate an arrival from below the receivers. A few white dots are visible, indicating intensity from above, which are caused by the destructive interference of direct and sub-bottom paths. The interference is most clearly visible in the vertical reactive intensity, and following the intensity formulation of circularity (Eq. 4.2), corresponds to a change in polarization of the Θ.

Figure 6.3(a) shows $\tilde{\Theta}$ as a function of range computed from the pressure and vertical particle velocity. The value of $\tilde{\Theta}$ reported for each CW pulse corresponds to the value at the time of the direct arrival. Results from the individual ship tracks along the bearings 120°, 210°, and 300° (thin black lines) show a similar feature between 175-230 m that remains through averaging (thick gray line).

As observed in the experimental data, interference between the first three arrivals causes distinct oscillations in Θ as a function of range. The Θ range dependence can be described by a wavelength, λ_Θ, defined as the characteristic range between peaks of similar signed values of Θ. The experimental data yields $\lambda_\Theta \simeq 16$ m.

Although the experimentally measured magnitude of Θ appear to be close to zero, the reported magnitudes are stable over the 2-3 ms duration of the pulse. The magnitude of the circularity is related to the relative level of the interfering arrivals; larger values of Θ (closer to ± 1) will occur when the interfering wavefronts are of equal magnitude. The amplitude

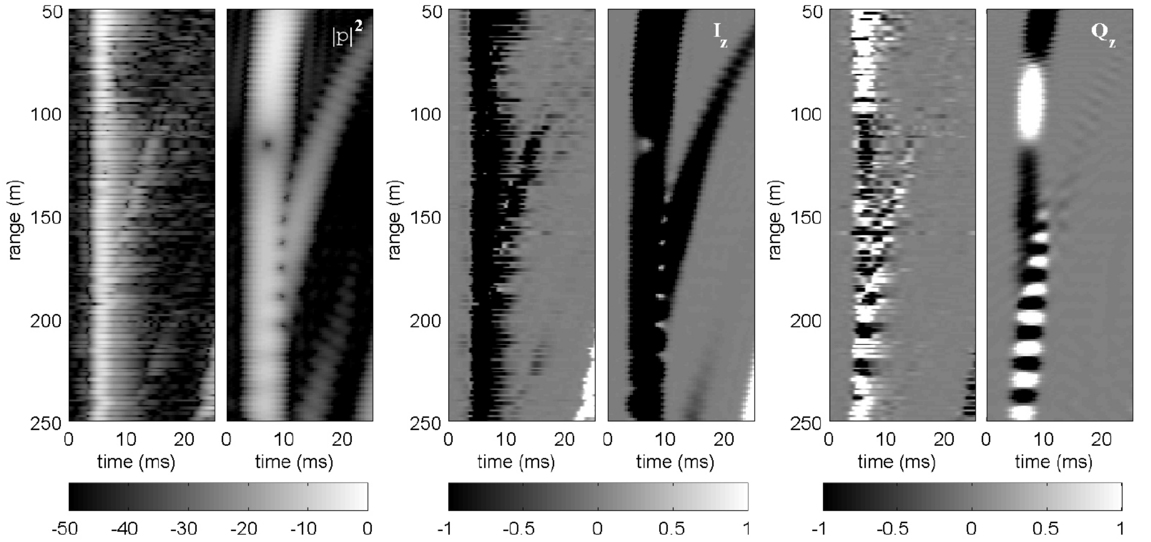

Figure 6.2: Experimental measurements at 50 m depth of (a) pressure magnitude squared divided by $\rho_0 c$, (b) vertical active intensity and (c) reactive intensity (all normalized by their respective maximum recorded value) are plotted next to their respective simulated data.

of the sub-bottom arrival is at least an order of magnitude less than direct arrival [29], as this path is subject to attenuation of the sediment and reflection/transmission coefficients of the interfaces. Regardless of the relative levels, the range dependence of the polarization of Θ, from which we determine λ_Θ, is not dependent on the relative magnitude of the two arrivals. Furthermore, the levels reported experimentally are in accordance with the levels predicted by numerical simulations of the pulse as discussed next.

6.3 Simulation of Θ for the experimental site

Synthetic time series of the pressure and particle velocity, computed from numerical simulations of the acoustic pressure by the RAM-PE [30] parabolic equation code which is discussed further in Chapter 7, are used for comparison with experimental data. The particle velocity is computed by the finite difference of the pressure simulations, and a Fourier synthesis of these numerical simulations, spanning the frequency band of the experimental pulse waveform shown in the inset of Fig. 6.1, are used to construct the time-series. The

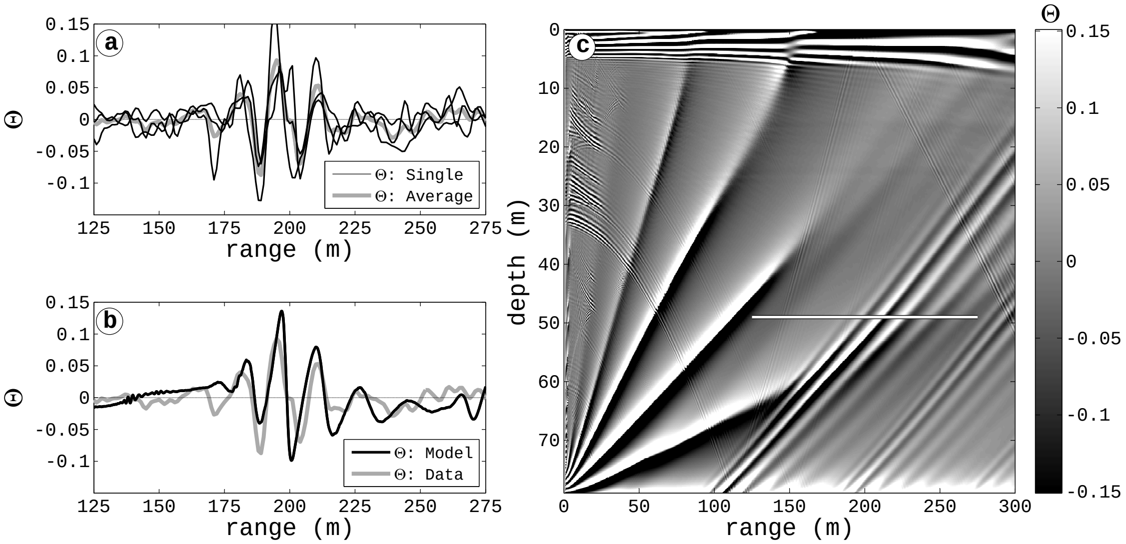

Figure 6.3: (a) Plot of experimentally measured $\tilde{\Theta}$ over three tracks (thin black) and their average (thick gray). (b) Plot of the corresponding simulated value of Θ (thick black) and the averaged experimentally measured $\tilde{\Theta}$ (thick gray). (c) Image of simulated value of Θ occurring during the direct path arrival as a function of range and depth. See text for bottom model. The range corresponding to the experimental data is shown by white horizontal line at depth 49 m.

simulated pressure and particle velocity time-series then used to compute the time dependent $\vec{I_c}$ and Θ at each range and depth point. Fig. 6.3(b) shows the average experimentally measured $\tilde{\Theta}$ (gray line) and the simulated Θ (black-line), corresponding to the value at the time of the direct arrival. The image of Θ in Fig. 6.3(c) corresponds to the value of the Θ at the time of the direct arrival. The range and depth of the experimental and simulated data shown in Fig. 6.3(b) correspond to the white horizontal line in Fig. 6.3(c).

Observe the range dependence of Θ for the experiential receiver depth of 49 m in Fig. 6.3(c). At a range of 175 m, the range dependence of Θ undergoes a transition due to additional interference from a sub-bottom reflected wave, which begins to interfere with the direct and bottom arrivals. The experimental pulse determines this range; for example, were it to have been longer in time (or processing bandwidth decreased), the point at which direct and sub-bottom arrivals begin to interfere would be less than 175 m. The range indicating the onset of sub-bottom/direct interference also depends on properties of the sediment through which the sub-bottom arrival propagates. This range of interference is exploited for geo-acoustic inversion in Sec. 6.4.

At ranges less than 175 m, only the direct and bottom paths are interfering. This depth and range dependence of Θ shares some properties with Lloyd's Mirror discussed in Chapter 5. If there were layering structure in the sea-bed (and thus no sub-bottom reflection), the pattern would extend until the range where simultaneous surface arrival would begin to interfere. For example, interference due to the surface path can be seen in Fig. 6.3 at depths less than 5 m.

At ranges greater than 175 m, a simultaneous sub-bottom arrival establishes an additional interference with the direct/bottom arrivals, characterized by λ_Θ. The value of λ_Θ relates directly to the propagation angle of the sub-bottom path. As the propagation angles of the sub-bottom arrivals are close to the critical angle of the water/sediment interface, the value of λ_Θ is nearly a constant.

The value of λ_Θ can also be computed by ray theory. To include the time-dependent nature of the pulses in ray theory, the arrival time of the direct, bottom and sub-bottom arrivals are explicitly calculated. Then, the field is computed during the direct arrival time, where the bottom and sub-bottom arrivals are included in the sum if their arrival times are within a pulse duration of the direct arrival. Since the source is near the bottom, both the direct and bottom path arrive nearly simultaneously.

Fig 6.4 shows Θ computed using the plane wave reflection coefficient and the spherical wave reflection coefficient. The effect of the spherical wave reflection coefficient, which depends on the frequency and the proximity of the source to the boundary, becomes significant when the source is close relative to a wavelength. The spherical-wave reflection coefficient can be computed as a function of indicent angle by numerical integration of the plane-wave reflection coefficient over complex angles, evaluated near the incident (reflected) angle. The complex angles are an important contribution to the integral, and correspond to an evanescent wave excited in the lower media, which then propagates into the water. The range of angles used in the numerical integration is adjusted for each incident angle, such that all of the excited propagated waves are included in the integral.

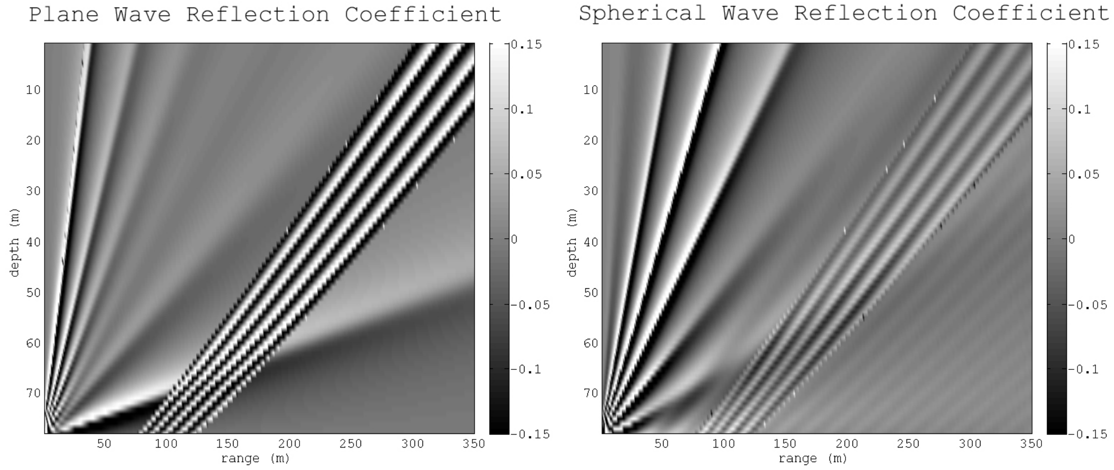
Plane Wave Reflection Coefficient

Spherical Wave Reflection Coefficient

Figure 6.4: Θ computed from a ray model using the plane wave (left) and spherical wave (right) reflection coefficient for a layered sediment model.

These results are in agreement with parabolic equation simulations. Note that the spherical wave reflection coefficient model and the numerical model have the same spatial dependence of Θ relating to the direct and bottom arrivals, as can be seen by comparison of Figs. 6.3 and 6.4. As both the plane wave and spherical wave model show, the interference due to the sub-bottom path maintains a characteristic wavelength, λ_Θ, regardless of the reflection coefficient. As the plane-wave reflection coefficient is able to recreate this pattern (and does not require time for numerical integration), the simpler plane wave model will be used for modeling the parameter dependence of λ_Θ.

The simulations of Θ in Figs. 6.3 and 6.4 all use a bottom model consisting of 2 layers: the upper layer properties are c_s=1614 m/s, ρ_s = 2000 kg/m^3, H_s=16 m, the lower R-reflector half-space properties are c_b=1740 m/s, ρ_b = 2200 kg/m^3 (see Fig. 6.1 for variable definitions). Attenuation in the sediment layer was set to 0.05 dB/m/kHz, and a value of 0.3 dB/m/kHz was used for the absorbing half-space [29]. These parameters were found to be the best-fit parameters for the two layer bottom model, and are compared to other experimental studies in [7]. The effect of the sound-speed and layer thickness on circularity measures, and the sensitivity to these parameters are discussed next.

6.4 Geoacoustic Inversion

The bottom properties effect the vector properties of the field due to the additional interference from an arrival from a sub-bottom layer of the sea-floor. The arrival angle of this sub-bottom reflected wave depends on the properties of the upper layer through which the wave propagates. The arrival angle of the sub-bottom arrival establishes the characteristic range scale of oscillations in the circularity,λ_Θ, which are equally reflected in the active intensity vorticity and the reactive intensity divergence.

A simple relationship can be used to describe λ_Θ by two propagation angles, which is used to discuss the sensitivity of λ_Θ to the bottom parameters in terms of the Cramer Rao Lower Bound (CRLB) framework. For a pulse with acoustic wavelength, this relationship is,

$$\lambda_\Theta = \frac{\lambda}{\cos\phi_d - \cos\phi_s}, \tag{6.1}$$

where ϕ_d and ϕ_s are the propagation angles of the direct path and sub-bottom path with respect to the horizontal, respectively.

For a given bottom parameterization, ray theory can be used to compute the arrival angles, where the propagation angle of the direct path is readily determined by the source-receiver geometry and the propagation angle of sub-bottom path is constrained by Snell's law. This constraint can be used to construct the geometry of the sub-bottom path which is sensitive to two parameters, the layer thickness (H_s) and the layer soundspeed (c_s); the density and attenuation of the layer do not effect the propagation angles. For this analysis, all the paths considered remain below the thermocline (see Fig. 6.1) and simple geometrical-methods are adequate.

The contours of Fig. 6.5(a) show the values of λ_Θ for various candidate models of the overlaying layer $[c_s, H_s]$, for which the sediment below this layer is considered a halfspace with sound speed 1740 m/s. A particular value of λ_Θ is satisfied by a set of $[c_s, H_s]$ parameterizations; additional information is needed to infer a best fit to the parameter space.

6.4.1 Geo-acoustic inversion results based on λ_Θ

Two methods can be used to reduce the parameter space and arrive at a best-fit estimate. One method includes additional data from chirp sonar surveys of the experimental area [31]. The other method utilizes the arrival time information from the experimental pulses.

The chirp sonar method incorporates the measured two-way travel time (TWT) between the water-sediment interface and the bottom of the layer. The TWT follows a simple relationship, TWT $= 2H_s/c_s$; the measured TWT$\simeq$ 26 ms through the upper layer throughout the experimental area. Modeling the overlaying layer as with a constant density and sound speed, the thick dashed line in Fig. 6.5(b) identifies which pairs of $[c_s, H_s]$ values consistent with a TWT$\simeq$ 26 ms. Similarly, the curved solid thick identifies which pairs of $[c_s, H_s]$ consistent with a value of $\lambda_\Theta = 16$ m. The intersection of the TWT parameterization and λ_Θ gives a parameter estimate of a $c_s = 1610$ m/s, $H_s = 21$ m.

The other method uses only the pressure measurements to narrow the parameter space as follows. For a given bottom parameterization, the arrival-times calculated from ray theory can be written in terms of the range where simultaneous arrivals occur. As the measure of circularity depends on interference of the direct and sub-bottom path; the presence of Θ oscillating in sign (along with a characteristic λ_Θ) at a particular range indicates overlapping arrival times. The thin contour lines in Fig 6.5(b) show the range, for the experimental aquistion-geometery and various bottom parameterizations, where the sub-bottom and direct path arrival times are identical.

The experimental measurements of Θ in Fig. 6.3(a) show oscillations occurring at ranges of 175 m to 220 m. This spread in range (both closer and farther away) is due to the duration of the pulse (∼3 ms). The range where there arrivals occur simultaneously is further narrowed by the aforementioned matched-filtered data, which shows simultaneous arrival of the direct and sub-bottom path at range 200 m. Note that the arrival-time model and λ_Θ model have an inherently different parameter dependence, and their intersection establishes a best fit model, $c_s = 1614$ m/s, $H_s = 16$ m. (This best fit estimate is used in the simulations in Fig. 6.3.) The filled in area in 6.5(b) is the union of the three parameter dependencies: λ_Θ, TWT, and arrival-time (two are required for a best-fit estimate).

6.4.2 CRLB of parameter estimates based on Θ

The uncertainty of the bottom parameters based on a value of λ_Θ can be derived from the Fisher information matrix,

$$\mathbf{F} = \frac{1}{\sigma^2_{\lambda_\Theta}} \begin{bmatrix} \frac{\partial^2 \lambda_\Theta}{\partial c_s^2} & \frac{\partial^2 \lambda_\Theta}{\partial c_s \partial H_s} \\ \frac{\partial^2 \lambda_\Theta}{\partial H_s \partial c_s} & \frac{\partial^2 \lambda_\Theta}{\partial H_s^2} \end{bmatrix}, \tag{6.2}$$

where the matrix elements are the partial derivatives of the λ_Θ, with respect to the parameters, and σ_{λ_Θ} is the uncertainty in the estimate of λ_Θ. The diagonal elements of the inverse, $\mathbf{F}^{-1}$, are the CRLB estimates for the parameters under study. If off-diagonal elements of $\mathbf{F}^{-1}$ are non-zero, there is evidently coupling between parameter estimates.

The measurement of λ_Θ from two vertically spaced hydrophones has an inherent degree of uncertainty, σ_{λ_Θ}, which is affected by the signal to noise ratio (SNR). An analysis of simulated data with additive Gaussian white noise with SNR of 30 dB, roughly corresponding to that in effect for the field data, puts $\sigma_{\lambda_\Theta} \simeq 1.1$ m. Similarly, the standard deviation of λ_Θ measured over the three range-tracks that comprise the experimental data is $\sigma_{\lambda_\Theta} \simeq 1$ m.

The uncertainty in sound speed increases for higher sediment sound speeds. The steeper propagation angles of the sub-bottom path, which are set by critical angle of the water-sediment interface, result in smaller λ_Θ as given by Eq. 6.1. The error in the λ_Θ estimate, σ_{λ_Θ}, has a greater effect on the higher sound speed parameterizations.

The uncertainty in layer thickness increases for thicker layers. This uncertainty is due to the effect of layer thickness on the propagation angle. The geometry requires thicker layers to have steeper propagation angles, which is similar to the effect of an increase in sound speed, giving smaller values of λ_Θ. Note that the change in sensitivity of the two parameters over the parameter space has implications for adaptive estimation algorithms [32], specifically the order (sequence) in which the parameters are estimated.

The coupling between these two parameters is shown by the error ellipses in Fig. 6.5(c), for several parameter combinations $[H_s, c_s]$ given $\sigma_{\lambda_\Theta} = 1.1$ m. (The intersection of the major and minor axes of the ellipses are centered at $[H_s, c_s]$.) The orientation of the error ellipses, which are determined by the eigenvectors of the $\mathbf{F}^{-1}$ matrix, show that estimates

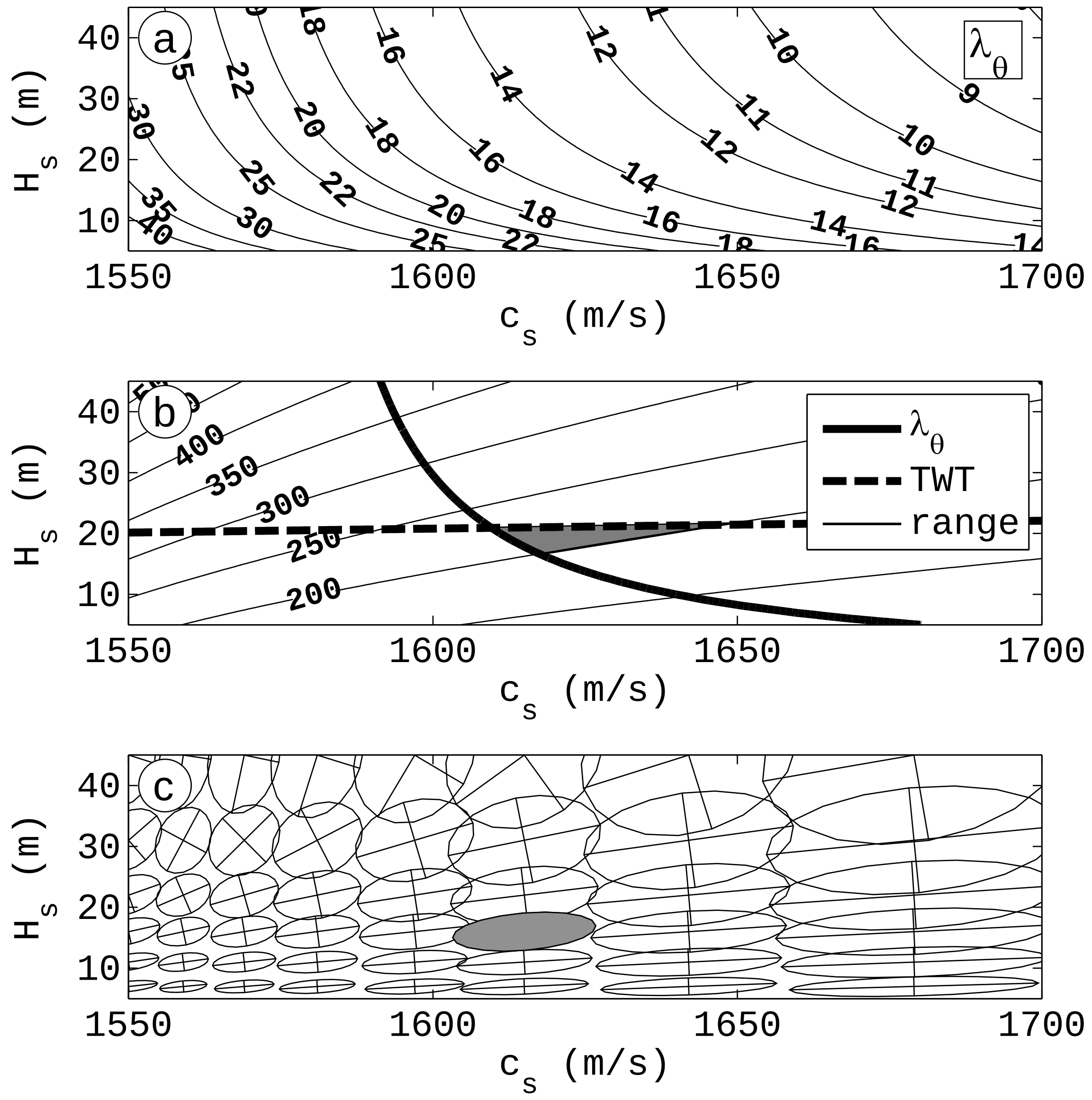

Figure 6.5: (a) Contours of λ_Θ (numbers in m) for candidate models of $[c_s, H_s]$. (b) Contours of the range (numbers in m) where the sub-bottom and direct paths arrive simultaneously. The 200-m contour corresponds to the observation in the data. The solid curved line indicates the parameter set consistent with a λ_Θ=16 m contour and the dashed line indicates the parameter set consistent with the TWT from chirp sonar data. (c) Error ellipses representing the CRLB for an uncertainty in the λ_Θ estimate, $\sigma_{\lambda_\Theta} = 1.1$ m. The grayed-filled ellipse corresponds to the uncertainty of the parameters for a best fit, $c_s = 1614$ m/s and $H_s = 16$ m.

of the two parameters are coupled, and the uncertainty in H_s depends on the uncertainty in c_s.

From the analysis of the CRLB, the uncertainties in the optimum parameter set due to the variability in the estimate of λ_Θ are ±4 m corresponding to $H_s = 16$ m, and ±10 m/s corresponding to $c_s = 1614$ m/s. The possible values of $[c_s, H_s]$ due to the uncertainty are contained in the filled ellipse in Fig 6.5(c). This error ellipse encompasses the majority of the parameter space given by shaded region in Fig. 6.5(b) and is a reasonable best-fit estimate.

Chapter 7

WAVEGUIDE EFFECTS ON PROPERTIES OF THE VECTOR FIELD

This chapter consists of results from an ocean experiment, which were published in the Journal of the Acoustical Society of America in March, 2012 [7]. The measurements used here were made in 2008 in the East China Sea, during a collaborative experiment between a team from the Applied Physics Lab, the Naval Research Laboratory and colleagues from Hangyang University, South Korea. Vertical intensity measurements of implosive lightbulb sources were used to investigate waveguide propagation. Both the experimental data and models of the intensity field are used to discuss the acoustic vector properties of the waveguide, in particular in regions of complete destructive interference, which are called dislocations.

7.1 Acoustic models: Numerical and Analytical Simulations

An analytical model of the field in a waveguide can be constructed from the time-independent Helmholtz equation, which is the Fourier transform of the wave-equation,

$$\nabla^2 p + k_0^2 n^2 p = 0. \tag{7.1}$$

where n is the index of refraction, c/c_0, where c can vary in space and c_0 is the mean sound-speed. Numerical solutions can be constructed from Eq. 7.1, which can handle depth and range dependence in sound speed, c. If we assume axial symmetry and range independent boundary conditions, an analytic solution based on the vertical modes of the waveguide can be constructed.

To develop a time-dependent solution for modeling the propagation of a pulse, narrowband solutions can be used to construct the field as a function of frequency. An inverse Fourier transform can then be applied to this broadband solution to synthesize a time-series at each grid point. Due to the finite number of simulated frequencies, it is important to properly define the source spectrum over the bandwidth of interest. For example, to simulate a Gaussian pulse with a duration T, the bandwidth of the frequency simulations should be $1/T$. The duration of the inverted time series is set by the spacing of the simulated frequencies, df in Hz, such that the final time series is $1/df$ seconds long.

7.1.1 Numerical Simulation: Parabolic Wave Equation

To handle spatial variations in the sound speed, the Helmholtz equation can be re-written as the parabolic wave equation. The parabolic wave equation is particularly useful to handle spatial variations in sound-speed, and the derivation of the parabolic wave equation can be found in F.B. Jensen et al. [33]. One particularly efficient algorithm, the RAM-PE [30], calculates the solution to the parabolic wave equation through a finite difference technique over a spatial grid. At each point on the computational grid, the medium is characterized by a soundspeed (c), density (ρ), and absorption/attenuation coefficient (α).

Since a numerical solution is limited to finite dimensions, to satisfy the Sommerfeld radiation condition of wave-propagation, which states that sound radiated to infinity will not radiate back into the domain, the environment must be constructed with perfectly matched layers. These perfectly matched layers, which have the same density and soundspeed of the boundary, act to absorb the sound at the end of the domain without causing a reflection. The sea-surface typically does not require an absorbing layer, as we can approximate the sound energy as being completely reflected. However, an additional absorbing air-layer can be added on the top of the domain to approximate in-air sound propagation, or to build a range-dependent surface to model rough-surface reflections.

The RAM-PE can model the field due to a point source in a waveguide. It is a marching algorithm, which first initializes the field at the source range, and then calculates the field sequentially at subsequent ranges. As a rule of thumb, range and depth spacing of the calculation grid should be a fraction of a wavelength of the source frequency, $\lambda/5$. This spacing allows for readily computing the components of particle velocity from finite difference methods.

7.1.2 Acoustic Modes of a Waveguide

An analytic solution can also be constructed for some basic waveguides, which does not require a marching algorithm and is quite efficient at simulating the field at long ranges. Furthermore, exact derivatives of the field can be calculated to remove any ambiguity in the analysis of intensity and particle motion. In an ocean waveguide defined by the sea-surface and horizontal sea-floor, the vertical dependence of the acoustic pressure and the components of particle velocity can be expressed as a sum of vertical modes. Each mode satisfies continuity and conservation of momentum along the boundary. At the surface, the boundary conditions are essentially equivalent to a pressure release surface, $p(0, r) = 0$. At the sea-floor, the modes satisfy the boundary conditions, parameterized by the geoacoustic properties of the sediment, c_b, ρ_b, and α.

Some additional insight into the vector properties of the acoustic field can be shown by an analytic solution to a canonical ocean waveguide model, a Pekeris waveguide. A Pekeris waveguide is defined by a pressure release surface, an iso-velocity water column, and a bottom half-space with uniform properties, ρ and c. The wavenumber, k, in the Eq. 7.1 can be written in terms of the horizontal wavenumber, which can be complex.

The acoustic field in a Pekeris waveguide is a summation of trapped pressure and particle velocity modes. The pressure field is,

$$p(z, r; t) = \sum_{n=1}^{N} A_n \Psi_n(z) H_0^{(1)}(k_n r) e^{-i\omega t}, \tag{7.2}$$

and the horizontal and vertical particle velocities are,

$$\begin{aligned} v_r(z, r; t) = & \sum_{n=1}^{N} \frac{-k_n}{i\omega\rho_0} A_n \Psi_n(z) H_1^{(1)}(k_n r) e^{-i\omega t} && (7.3) \\ v_z(z, r; t) = & \sum_{n=1}^{N} \frac{1}{i\omega\rho_0} A_n \Phi_n(z) H_0^{(1)}(k_n r) e^{-i\omega t}, && (7.4) \end{aligned}$$

where A_n is the modal amplitude, k_n is horizontal wavenumber for the n^{th} mode, and $H_0^{(1)}$ and $H_1^{(1)}$ are the zeroth and first order Hankel functions of the first kind. The mode shapes for the pressure and horizontal particle velocity (Ψ_n) are given by,

$$\Psi_n(z) = \sin(\sqrt{k^2 - k_n^2}\, z), \tag{7.5}$$

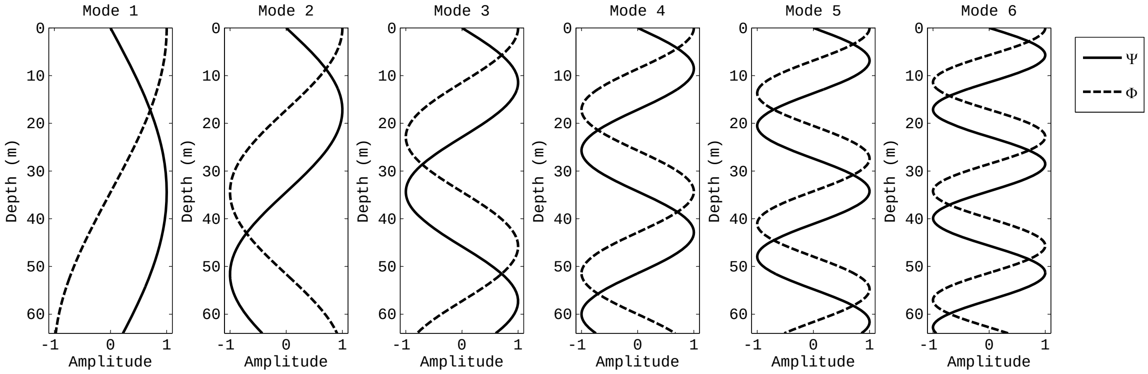

Figure 7.1: Mode shapes for the pressure and vertical particle velocity at 210 Hz in a Pekeris waveguide, depth 62 m.

and the mode shape for the vertical particle velocity (Φ_n) by,

$$\Phi_n(z) = \sqrt{k^2 - k_n^2}\ \cos(\sqrt{k^2 - k_n^2}\, z), \tag{7.6}$$

where the origin of depth coordinate z is at the surface.

Figure 7.1 shows the first six pressure and particle velocity mode shapes for a 210 Hz tone in a Pekeris waveguide, parameterized by depth 62 m, c_w = 1500 m/s, ρ_w = 1024 kg/m^3, overlaying an semi-infinite half-space, with c_b = 1600 m/s and ρ_b = 1600 kg/m^3. Since the horizontal particle velocity is the gradient of the pressure field in the direction of range, the vertical mode shapes of the horizontal particle velocity are identical to the pressure mode shapes. These six modes represent all of the completely real values of k_n. These trapped modes are perfectly reflected from the waveguide boundaries and propagate with the cylindrical spreading term.

The number of trapped modes depends on the depth of the waveguide, h, and the source frequency. As described by Frisk [20], the horizontal wavenumber, k_n, of the nth trapped mode is the real valued-pole of the eigenvalue equation, $(n - 1/2)\pi = \sqrt{k^2 - k_n^2}H + \varphi_n/2$ where φ_n is the phase of the bottom reflection coefficient. The modal amplitude for each trapped mode is derived from the boundary conditions at the sea-floor [20], and depends on the source depth,

$$A_n = \frac{i2\pi P_0 \Psi_n(z_0)}{h - \frac{\Psi_n(2h)}{2\sqrt{k^2-k_n^2}} + \frac{\rho_0}{\rho_b}\frac{\Psi_n^2(h)}{\sqrt{k_n^2-\left(\frac{\omega}{c_b}\right)^2}}}, \tag{7.7}$$

z_0 is the source depth, ρ_b and c_b are the density and sound speed of the sediment and P_0 is the source pressure amplitude, defined such that A_n has the dimension of pressure.

There are additional modes which have a complex horizontal wavenumber. The imaginary term of k_n corresponding to these modes signifies an attenuation of the propagating waves with range, caused by a reflection coefficient amplitude less than unity (indicating a portion of the energy transmitted into the sea-bed which does not return). These virtual, or improper, modes decay exponentially with increasing range and only significantly contribute to the field at ranges near the source. At ranges on the order of ten or more waveguide depths, the field can be represented solely by the sum of the trapped modes.

The vector components of $\vec{I_c}$ are found by inserting Eqs. (7.2-7.4) into Eq. 2.20. Note that the correct sign of $\vec{Q}$ depends on the sign convention of the time dependent term, requiring the particular conjugation of Eq. 2.20 for the ($e^{-i\omega t}$) convention used here [34].

With the Hankel function written in its asymptotic form (valid when $k_n r \gg 1$), $|p|^2$ is given by,

$$|p|^2 = \frac{1}{r}\sum_{m=1}^{N}\sum_{n=1}^{N} B_m B_n \cos[\triangle\kappa_{mn} r] \tag{7.8}$$

where $\triangle\kappa_{mn} = k_m - k_n$ and the pressure modal amplitude B_m is,

$$B_m = \frac{2A_m \Psi_m(z)}{\pi\sqrt{k_m}}. \tag{7.9}$$

Simplifying for just two modes, it is seen that Eq. 7.8 will go to zero (a pressure null or pressure dislocation) at a range and depth combination, such that $\cos(\triangle\kappa_{mn} r) = -1$ when B_m and B_n are of equal sign and magnitude, or $\cos(\triangle\kappa_{mn} r) = 1$ when B_m and B_n of equal magnitude and opposite sign. A null at one particular depth repeats in range at the interference wavelength, $2\pi/\triangle\kappa_{mn}$.

The active vertical intensity is given by,

$$I_z = \frac{1}{r}\sum_{m=1}^{N}\sum_{n=1}^{N} B_m C_n \sin[\triangle\kappa_{mn} r], \tag{7.10}$$

where the vertical velocity modal amplitude C_n is,

$$C_n = \frac{2A_n\Phi_n(z)}{\pi\omega\rho_0\sqrt{k_n}}. \tag{7.11}$$

At the range of the pressure null, I_z, again upon simplifying to just two modes, is zero over the entire depth of the water column due to the sine term.

The behavior of the particle motion and acoustic intensity near a dislocation is fascinating, as the value of active intensity curl, reactive intensity divergence and the particle motion circularity take on extreme values. These dislocation features can be identified by the normalized components of the acoustic intensity, as discussed next, and are further explained in Section 7.3.

7.2 Field Indicators: The Pressure Intensity Index

Normalized forms of the complex acoustic intensity, referred to as the pressure intensity indices, were first introduced by Jacobsen in the context of airborne acoustics [35]. These non-dimensional field indicators are used in the analysis of vector properties in ocean waveguides presented in Chapter 7. The pressure intensity index mirrors the complex intensity, with the active pressure intensity index defined as,

$$\vec{I}^\star = \frac{\vec{I}}{|p|^2/\rho_0 c}, \tag{7.12}$$

and the reactive counterpart defined as,

$$\vec{Q}^\star = \frac{\vec{Q}}{|p|^2/\rho_0 c}. \tag{7.13}$$

The superscript ($\star$) is used here to indicate that these are normalized, non-dimensional intensity quantities. Interestingly enough, the cross product $\vec{I}^\star \times \vec{Q}^\star$ is a non-dimensional version of $\nabla \times \vec{I}$ as formulated by Eq. 3.26. It is of interest to examine the behavior of $I_z^\star$ as range r approaches such a null location. Continuing with just the 2-mode case, expanding Eq. 7.8 and Eq. 7.10 about a null range point r_0, one can see their ratio, and thus $\vec{I}^\star$, goes as $\pm 1/dr$, where $dr = r - r_0$. The sign of $\vec{I}^\star$ indicates direction of energy flow in the active intensity vortex, the center of which is the null.

In terms of $Q_z^\star$, note that at a pressure null $Q_z^\star$ is also zero. In this case, the more interesting property is how the index behaves as a function of z going towards the null. It is worth reiterating that $Q_z^\star$ is proportional to the vertical gradient of $|p|^2$. Therefore, a similar expansion of $Q_z^\star$ about the null depth point shows that the ratio goes as $1/dz$. The sign of $Q_z^\star$ indicates convergence of $\vec{Q}$ at the null.

The behavior of $I_z^\star$ and $Q_z^\star$ about a pressure null for the case of multiple mode propagation has a structure similar to the two mode case. Figure 7.2a shows $|p|^2$ contours for a point source (210 Hz, depth of 35 m) in the Pekeris waveguide defined in Fig. 7.1. The white box outlines a region containing dislocations at a range where the pressure field is sufficiently approximated by 6 trapped modes.

Contours of $I_z^\star$ within the white box in Fig. 7.2b show vortex regions where $|I_z^\star| > 1$. The vortex center is indicated by $I_z^\star$ changing sign, describing energy flux propagating in opposite directions on either side of the pressure null. Similar contours of $Q_z^\star$ (Fig. 7.2c) indicate convergence of reactive intensity at these same null points. The box in Fig. 7.2c shows such a convergence, indicated by $Q_z^\star$ changing sign such that $Q_z^\star$ is directed inwards toward the center of the null. The behavior of $I_z^\star$ along the horizontal axis and $Q_z^\star$ along the vertical axis at the nulls show the same abrupt change in sign characterized by the two mode behavior. A key advantage of the index approach is that the pressure intensity indices are maximum at dislocations in the field, and detection of these regions (where $|\vec{I}^\star|$ or $|\vec{Q}^\star| > 1$) is feasible with one directional component, e.g., $Q_z^\star$ and $I_z^\star$ as can be provided by a vertical line array.

Finally, Figs. 7.2 (d-e) show $I_z^\star$ and $Q_z^\star$, respectively, as a function of depth and frequency at a fixed range (650 m). These form mirror images of the range depth plots in Figs 7.2 (b-c). This range and frequency relationship is described by the waveguide invariant, β. Most often applied to the range-frequency relation in $|p|^2$, uses of the β parameter include detection of internal waves [36], active sonar [37], passive range estimation [38] and source localization [39]. The waveguide invariant has also been used to describe the range frequency relationship of the active intensity[40] and reactive intensity[41]. As demonstrated next, β also applies to the indices $\vec{I}^\star$ and $\vec{Q}^\star$, with the demonstration limited here to the components of $I_z^\star$ and $Q_z^\star$.

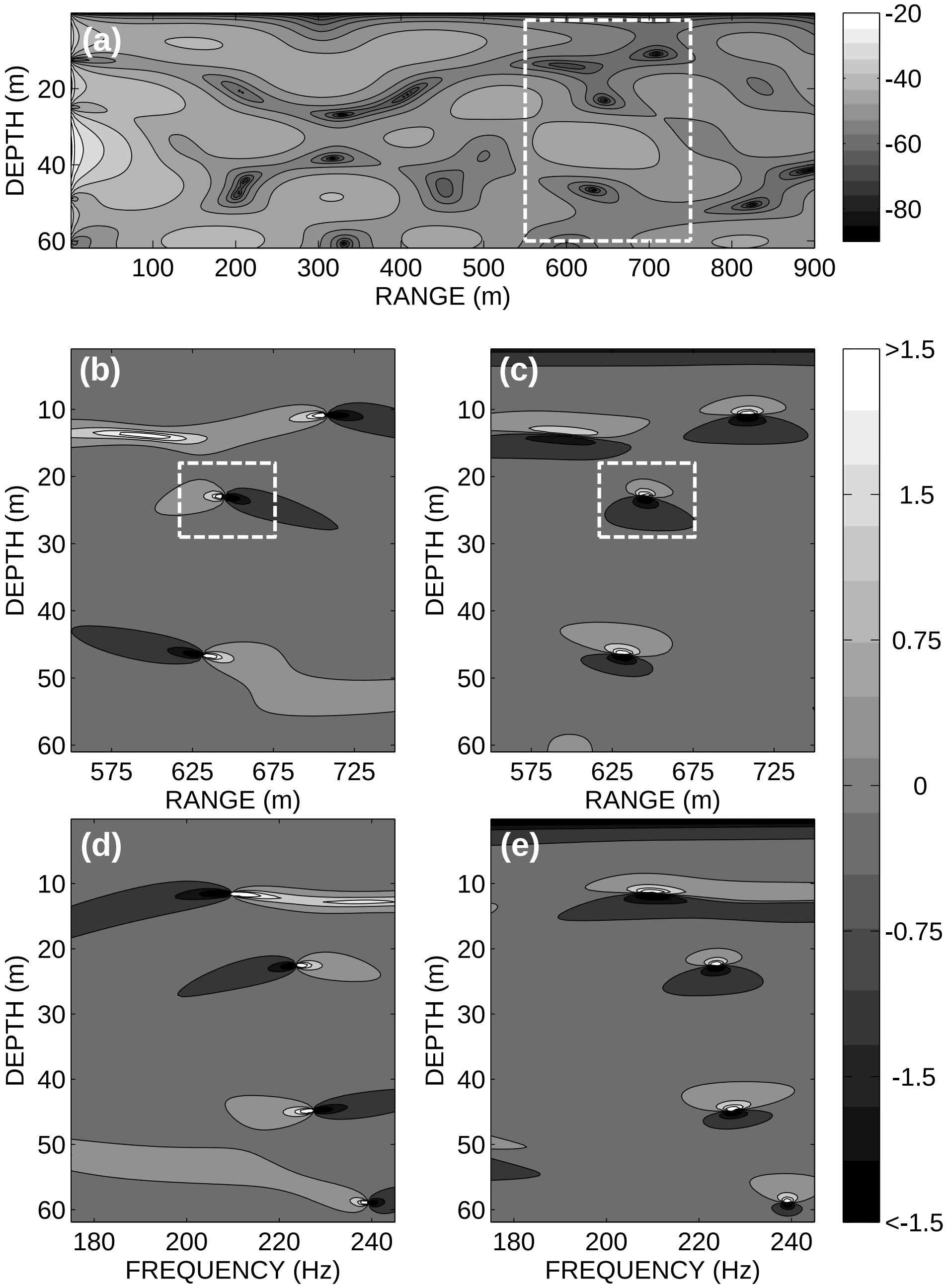

Figure 7.2: (a) $|p|^2$ in dB for a unit point source at 37 m in a Pekeris waveguide. (b) Expanded view of $I_z^\star$ and (c) $Q_z^\star$ for the white outlined box in (a). (d) $I_z^\star$ and (e) $Q_z^\star$ plotted as a function of depth and frequency at a fixed range of 650 m.

Contours of constant $I_z^\star$ in range and frequency are described by,

$$\frac{\partial I_z^\star}{d\omega} d\omega + \frac{\partial I_z^\star}{dr} dr = 0. \tag{7.14}$$

Increments of frequency $d\omega$ and range dr where $I_z^\star$ have the same contour level are found from,

$$\frac{d\omega}{dr} = -\frac{\partial I_z^\star / \partial r}{\partial I_z^\star / \partial \omega}. \tag{7.15}$$

In a Pekeris waveguide, $I_z^\star$ can be formed from Eq. 7.8 and Eq. 7.10 giving,

$$I_z^\star = \rho_0 c \, \frac{\displaystyle\sum_{m=1}^{N} \sum_{n=1}^{N} B_m C_n \sin[\triangle \kappa_{mn} r]}{\displaystyle\sum_{m=1}^{N} \sum_{n=1}^{N} B_m B_n \cos[\triangle \kappa_{mn} r]} = \rho_0 c \, \frac{\mathcal{N}}{\mathcal{D}}, \tag{7.16}$$

where $\mathcal{N}$ and $\mathcal{D}$ define the numerator and denominator, respectively. The modal amplitudes B_m and C_m are weak functions of frequency and are range independent . This holds for any normal mode description of the acoustic field in a limited bandwidth for which B_m and C_m can be approximated as frequency independent [37]. With this approximation, the right side of Eq. 7.15 is,

$$\frac{\partial I_z^\star / \partial r}{\partial I_z^\star / \partial \omega} = \frac{\mathcal{D}\frac{\partial \mathcal{N}}{\partial r} - \mathcal{N}\frac{\partial \mathcal{D}}{\partial r}}{\mathcal{D}\frac{\partial \mathcal{N}}{\partial \omega} - \mathcal{N}\frac{\partial \mathcal{D}}{\partial \omega}} = \frac{\mathcal{D}\mathcal{N}_r - \mathcal{N}\mathcal{D}_r}{\mathcal{D}\mathcal{N}_\omega - \mathcal{N}\mathcal{D}_\omega}. \tag{7.17}$$

The ratio of the partial derivatives, $\mathcal{D}_r/\mathcal{D}_\omega$, is further simplified following arguments given by Brekhovskikh and Lysanov [42]; a demonstration is provided by Quijano, et al. [37] for striation patterns in $|p|^2$. These arguments also apply to the ratio of partial derivatives, $\mathcal{N}_r/\mathcal{N}_\omega$, which leads to the same simplification, and thus reduces Eq. 7.15 to the familiar operational relation for β, namely,

$$\beta = \frac{r}{\omega} \frac{d\omega}{dr}. \tag{7.18}$$

The same functional relationship also applies to $Q_z^\star$.

7.3 Vector Properties of Dislocations

Acoustic intensity in a waveguide will exhibit a spatial structure corresponding to regions of constructive and destructive interference. These structures are characterized by the properties of the time-independent complex intensity and fall into two categories: crests and vortices.

Crests occur in regions of constructive interference where there are maxima in the $|p|^2$ field. In these regions, mean active intensity follows streamlines propagating energy away from the source; a crest follows the most energetic streamline of $\vec{I}$. Constructive interference produces gradients in the $|p|^2$ field, and as $\nabla|p|^2 \propto \vec{Q}$, the reactive intensity vector points outward from a particular maximum in the $|p|^2$ field.

Vortices occur in regions of destructive interference where there are minima in the $|p|^2$ field. The mean active intensity forms a vortex, the center of which is a null where both $|p|^2$ and $\vec{I_c}$ are zero. In the vortex region, active intensity can have a left or right-handed curl ($\nabla \times \vec{I}$), while reactive intensity converges toward the dislocation. Some experimental and simulated measurements of dislocations are described in D'Spain, et al.[41].

Theoretical work by Eliseevnin, et al. [43] shows that the spatial distribution and strength of intensity vortices is related to the difference in mode number. Although the two mode case is useful to visualize intensity structures like the vortex region, the spatial structure of intensity due to two modes is not preserved when considering the complete modal sum. Additional modes change the interference pattern, e.g., changing the number and the location of nulls in the intensity field.

To demonstrate these features, Fig. 7.3 shows a simulation of a point source 5λ from the surface of an isovelocity waveguide with sound speed c_1. The waveguide is 10λ thick and bound by a semi-infinite half-space with soundspeed c_2. The bottom interface is parameterized by a sound-speed ratio, $n = c_1/c_2$, and density ratio, $m = \rho_2/\rho_1$, with $n = 0.9$ and $m = 1.6$.

Figure 7.3a shows magnitude, in log space, of the active intensity field due to a single frequency. The active intensity magnitude has been normalized by the maximum value at $r = 1$. Since the waveguide is parameterized in terms of λ, this graphic is frequency

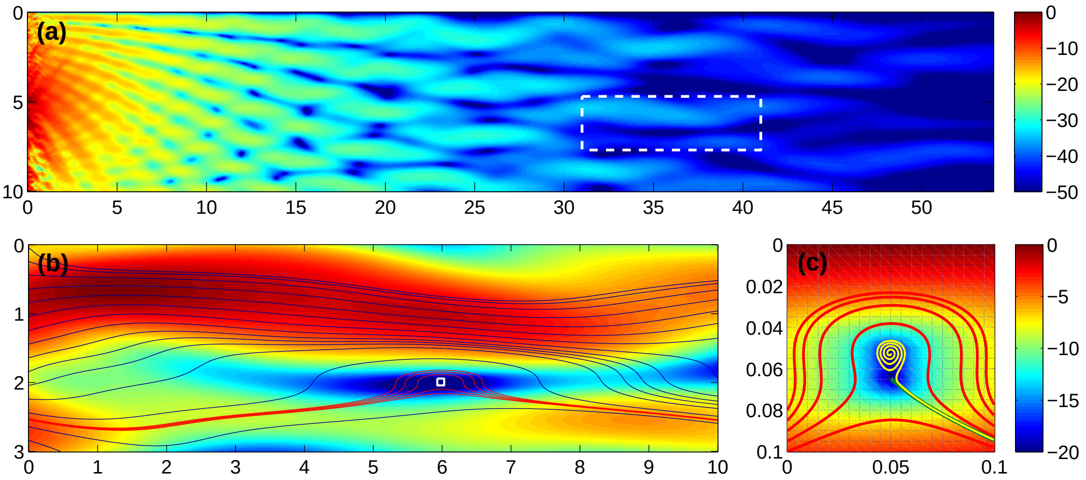

Figure 7.3: (a) An image of the pressure magnitude, in dB referenced to the level at 1 m from the source. Range and depth expressed in number of wavelengths λ , where the source depth is 5λ (b) An image of the magnitude of the active intensity in dB, scaled to its maximum value, of the region indicated by the white box in (a), and corresponding intensity streamlines. (c) An enlargement of the active intensity in the region indicated by the white box in (b), rescaled by the maximum in this region, and corresponding intensity streamlines.

independent and gives some insight into the spatial scale of both crest and vortex regions. Figure 7.3b shows a portion of the active intensity field (rescaled to the maximum active intensity in the white box in Fig. 7.3a) that contains both crests and null features. The black streamlines, initiated at a equal depth spacing $\lambda/5$, converge along the crests in active intensity. A subset of red streamlines show the behavior of intensity streamlines approaching a vortex region, and follow a trajectory to either side of the vortex center.

The spatial structure of this active intensity vortex plotted in the small white box in Fig. 7.3b is magnified in Fig. 7.3c, again rescaled by the maximum intensity magnitude. The vortex region contains two nulls in active intensity, one at the vortex center (which corresponds to a null in pressure and thus zero active and reactive intensity), and another where the vertical active intensity flips sign. Streamlines initiated at these two nulls (yellow at the vortex center, and green at the other) eventually converge along an active intensity crest. The red streamlines are the same as those in Fig. 7.3b.

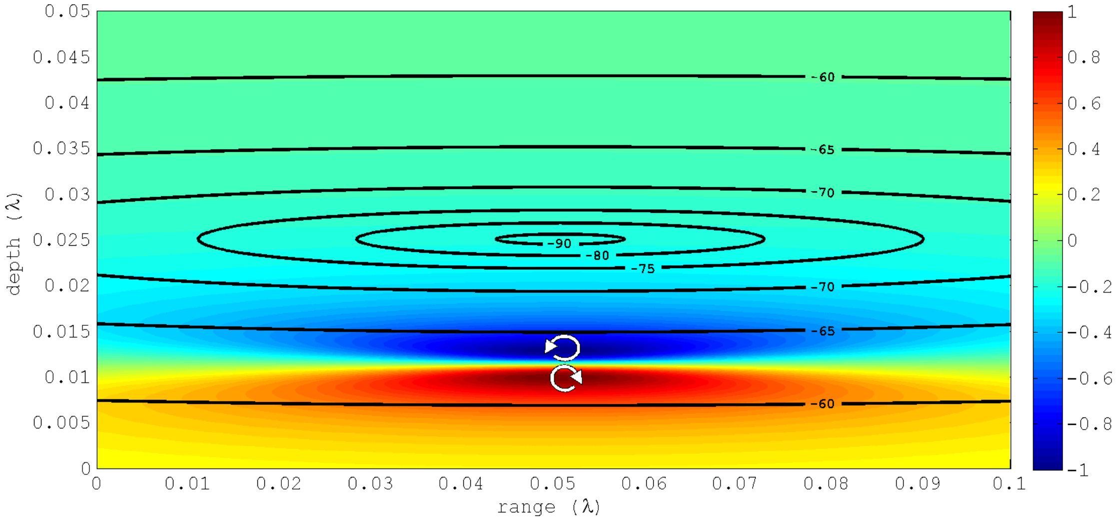

Figure 7.4: An image of the value of Θ in a vortex region shown in Fig. 7.3, with contours of the pressure magnitude (in dB) shown by the black lines. Exaggerated particle motion paths are shown for two points near the saddle point, which have opposite sign of Θ.

Figure 7.4 shows an enlargement of the vortex region, with contours of pressure magnitude (in dB corresponding to the scale in Fig. 7.3a), plotted over an image of Θ. The particle motion behavior in a vortex region becomes perfectly circular, corresponding to a value of $\Theta = \pm 1$ just above and below null in active intensity. Exaggerated particle motion paths are plotted over the image of circularity, and their polarization is shown by the arrow head. It is interesting to note that the reactive intensity is convergent at the center of the vortex, the pressure null. In the region between the vortex center and the saddle point, the sign of the vertical component of reactive intensity and the circularity are opposite. It is only in this small region where approximations to the circularity fail, as discussed in Sec. 4.2.3. Experimental observations of divergent reactive intensity caused by an impulse source have indicated vortex regions, and is discussed next.

7.4 Experimental Observations of the Vertical Intensity

The experiment was conducted 17 km northeast of the South Korean ocean research station (Ieodo) in waters 63 m deep, and formed a component of a larger program known as the Transverse Acoustic Variability Experiment (TAVEX). Acoustic pressure data was collected on a 16-element vertical line array (VLA) with uniform hydrophone spacing (d) of 3 m. The sampling frequency of the measurement system is 20.47 kHz. The source signals were implosions of light bulbs (air volume 700 cm^3) at a nominal depth of 40 m off the stern of the R/V *Sunjin*. Due to wind coupling of the research vessel and the resulting relative motion of the vessel with respect to the water column, the bulb deployment system was suspended at an angle from vertical resulting in bulb implosion depths estimated to be 37 m. The key feature of the implosion signal is a long-time scale rarefaction signal, followed by a impulsive-like spike in pressure. This sequence (bubble pulse) is repeated every 4.7 ms with an exponential decay, similar to that described by Heard [44].

Figure 7.5a shows the locations of the bulb sources relative to the moored VLA. The arrows represent the depth-average current vector during each bulb implosion, inferred from a two-week acoustic Doppler current profiler (ADCP) record collected within 1 km of the VLA site. Although the current measurements began the day after the acoustic measurements, the daily tidal signal in the ADCP data shifts very little over the two week measurement period, and thus the current properties during the two hour period of the acoustic measurements on August 21, 2008 are inferred.

During the time period of the experiment, the magnitude of the current was ~ 0.6 m/s and slowly shifted direction from NW to N. The VLA is subjected to a depth dependent tilt in the direction of the current. The relative receiver locations, estimated from ray arrival-times of the four closest sources suggest that the array shape remains relatively constant with respect to the current direction (Fig. 7.5b). Environmental data from the nearby Ieodo tower indicated a 7 m/s southerly wind, and seas characterized by an root-mean squared (rms) wave-height, H_{rms}, of 0.475 m. SSP measured from three expendable bathythermograph (XBT) casts during the experiment show a downward refracting environment.

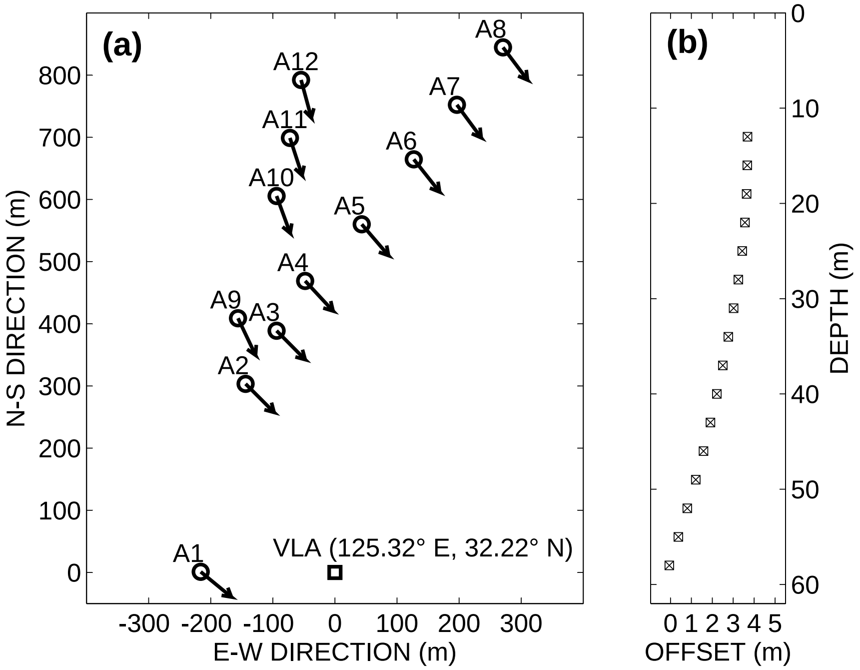

Figure 7.5: (a) Source locations (circles) relative to the VLA (square) plotted with their estimated ocean current vector. The labels A1-A12 denote the time sequence of the bulb implosions, occurring over a two hour period. (b) Estimated array shape (relative hydrophone offset) corresponding to a tilt directed along the current vector for each bulb source.

7.4.1 Instantaneous and Complex Vertical Intensity from the VLA

A reliable estimate of the instantaneous intensity based on the finite difference approximation requires low-pass filtering of the pressure time-series, before computing the particle velocity to satisfy d/λ requirements. To demonstrate the behavior of the instantaneous intensity for the first three arrivals, the filter bandwidth must be wide enough to resolve the time-separated arrivals. Typically, finite difference constraints on frequency for a given sensor spacing are set to meet an acceptable percent error in an unknown acoustic field.

The error for the finite difference approximation is a function of frequency and arrival angle. In situations where the field can be described as locally planar, the finite difference error in particle velocity is,

$$e(v_x) = 1 - \frac{2\sin\left(\frac{kd\sin\theta}{2}\right)}{kdsin\theta}, \tag{7.19}$$

and for pressure is,

$$e(p) = 1 - \cos\left(\frac{kd\sin\theta}{2}\right). \tag{7.20}$$

The error only effects the magnitude of intensity component along the axis separating the two sensors. The error in magnitude is equal the sum of Eq. 7.19 and Eq. 7.20 [4].

There is no inherent phase error in estimating pressure and vertical velocity and the existence of reactive intensity should not be attributed to errors in the finite difference technique. Measurements may suffer from other sources of errors due to imperfections in the measurement system. Such an error in the active intensity is due to phase mismatch between two sensors. An error in the reactive intensity is due to amplitude mismatch between two sensors [45]. Fortunately, the errors discussed here are not an issue when considering simulated data, which in turn validate the observations in the experimental data.

By limiting the analysis to propagation angles near broadside (where broadside represents $\theta = 0°$), the finite difference error can be kept below the aliasing frequency, preserving the correct sign of pressure and particle velocity. Here, the aliasing frequency occurs when the sign of the pressure estimate at the midpoint used in the finite difference approximation is no longer preserved, most easily interpreted for an endfire arrival ($\theta = 90°$) when $d = \lambda/2$.

Considering wavelengths that are small in comparison to the waveguide depth, ray theory can be employed, using the experimental SSP in Fig. 7.6a, to determine characteristics of the first three arrivals. Arrival angles of the first three eigenrays for the closest source location (A1), shown in Fig. 7.6b, correspond to an average finite difference error in intensity at 360 Hz of 2% for the direct path (black); 22% for the surface path (light gray); and 41% for the bottom path (dark gray), all below the aliasing frequency. Note that this source range is particularly interesting as the time-series exhibit temporal separation between the peak arrivals of the first three acoustic paths at some depths, and multi-path interference at others.

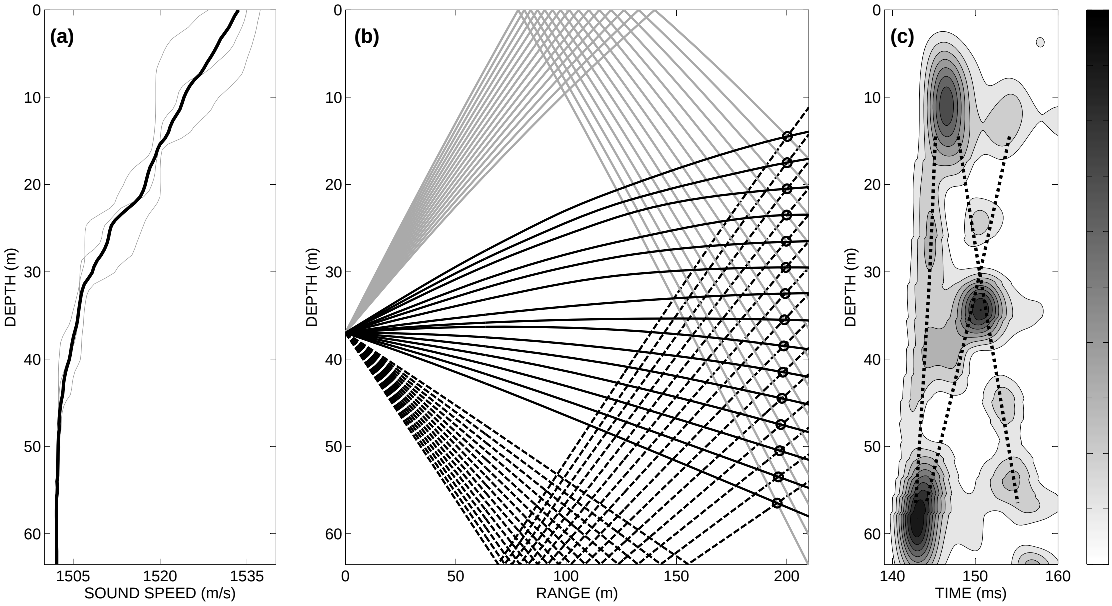

Figure 7.6: (a) The average soundspeed profile, SSP, (black) used in numerical simulations is derived from three experimentally measured SSP (gray). (b) Eigenrays of the direct path (solid black), surface path (gray) and bottom path (dashed) for the midpoints of the 15 hydrophone pairs (circles). (c) Contours of $|p|^2$ of a simulated bulb pulse, $B = 300$ Hz and $f_0 = 210$ Hz, formed by a Fourier synthesis of parabolic equation (PE) numerical solutions. Arrival times of the first three eigenrays (dotted), computed from ray theory, are plotted over the contours.

A simulated pressure times-series of the VLA data for the A1 source is constructed to evaluate the effect of the downward refracting SSP and multi-path interference on the received signal. The simulated time-series, $B = 300$ Hz and $f_0 = 210$ Hz, is generated from a Fourier synthesis of parabolic equation (PE) simulations. Figure 7.6c shows contours of $|p|^2$ as a function of time and receiver depth. The source/receiver range of the VLA sensors are dependent on the array tilt, and the approximated tilt during the A1 signal is incorporated into this simulation. The arrival times of the first three eigenrays are plotted (dotted line) over the contours to highlight the arrival times of these paths. There are two kinds of gradients in $|p|^2$, beyond that accounted for by spherical spreading, observed along the vertical axis of the simulated times series. One is due to constructive and destructive interference caused by multi-path interference; the other is due to refraction, owing to the

SSP, which generates a focusing and defocusing of the wavefronts. As reactive intensity is directed along decreasing $|p|^2$ contours [41], we can anticipate a degree of reactive intensity that will be observable in these two regions.

With results of Fig. 7.6 in mind, we now examine the field data. For each pair of neighboring receivers, the instantaneous and complex intensity component directed along the array is formed by Eqs. (2.11) and (2.20). In the coordinate system used here, where the origin is placed at the top of the array (14.5 m), negative intensity indicates energy propagating toward the surface. Figures 7.7a and 7.7b show a normalized component of $\vec{S}(t)$ (dashed) computed from the receiver pair pressure signals at 32.5 m depth, processed by a bandpass filter ($B = 300$ Hz and $f_0 = 210$ Hz), and normalized by the maximum squared pressure divided by $\rho_0 c$, the characteristic impedance where ρ_0, once again, is the density of the medium and c is the nominal sound speed.

At this depth, the component of $\vec{S}(t)$ along the array starts off as being predominantly negative, as the energy flux associated with the direct path passes the sensors. As the surface reflected and bottom reflected paths arrive at the receiver pair (nearly simultaneously according to the ray arrival times in Fig. 7.6c), the instantaneous intensity becomes oscillatory, i.e., with reduced time average, which is a characteristic of interference between the two paths. If the surface and bottom arrivals were sufficiently time separated, the instantaneous intensity would appear to be on one side of the axis (positive for the surface arrival and negative for the bottom arrival).

The active intensity, normalized in the same manner as the instantaneous intensity, is plotted over the instantaneous intensity in Fig. 7.7a by the thick black line. Similarly, the reactive intensity envelope is plotted in Fig. 7.7b as the thick gray line. The negative active intensity indicates energy flux traveling up the array during the direct arrival, which then switches to positive, indicating energy flux traveling down the array (away from the surface) during the subsequent arrival. Even though there is energy traveling upwards from the bottom arrival, the signal is dominated by the surface path and the interference between these opposing energy fluxes produces a strong component of reactive intensity.

There also is a small component of reactive intensity associated with the direct arrival observed in the data at 5 ms in Fig 7.7b. This component of reactive intensity may be

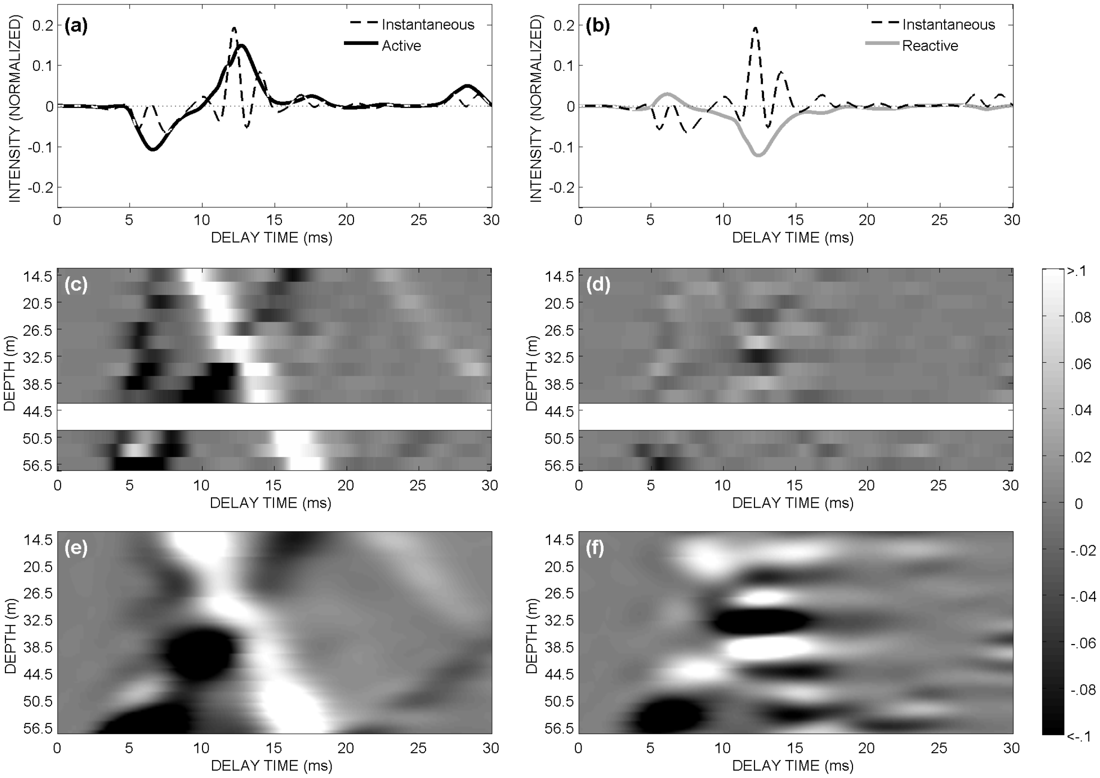

Figure 7.7: (a) The component of instantaneous intensity (dashed) and the active intensity envelope (solid black) oriented along the array at depth 32.5 m for the bulb-pulse at 190 m range. (b) The same component of the instantaneous intensity (dashed) plotted over the reactive intensity envelope (solid gray). The intensities are normalized by the maximum value of $|p|^2/\rho_0 c$. (c) Image of the active intensity envelope measured along the length of the array. (d) Image of the reactive intensity envelope measured along the length of the array. Whited out regions correspond to a 6 m gap in data due to an inoperable hydrophone. (e) Image of the active intensity envelope along the modeled VLA array shape for a PE simulated bulb pulse. (f) Image of the corresponding reactive intensity envelope. Active and reactive intensity images are normalized by the depth average of the maximum value of $|p|^2/\rho_0 c$.

due to refraction and subsequent focusing associated with the SSP, as seen in contours $|p|^2$ of the PE simulation in Fig. 7.6c. The SSP-dependent focusing, which has the greatest effect on the direct path, does not produce the level of reactive intensity that was observed during interference between the surface and bottom paths. The sign of the reactive intensity envelope does not necessarily describe the direction of the instantaneous energy flux, but it does provide an indication of the proximity and direction of gradients in $|p|^2$.

These intensity features, created from both focusing and multi-path interference, have a spatial structure observable along the length of the VLA. Figures 7.7c and 7.7d show the component of the active and reactive intensity envelopes, respectively, measured along the array for the A1 bulb range. In this case, the intensity envelopes are normalized by a constant equal to the depth average of the maximum magnitude squared pressure divided by $\rho_0 c$. As mentioned earlier, the active intensity envelope denotes the direction of propagating energy flux, negative indicating energy flux up the array toward the surface. Figures 7.7e and 7.7f show the active and reactive intensity envelopes of a simulated bulb-pulse measured along the tilted array. The simulated bulb-pulse is from a Fourier synthesis of PE simulations over a 300 Hz bandwidth, centered at 210 Hz, and shaped by the bulb-signal spectrum. As with the real data, the simulated data show a direct arrival propagating up the array, a surface path down the array, and a bottom path traveling up the array. The simulated data is not subject to the degree of granularity inherent in such experimental observations, based on the larger depth separation of the VLA hydrophone elements. The spatial structure of the reactive intensity provides information on the interference field.

The direction of the reactive intensity measured along the array gives an indication to the divergence of $\vec{Q}$. In a region about a maxima in the $|p|^2$ field reactive intensity is divergent ($\nabla \cdot \vec{Q} > 0$) and $\vec{Q}$ points outward from the maxima. At a minima in the $|p|^2$ field reactive intensity is convergent ($\nabla \cdot \vec{Q} < 0$), and $\vec{Q}$ points toward the minimum. Therefore, in this coordinate system, a change along the array, from positive to negative with increasing depth, indicates a sink of $\vec{Q}$, while a change from negative to positive indicates a source of $\vec{Q}$. The data suggests a sink of $\vec{Q}$ between 29-33 m, created by destructive interference of the surface and bottom arrivals, and a source of $\vec{Q}$ between 35-39 m, created by the constructive interference. These features are also observed in the simulation. Sinks of reactive intensity are defining characteristics of intensity in the waveguide, and occur coincidentally with an active intensity vortex.

7.4.2 Time Averaged Complex Intensity

At ranges greater than a few waveguide depths, a signal requires a large bandwidth to exhibit time separation between multipaths. The frequency span of the filter applied to the experimental measurements should be set to minimize measurement errors. However, reducing the filter bandwidth has the consequence of reduced time resolution and multipaths are no longer resolved. As the bandwidth is reduced to form an ever more narrow band signal at center frequency f_0, the complex intensity loses its time dependence and $\vec{I}$ and $\vec{Q}$ can be represented by a single steady state value (of positive or negative sign), transforming $\vec{I}_c$ into a time-independent function of frequency.

It is worth further clarifying the role of bandwidth B in constructing the complex intensity envelope, and subsequent time averaging. Figure 7.8 illustrates a partitioning of the 300 Hz bandwidth data previously shown in Figs. 7.7a and 7.7b, into frequency bins located at f_0 by applying filters with a smaller B to the signal. Figures 7.8a and 7.8c show examples of the data filtered with $B = 10$ Hz at three different center frequencies, f_0. Estimates of the component of $\langle\vec{I}\rangle$ and $\langle\vec{Q}\rangle$, measured along the array from a filter ($B = 10$ Hz), are highly dependent on the center frequency. For example, at $f_0 = 205$ Hz, shown in Fig. 7.8b, the $\langle\vec{I}\rangle \approx 0$ and $\langle\vec{Q}\rangle \approx -.05$ while at $f_0 = 255$ Hz, shown in Fig. 7.8c, $\langle\vec{I}\rangle \approx 0.3$ and $\langle\vec{Q}\rangle \approx 0$. Figure 7.8d shows a summary of $\langle\vec{I}\rangle$ and $\langle\vec{Q}\rangle$ for the frequency bins spanning the 300 Hz bandwidth. Although the two processing schemes result in very different time series, the sum of $\langle\vec{I}\rangle$ and $\langle\vec{Q}\rangle$ over the 300 Hz band shown in Fig. 7.8d give the same estimate of $\langle\vec{I}\rangle$ and $\langle\vec{Q}\rangle$ from a single 300 Hz bandwidth filter.

The time-average of the active intensity envelope, $\langle\vec{I}\rangle$, represents the mean flow of energy and is equivalent to the time-average of instantaneous intensity, $\langle\vec{S}\rangle$ [19]. The time-average of the reactive intensity envelope, $\langle\vec{Q}\rangle$, indicates the presence of a non-propagating, oscillatory component of $\vec{S}$ over the averaging period. This oscillatory component (e.g., here due to multipath interference) depends on the degree to which p and $\vec{v}$ were not in phase during

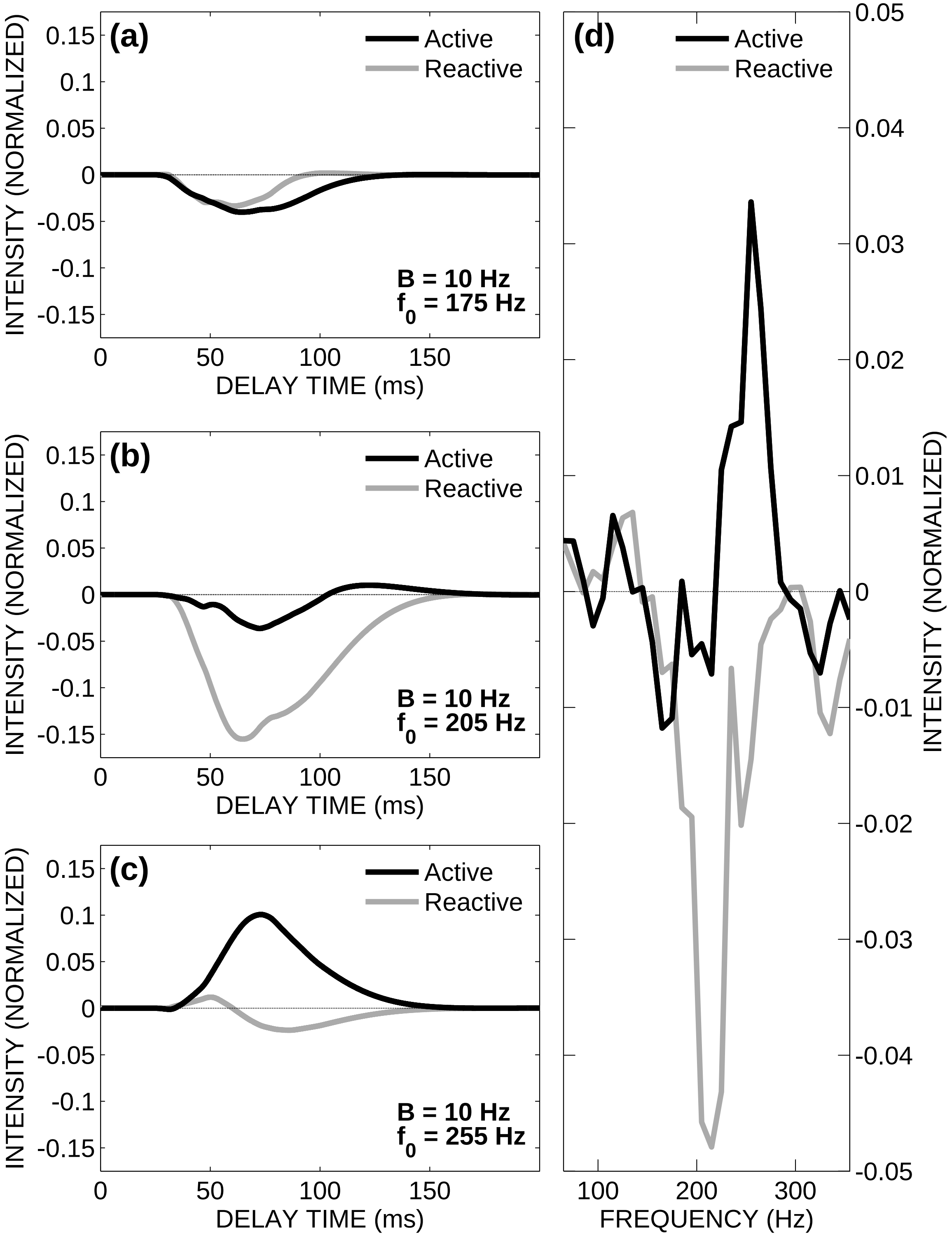

Figure 7.8: (a-c) Time-series of the active (black) and reactive (gray) intensity envelopes at the 32.5 m for three filters with B=10 Hz at three different center frequencies for the A1 bulb signal (range 190 m). (d) Time-averages of narrow-band filtered signals at the 32.5 m depth, B=10 Hz, spanning 300 Hz and centered at 210 Hz.

the averaging period. The time-independent $\vec{I}_c$, as constructed from narrow-band $\langle\vec{I}\rangle$ and $\langle\vec{Q}\rangle$, is used hereafter to describe the spatial structure of intensity.

When analyzing signals that do not exhibit time separation, it is useful to describe $\vec{I}_c$ as a time-independent function of frequency. One frequency transformed description is provided by the time-averaged narrow band intensity envelopes, as depicted in Fig. 7.8d. The Fourier transform of the time-series provides another representation of time-independent complex intensity. The time-independent $\vec{I}$ and $\vec{Q}$ are functions of frequency, range and depth. Intensity features, as characterized by their spatial structure, exhibit a strong relationship between range and frequency based on the waveguide invariant (see Eq. 7.18).

7.4.3 Intensity Structure in the TAVEX Waveguide

In this section, the range-frequency relationship in $I_z^\star$ and $Q_z^\star$ is examined in the context of the TAVEX waveguide, using a combination of field data and parabolic equation (PE) simulation. PE simulations of the complex intensity field for a point source in the TAVEX waveguide allow for finer spatial and frequency resolution of $\vec{I}^\star$ and $\vec{Q}^\star$.

For the PE simulations, the enviromental model consists of the average SSP [Fig. 7.6] and an experimentally derived bottom model. For the latter, time-separated bottom reflected paths corrected for spreading loss are used to construct an empirical relation for the magnitude of the bottom pressure reflection coefficient (Fig. 7.9), where spreading loss and arrival angle are derived using ray theory. The representative bottom model (black, dashed line) is defined by $c_b/c_w = 1.06$, density 1600 kg/m^3, and $\alpha_b = 0.019$ dB/m, α (the absorption coefficient) applies to the simulation frequency of 210 Hz, and originates from a model for averaged properties for sediments in this region [46]. Historical sedimentological data [47] and a chirp sonar bottom profile of the experimental site are consistent with the estimated bottom model. The PE simulations of intensity vector properties are carried out by application of finite differencing of a fine spatial sampling. The depth and range computational steps are set to be less than 10% of a wavelength of the maximum simulated frequency.

The time-independent $\vec{I}_c$, based on the Fourier components of the pressure and vertical

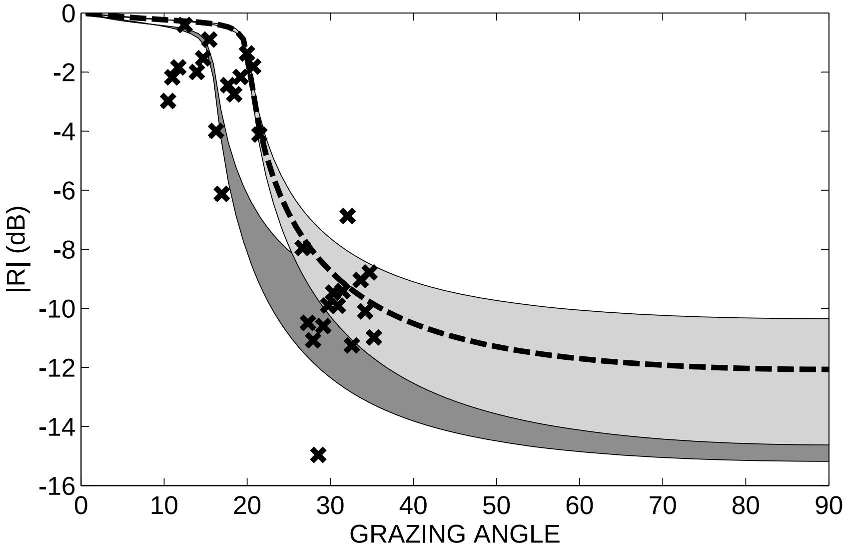

Figure 7.9: Estimates of bottom reflection coefficient (x) for two sound speed ratios $c_b/c_w = 1.04$ (dark gray) and $c_b/c_w = 1.065$ (light gray) over a range of bottom densities 1400 to 1800 kg/m^3. The representative bottom model (black, dashed) has $c_b/c_w = 1.065$ and $\rho_b = 1600$ kg/m^3 and $\alpha_b = 0.019$ dB/m.

particle velocity, are used to construct narrow band estimates of $I_z^\star$ and $Q_z^\star$ with the TAVEX data as a function of frequency, based on B=1 Hz with f_0 ranging from 110-310 Hz. For ease in notation, $I_z^\star$ and $Q_z^\star$ are used to denote the measurement along the VLA, which is influenced by the array tilt shown in Fig. 7.5. The measurements in fact represent a vector sum of the two directional components, according to the tilt of the hydrophone pair used in the intensity formulation. Although the tilt can have a substantial effect on approximating the true value of $I_z^\star$, the horizontal component $I_r^\star$ is typically directed away from the source. The direction of the tilt amounts to a positive or negative shift in the approximate $I_z^\star$. The normalized quantity $Q_z^\star$, on the other hand, is quite robust to errors stemming from array tilt, as the horizontal component, $Q_r^\star$, is nearly zero for ranges greater than a few wavelengths. Errors in measurement aside, the frequency range relationship described by the waveguide invariant holds for any directional component of $\vec{I}^\star$ and $\vec{Q}^\star$.

Figures 7.10a and 7.10b show $I_z^\star$ and $Q_z^\star$, respectively, as a function of frequency for the

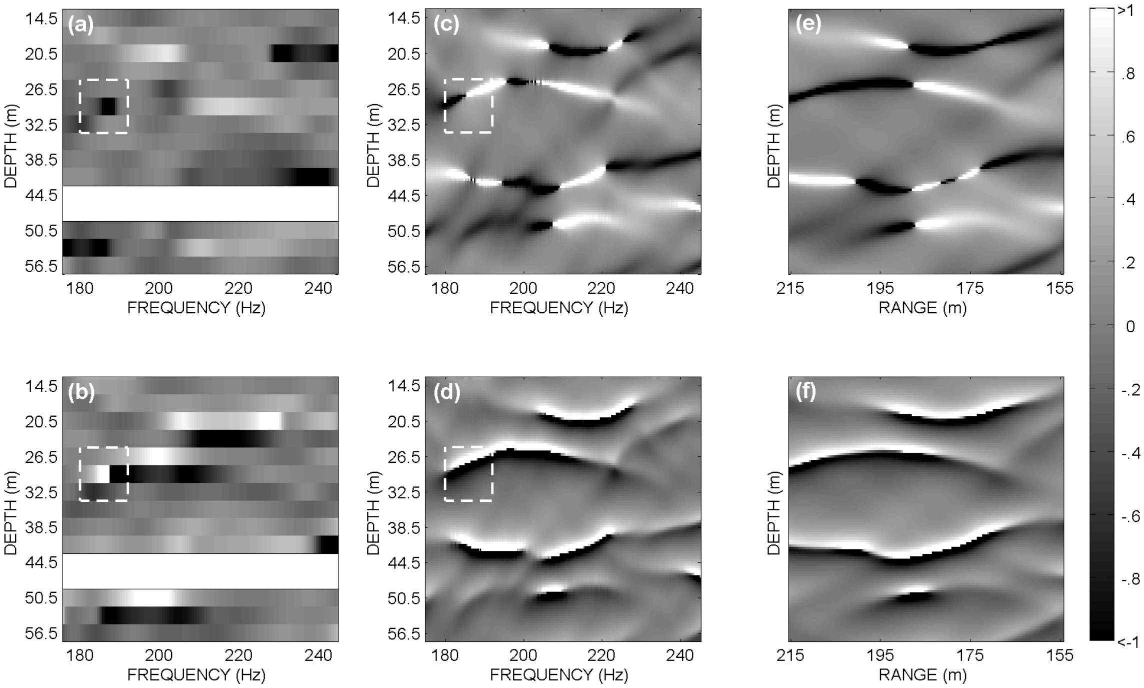

Figure 7.10: (a) Experimental estimates of $I_z^\star$ as function of frequency and depth corresponding to the closest bulb range A1; (b) corresponding estimates of $Q_z^\star$. Whited out regions correspond to a 6 m gap in data due to an inoperable hydrophone. (c) PE simulated estimates of $I_z^\star$ as a function of frequency and depth at the A1 bulb range (190 m) and based on a source depth of 37 m; (d) corresponding estimates of $Q_z^\star$. The white box highlights a dislocation. (e) PE simulated estimates of $I_z^\star$ as function of range and depth at frequency 210 Hz; (f) corresponding estimates of $Q_z^\star$.

13 vertical intensity receiver depths at the source range (190 m), calculated from the same data shown in Fig. 7.7. Values where $|I_z^\star| > 1$ suggest a dislocation is nearby, but the depth resolution is not adequate to resolve it precisely. The PE simulations of $I_z^\star$ (Fig. 7.10c) and $Q_z^\star$ (Fig. 7.10d) pinpoint a dislocation at 27 m depth and frequency 187 Hz, indicated by a convergence of $Q_z^\star$ in depth when $|Q_z^\star| > 1$, in conjunction with $|I_z^\star| > 1$. Applying this observation to the data suggests that there is indeed a dislocation between 26m and 33 m depth at frequency 187 Hz as suggested by the combination of $|I_z^\star| > 1$ and $Q_z^\star$ being convergent, highlighted in the box in Figs. 7.10a and 7.10b.

It is next of interest to compare the PE simulation of $I_z^\star$ and $Q_z^\star$ as a function of frequency at a fixed range, and as a function of range at fixed frequency. Fig. 7.10c and 7.10d show $I_z^\star$ and $Q_z^\star$, respectively, as function of frequency at a range of 190 m. The results are similar to those measured experimentally, shown in Fig. 7.10a and 7.10b. Fig. 7.10e and 7.10f show $I_z^\star$ and $Q_z^\star$, respectively, as function of range at a center frequency 210 Hz. The center frequency 210 Hz is used here because it corresponds to a peak in the bulb signal spectrum. These figures shows how $I_z^\star$ and $Q_z^\star$ are clearly related in both range and frequency. For this PE simulation, the frequency range relationship follows that of Eq. 7.18, with a value of $\beta \approx 1$.

Figure 7.11 shows the result of PE simulations of the spatial structure of $I_z^\star$ and $Q_z^\star$ at 210 Hz over the entire range relevant to the TAVEX experiment. A single frequency simulation can be reconstructed by a small set of fixed-range simulations, but at each fixed-range, the simulation is computed over a band of frequencies. The frequency band is then interpreted as a range band according to Eq. 7.18, using $\beta = 1$. The single frequency $I_z^\star$ in Fig. 7.11a is reconstructed in 7.11b by multiple frequency simulations at 24 discrete ranges (separated by the black vertical lines). The single frequency $Q_z^\star$ simulation, plotted in Fig. 7.11c, is reconstructed in Fig. 7.11d. In other words, $I_z^\star$ and $Q_z^\star$ in Figs. 7.11b and 7.11d are computed as a function of frequency between 175 Hz and 245 Hz at discrete source ranges spaced every 50 m. The mapping from frequency to range around a center frequency of 210 Hz, and subsequent reconstruction of $I_z^\star$ and $Q_z^\star$ versus range, display the same intensity spatial structure observed in the original narrow band simulation shown in Figs. 7.11a and 7.11c.

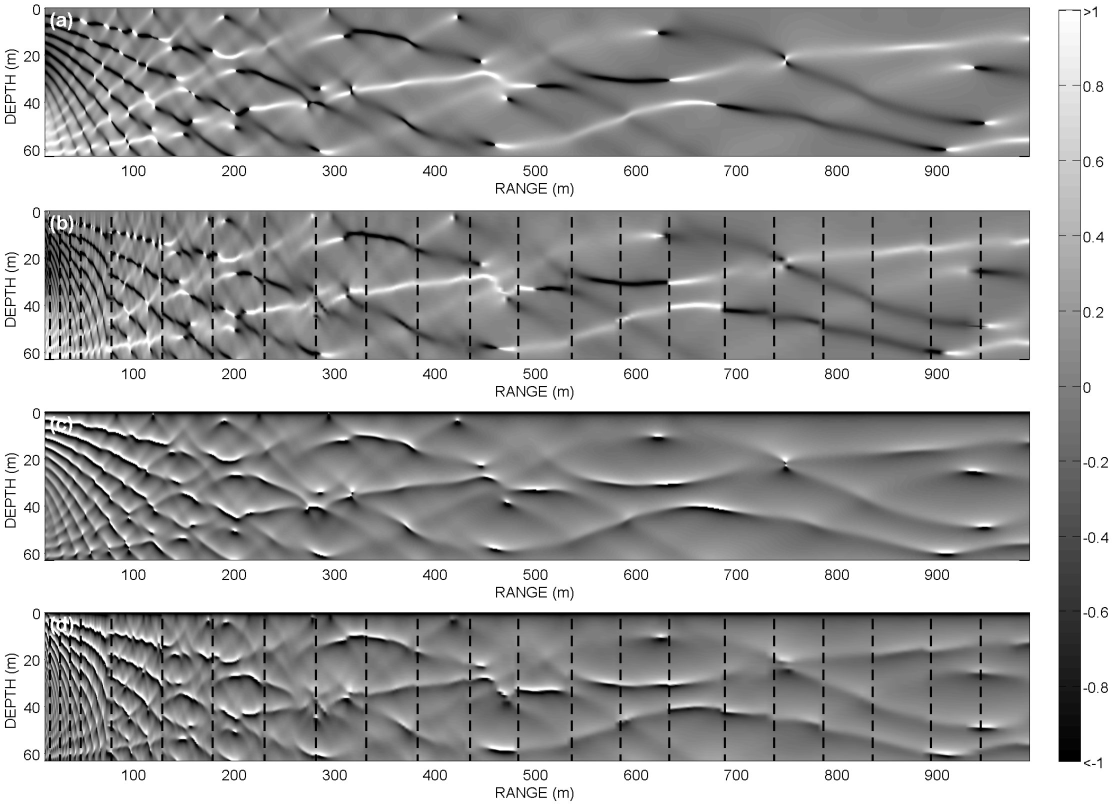

Figure 7.11: (a) Single frequency PE simulation of $I_z^\star$ at 210 Hz and (b) the reconstruction of $I_z^\star$ at 210 Hz from multiple frequency simulations at 24 discrete ranges (separated by dotted vertical lines) using the TAVEX waveguide model (see text). Dislocations are located at the sharp transitions from large positive value ($I_z^\star > 1$) to a large negative value ($I_z^\star < -1$). (c) Single frequency PE simulation of $Q_z^\star$ at 210 Hz and (d) the reconstruction of $Q_z^\star$ at 210 Hz from multiple frequency simulations. The single frequency $I_z^\star$ and $Q_z^\star$ are reconstructions are performed by a mapping of frequency to range using the nominal shallow water waveguide invariant value ($\beta = 1$).

The dominant feature indicated by $I_z^\star$ are dislocations, or nulls, indicated by abrupt changes in sign along "bands" of elevated $I_z^\star$ (where $|I_z^\star| > 1$). These dislocations often represent a vortex in active intensity, occurring at the point when a band narrows before undergoing an abrupt change in sign. Bands of $I_z^\star$ trace out a pattern related to the modal structure of the field. In the 2-mode propagation case, dislocations repeat at the interference wavelength. In the case of multi-mode propagation, the actual dislocations may not repeat at the interference wavelength, but the bands of $I_z^\star$ have a characteristic structure associated with the multiple interference wavelengths, as shown in Figs. 7.11a and 7.11b. Along the bands of $I_z^\star$, there is also a seam of convergence in reactive intensity, indicated by $Q_z^\star > 1$ above and $Q_z^\star < 1$ below the seam, or white above black in the in Fig. 7.11c and 7.11d.

There are some features in the narrow band case which are not perfectly recreated in the mapping. At the interface between two ranges, the curves are not perfectly aligned. This could be attributed to depth dependence of the β parameter, caused by the downward refracting SSP [48]. In the case where the sign of $I_z^\star$ is opposite, the frequency dependence of the modal amplitudes may come into play, which is neglected when deriving the waveguide invariant [41].

A similar range frequency relationship of $I_z^\star$ and $Q_z^\star$ is also observable in the experimental data between two nearby bulb ranges. Figures 7.12a and 7.12b show $I_z^\star$ for two sources deployed at A6 (675 m) and A10 (698 m), respectively. Figures 7.12c and 7.12d show the corresponding $Q_z^\star$. The general pattern of the pressure intensity indices, as indicated by regions of elevated $I_z^\star$ in Fig. 7.12a) and convergent $Q_z^\star$ in Fig. 7.12c (highlighted by the dotted lines), at range 675 m are up-shifted in frequency by ~7 Hz at range 698 m. The frequency shift is itself somewhat frequency dependent over the 175-245 Hz range, but the average of 7 Hz puts $\beta \sim 1$. Depth dependence of β is difficult to quantify with this experimental data set, due to uncertainties in the source location and possible changes in the relative receiver positions or SSP, as the two measurements occur an hour apart.

Continuing with $\beta = 1$, let us use the TAVEX data to reconstruct a nominal image of $I_z^\star$ and $Q_z^\star$ versus depth over the $\sim$ 1 km range, using eight discrete source ranges corresponding to bulbs deployments A1-A8, see Fig. 7.5a. Figure 7.12e and 7.12f show the reconstruction of $I_z^\star$ and $Q_z^\star$ at 210 Hz, using Eq. 7.18, as a function of range and depth. Note that

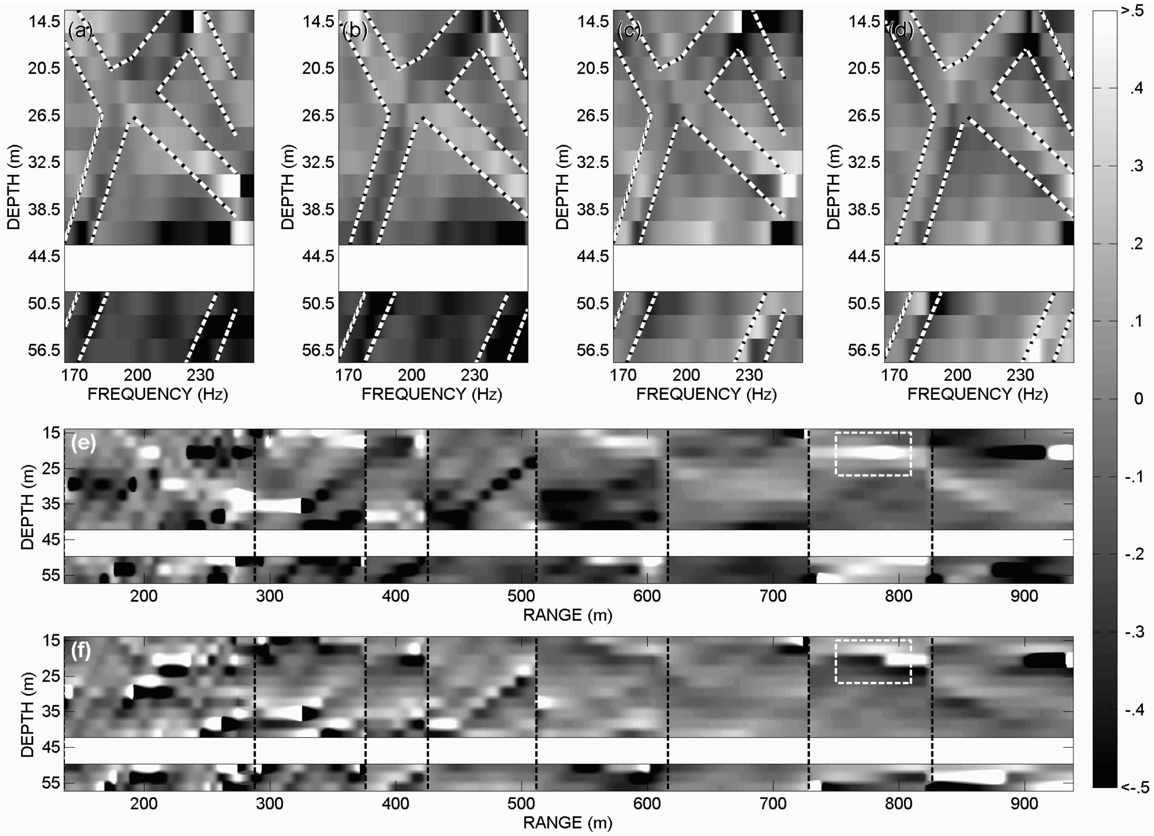

Figure 7.12: (a) $I_z^\star$ versus depth for bulb A6 (range 675 m); (b) corresponding $I_z^\star$ for bulb A10 (range 698 m). (c) $Q_z^\star$ versus depth for bulb A6; (d) corresponding $Q_z^\star$ for bulb A10. Regions where $I_z^\star$ is elevated above the neighboring frequencies and $Q_z^\star$ is convergent are highlighted by dotted lines. Whited out regions correspond to a 6 m gap in data due to an inoperable hydrophone. (e) Eight source-ranges (corresponding to bulb deployment A1-A8) and the waveguide invariant ($\beta = 1$) are used to reconstruct $I_z^\star$ at 210 Hz as a function of range at the 13 depths; (f) corresponding $Q_z^\star$.

closer ranges require a larger frequency span, following Eq. 7.18, to fill in the gap between sources, and a variable frequency range ($d\omega < 2\pi \times 100$ Hz) is employed to accommodate the different range gaps dr associated with A1-A8. Vertical lines in the reconstruction in Figs. 7.12e and 7.12f identify a portion of data used. For example, the data used for the farthest range, between 825 m and 950 m, is based on data from A8, collected at a range of 900 m.

In this experiment, there is a degree of ambiguity in the source depth, source range and array shape These points must necessarily add to the fact that the ranges corresponding to bulb signals A1-A8 were measured at different times, and thus the water column SSP certainly differed slightly for each range. Furthermore, the bottom model used in the PE simulation can be viewed as only approximate. With these limitations in mind, the TAVEX data reconstruction does share some features with the PE simulation, particularly at short ranges. In general, both the data and PE simulation show more bands and seams at ranges less than 500 m than at ranges greater than 500 m. This is because the 500 m range represents a transition of the field into the trapped mode regime. For example, a normal mode solution, based on the same waveguide parameters at frequency 210 Hz (using the program KRAKEN [49]), is described by six trapped modes, and converges to PE simulated field for ranges greater than ~500 m.

Finally, regarding the bottom model, small changes in sediment sound speed (~10 m/s) change the relative positions of dislocations significantly, an observation that could be exploited for geo-acoustic inversion. On the other hand, small changes in sediment density (~ 10 kg/m^3) have little effect on $I_z^\star$ and $Q_z^\star$. Additional sediment layering in the bottom model can also change the position, as well as increase the number, of dislocations in the waveguide.

Chapter 8

CONCLUSION

8.1 Summary of Contributions

This thesis develops the methodologies to apply a vector description of the acoustic field to the analysis and interpretation of experimental field measurements, and with the long-terms goal of discovering new applications of vector acoustics in underwater acoustics. Environments with an increasing degree of complexity in the vector field are studied, first examining vector properites in the most basic interference fields, and then examining properites of the complicated acoustic propagation in ocean waveguides. The key experimental accomplishments of this work are based on measurements of the pressure gradient between closely spaced hydrophones, which are used to estimate particle velocity and a component of intensity. However, this thesis also involves the construction of an accelerometer-based sensor, which is compared with a commercially-made vector sensor. When these vector sensors are paired with a simultaneous, co-located pressure measurement, they form a combined sensor which allows for estimation of the vector acoustic intensity.

The key science and engineering contributions of this thesis are as follows:

- Properties of the acoustic intensity vector in waveguides were studied using field data I collected off the coast of South Korea in 2008. The results from this study, which were published in the Journal of the Acoustical Society of America in March of 2012 [7], establish the framework to compute the complex acoustic intensity from real pressure measurements, using the notation developed by Heyser [3]. Given only the vertical component of intensity, I was motivated to apply non-dimensional field indicators, such as the pressure intensity index developed by Jacobson [35], to examine features of the complex intensity field. This is, to my knowledge, the first time these intensity field indicators have been applied to ocean acoustic measurements, and their use provided evidence of unique intensity features in waveguide propagation, namely the formation of dislocations where destructive interference completely cancels the acoustic field.

In the development of this paper, I used acoustic simulations, both analytic and numerical, to examine the complete acoustic field in an underwater waveguide. The simulations revealed an interesting spatial dependence of the field indicators, related to bands of divergent reactive intensity that pass through regions containing an active intensity vortex. The paper goes on to relate the spatial dependence of these structures to their frequency dependence, through the concept of the waveguide invariant. This paper constitutes a significant portion of my Ph.D. work on the complex vector intensity.

- The effect of seabed layering on properties of the vertical intensity was studied using field data, collected by my advisor, Peter Dahl, during an experiment off the coast of New Jersey in 2006. The results from this study (Journal of the Acoustical Society of America in July of 2013 *in press* [8]), are presented in terms of a non-dimensional parameter, the degree of circularity, which relates to trajectory of the particle velocity vector. I first became aware of the property of circular (elliptical) particle motion, and the ability to measure it, once I placed the vector sensor system that I had been developing in a water-filled tank with a constant frequency source. Following the work of D'Spain [17], I was able describe these observations by the degree of circularity from either measurements of particle velocity and complex intensity. I extended these definitions, using the notation developed by Heyser, to formulate a time dependent form of the degree of circularity. With this notation, I was able to express the gradient-based field measurements of the vertical intensity in terms of an approximate degree of circularity.

  The validity of this approximation was tested in a controlled laboratory experiment using an accelerometer-based vector sensor. This experimental comparison is the first time the degree of circularity has been measured in a controlled laboratory experiment and validated by theory. These results are included in the July 2013 paper, along with a demonstration an application of this technique to geo-acoustic inversion. In this demonstration, field measurements of the approximate degree of circularity were used to estimate geo-acoustic parameters of the seabed, and were compared to other inversion studies originating from the same area. The parameter dependent sensitivity of this inversion method was characterized by the Cramer Rao Lower Bound.

8.2 Future Research

This thesis provides the framework to describe vector properties of the acoustic field and to interpret vector sensor measurements. To paraphrase my advisor, Peter Dahl, now that we have established the basic properties of the vector field, applications will follow.

8.2.1 Analysis of the recent experimental dataset

The ocean vector sensor measurements discussed in Chapter 5, which demonstrated the utility of vector sensors in source-bearing localization, are only a small glimpse of a much larger dataset collected during the Targets and Reverberation Experiment (TREX). The complete dataset consists of recordings, made by a combined sensor and two line arrays, of pulses generated by sources at multiple locations, depths and ranges. In addition to the acoustic data, wave-buoy data was collected to characterize the directional spectrum of the rough sea surface.

The TREX dataset will be used to examine the feasibility of determining the depth of a source, which is currently a very difficult problem in shallow water, from vector properties of the field. The complete (3-D) intensity vector measured by the combined sensor will also allow for analysis of the azimuthal properties of the sound field, and will be used study vector properties, and their relationship to spatial coherence estimates made by the line arrays. Furthermore, simultaneously measured sea surface wave spectra, using a wave-buoy, will be used to study the effect of the rough sea surface on vector properties of the field. These studies will be conducted in a post-doctoral setting that I have arranged with my advisor.

8.2.2 Vector properties of aircraft noise transmitted into water

Measurements of the pressure field on both sides of the air-water interface of a propeller aircraft transiting overhead, which I made with my advisor in 2007, show that the underwater sound field consists of a transmitted and an evanescent component. The characteristic Doppler shift of the tonal propeller noise provides a separation (in time and frequency) of these two components in the measured pressure data. A model of the in-air and underwater pressure field that is based on the complex intensity, shown in Fig. 8.1, predicts the measured pressure level due to the active intensity (transmitted) and reactive intensity (evanescent). An in-depth analysis of these measurements is nearly complete, and is to be submitted to the Journal of the Acoustical Society of America.

Future measurements of this transmission phenomenon, using a vector sensor, will validate this intensity-based model of air-to-water transmission, and may provide vector information relating to the interference between the transmitted and evanescent components of the field. Vector properties, such as the degree of circularity, may also allow for the separation of these two components without a Doppler shift.

8.2.3 Explosion research

During my PhD work, I participated in an experiment to measure the sound of underwater explosions off the coast of Virgina Beach, Virgina. The research was motivated by the US Navy as part of a required environmental impact assessment of their Explosive Ordnance Disposal (EOD) training exercises. The measurements provided calibrated estimates of the pressure field (potential energy) caused by explosions, made by an EOD team. I have an interest in measuring the kinetic energy of these explosions with vector sensor, and may have the opportunity to do so in a future collaboration with another EOD team.

8.2.4 Fish Behavior Studies

Fish have an internal mechanism that can sense acoustic particle motion, and as shown by a team of researchers at the University of Washington [24], fish respond to the orientation of the particle velocity field. It was shown that the fish follow the orientation of straight line

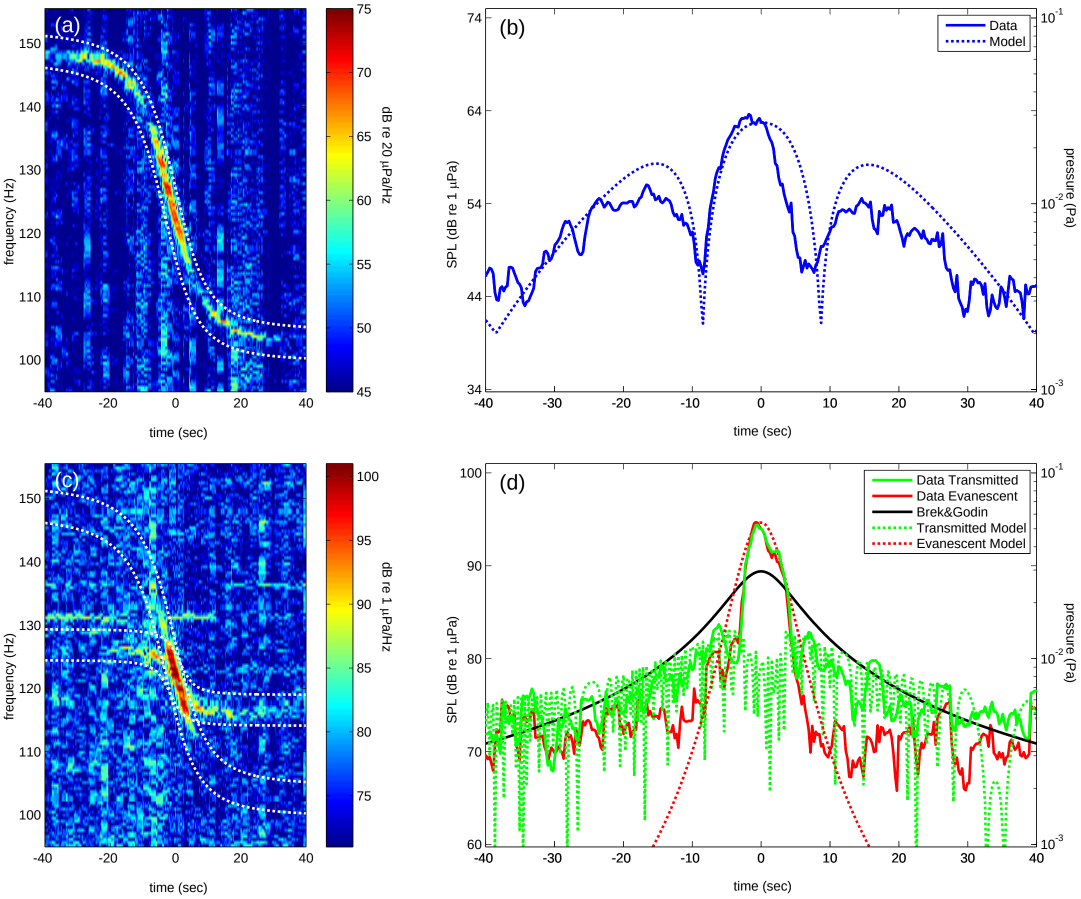

Figure 8.1: (a) Spectrogram of the in-air pressure field measured by the microphone during the overflight of a propeller aircraft. (b) The sound pressure level, SPL, of the data (solid blue) and model (dotted blue) which are constructed from the integrated spectrum over the frequencies between the two white dotted lines, which correspond to the Doppler shifted tone at 121 Hz. (c) Spectrogram of the in-water pressure field measured by a hydrophone. (d) The SPL of the underwater field is computed for the two Doppler shifted arrivals, the transmitted path for the data (solid green) and the model (dotted green) and the evanescent path for the data (solid red) and model (dotted red). The data for the two arrivals are integrated spectrum over the frequencies between the two white dotted lines, which correspond to their respective Doppler shifted tone at 121 Hz.

particle motion paths, which was experimentally measured by an acceleration based vector sensor (similar to that described in this thesis). It was noted that the behavior of the fish was dependent on their placement in the tank, and their behavior appeared to be affected by reflections from the walls the experimental tank. It is possible that fish are not only sensitive to the magnitude and direction of particle motion, but can sense vector properties of the acoustic field as well.

Characterization of the acoustic field based on vector properties may help in the design of fisheries research vessels, so fish do not avoid them during surveys, and in the environmental impact assessment of noise-generating sources. A NSF-funded collaboration between Peter Dahl and the Northwest National Marine Renewable Energy Center will measure the acoustic particle velocity near tidal turbines. It will be interesting to see the turbines effect on the vector properties of the acoustic field and to assess marine life's reactions to them.

BIBLIOGRAPHY

[1] Shchurov, V.A., *Vector acoustics of the ocean.* Vladivostok: Dalnauka, 2006 p. 16.

[2] Allan D. Pierce, *Acoustics: An Introduction to its Principles and Applications* Woodbury, NY Acoustical Society of America, 1991 p. 130-135.

[3] Richard C. Heyser, "Instantaneous intensity," Proceedings of the 81st Convention of the Audio Engineering Society, Preprint 2399, (1986).

[4] Frank J. Fahy, *Sound Intensity: Second Edition.* London: Chapman and Hall, 1995 p. 105.

[5] Jacobsen, F., "A note on instantaneous and time-averaged active and reactive intensity." J. Sound Vib. 147, 489-496 (1991).

[6] Richard C. Heyser, "Fundamental Principles and some applications of Time Delay Spectrometry" in *Time Delay Spectrometry* (Audio Engineering Society, New York, 1988), pp. 205-262.

[7] D. R. Dall'Osto, P. H. Dahl, and J. W. Choi, "Properties of the acoustic intensity vector field in a shallow water waveguide," J. Acoust. Soc. Am. **131**, 2023-2035 (2012).

[8] D. R. DallOsto, and P. H. Dahl," Elliptical acoustic particle motion in underwater waveguides," J. Acoust. Soc. Am., in press, May 2013.

[9] David T. Blackstock, "Fundamental of physical acoustics," New York: John Wiley and Sons, Inc., 2000 p 27-28.

[10] James A. McConnell, "Analysis of a compliantly suspended acoustic velocity sensor," J. Acoust. Soc. Am. **113**, 1395-1405 (2002).

[11] Peter H. Dahl, "High-Frequency Underwater Sound," Wiley Encyclopedia of Electrical and Electronics Engineering. p. 1-19 2007.

[12] R.V. Waterhouse and D. Feit, "Equal-energy streamlines," J. Acoust. Soc. Am. **80**, 681-684 (1986).

[13] David M. F. Chapman, "Using streamlines to visualize acoustic energy flow across boundaries," J. Acoust. Soc. Am. **124**, 48-56 (2008).

[14] Peter H. Dahl, James H. Miller, Douglas H. Cato, and Rex K. Andrew, ”Underwater Ambient Noise,” Acoustics Today 3, 23 (2007).

[15] R.V. Waterhouse, T.W. Yates, D. Feit, and Y.N. Liu, ”Energy streamlines of a sound source,” J. Acoust. Soc. Am. **78**, 758-762 (1985).

[16] J.C. Pascal, ”Structure and patterns of acoustic intensity fields,” Proceedings of the 2nd International Congress on Acoustic Intensity, CETIM 97-103 (1985).

[17] G.L. D'Spain, ”Polarization of Acoustic Particle Motion in the Ocean and its Relation to Vector Acoustic Intensity,” 2nd International Workshop on Acoust. Eng. and Tech., Harbin, China (1999).

[18] V.A. Shchurov, V.P. Kuleshov, and A.V. Cherkasov, ”Vortex Properties of the Acoustic Intensity Vector in a Shallow Sea,” Acoustical Physics, 2011, Vol. 57, No. 6, 851-856 (2011).

[19] J.A. Mann III, J. Tichy, and A.J. Romano, ”Instantaneous and time averaged energy transfer in acoustic fields.” J. Acoust. Soc. Am. 82, 1729 (1987).

[20] George Frisk, *Ocean and Seabed Acoustics: A Theory of Wave Propagation*, Englewood Cliffs, New Jersey, Prentice-Hall, Inc., 1994 p. 148, 156, 212

[21] Chun P. Lee and Taylor G. Wang, ”Near-boundary streaming around a small sphere due to two orthogonal standing waves.” J. Acoust. Soc. Am. 85, 10811087 (1989).

[22] Triantafillos Koukoulas, Ben Piper, and Pete Theobald, ”Gated photon correlation spectroscopy for acoustical particle velocity measurements in free-field conditions,” J. Acoust. Soc. Am. **133**, EL156 (2013).

[23] Hans-Elias de Bree, Emiel Tijs, Tuncay Akal, ”The Hydroflown: MEMS-based underwater acoustic particle velocity sensor,” proceedings from ECUA, Istanbul (2010).

[24] David G. Zeddies, Richard R. Fay, Michael D. Gray, Peter W. Alderks, Andrew Acob and Joseph A. Sisneros, ”Local acoustic particle motion guides sound-source localization behavior in the plainfin midshipman fish, Porichthys notatus,” The Journal of Experimental Biology 215, 152-160 (2012).

[25] William M. Carey, ”Lloyd's Mirror - Image Interference Effects,” Acoustics Today, pp. 14-20 April (2009).

[26] O. A. Godin, ”Low-frequency sound transmission through a gasliquid interface,” J. Acoust. Soc. Am. **123**,1866-1879 (2008).

[27] M.J. Wilmut, N.R. Chapman, G.J. Heard and G.R. Ebbeson, "Inversion of Lloyd Mirror Field for Determining a Sources Track," IEEE J. of Oceanic Eng. Vol. 32, No. 4 (2007).

[28] Dahl, P.H., D.R. Dall'Osto and W. J. Plant, "Vertical coherence and forward scattering from the sea surface and the relation to the directional wave spectrum ," submitted to, J. Acoust. Soc. Am., March 2013.

[29] J.W. Choi, P.H. Dahl and John Goff, "Observations of the R reflector and sediment interface reflection at the Shallow Water '06 Central Site," J. Acoust. Soc. Am. **124**, EL128-EL134 (2008).

[30] M. D. Collins, "A split-step Pade solution for the parabolic equations method," J. Acoust. Soc. Am. **93**, 1736-1742 (1993).

[31] J. A. Goff and J. A. Austin, Jr., "Seismic and bathymetric evidence for four different episodes of iceberg scouring on the New Jersey outer shelf: Possible correlation to Heinrich events," Mar. Geology, vol. 266, pp. 244-254, (2009).

[32] H. Schmidt, A. B. Baggeroer, "Physics-imposed resolution and robustness issues in seismo-acoustic parameter inversion," Full Field Inversion Methods in Ocean and Seismo-Acoustics, 85-90 (1995).

[33] Finn B. Jensen, Michael B. Porter, William A. Kuperman, and Henrik Schmidt, *Computational Ocean Acoustics* Springer New York, 2011.

[34] Jacobsen, F., "Active and reactive, coherent and incoherent sound fields," Journal of Sound and Vibration 130(3), 493-507 (1989).

[35] Jacobsen, F., "Sound Field Indicators: Useful Tools," Noise Control Engineering Journal 35(1), 41-46 (1990).

[36] D. Rouseff, "Effects of shallow water internal waves on ocean acoustic striation patterns," Waves Random Media 11, 377-393 (2001).

[37] Jorge E. Quijano, Lisa M. Zurk and Daniel Rouseff, "Demonstration of the invariance principle for active sonar," J. Acoust. Soc. Am. 123, 1329-1337 (2008).

[38] K.L. Cockrell and H. Schmidt, "Passive ranging using the waveguide invariant," J. Acoust. Soc. Am 127, 2780-2789 (2010).

[39] Turgut, A.,Orr M., and Rouseff, D., "Broadband source localization using horizontal-beam acoustic intensity striations." J. Acoust. Soc. Am 127, 73-83 (2010).

[40] Ren, Qun-yan, J.-P. Hermand and Sheng-chun Piao, "The interference phenomena of broad-band vector field and striation processing," Proceedings, 4th International Conference and Exhibition on "Underwater Acoustic Measurements: Technologies & Results" pg. 905-912 (2011).

[41] G.L. D'Spain, D.P. Williams, G. Rovner, W.A. Kuperman, and the SWARM 95 Team, "Energy Flow in Interference Fields," Proceedings of Ocean Acoustic Interference Phenomena and Signal Processing, pg. 171-203 (2002).

[42] L. M. Brekhovskikh and Y. P. Lysanov, *Fundamentals of Ocean Acoustics.* 3rd ed. New York: Springer, 2002 p. 142.

[43] V. A. Eliseevnin and Yu. I. Tuzhilkin, "Acoustic power flux in a waveguide," Acoust. Phys. 47, 688-694 (2001).

[44] Heard, G.J., McDonald, M., Chapman, N.R., Jaschke, L., "Underwater light bulb implosions: a useful acoustic source," OCEANS '97. MTS/IEEE Conference Proceedings, vol.2, no., pp.755-762 vol.2, 6-9 Oct (1997).

[45] Jacobsen, F., "A note on finite difference estimation of acoustic particle velocity," Journal of Sound and Vibration 256(5), 849-859 (2002).

[46] Lin Wan, Ji-Xun Zhou, and Peter H. Rogers, "Low-frequency sound speed an attenuation in sandy seabottom from long-range broadband acoustic measurements," J. Acoust. Soc. Am. 128, 578-589 (2010).

[47] J. S. Youn, G. W. Go, "Sedimentological characteristics of the surface sediments in the southern sea off Cheju Island, Korea", The journal of the Oceanological Society of Korea, Vol. 22, No. 3, (1987).

[48] Rouseff, D., and Spindel, R. C. Modeling the waveguide invariant as a distribution, Proceedings of Ocean Acoustic Interference Phenomena and Signal Processing, pg. 137-150 (2002).

[49] M. B. Porter, "The KRAKEN Normal Mode Program," (last viewed June 11, 2013), http://oalib.hlsresearch.com/Modes/AcousticsToolbox/manual_html/kraken.html (1997).